A Study of the Nucleation and Formation of Multi-functional Nanostructures using GaN-Based Materials for Device Applications

A Dissertation
Presented to
The Academic Faculty

By

Hun Kang

In Partial Fulfillment
Of the Requirements for the Degree
Doctor of Philosophy in the School of Electrical & Computer Engineering

Georgia Institute of Technology

[December, 2006]

A Study of the Nucleation and Formation of Multi-functional Nanostructures using GaN-Based Materials for Device Applications

Approved by:

Dr. Ian Ferguson, Advisor

School of Electrical and Computer Engineering

Georgia Institute of Technology

Dr. Stephen Ralph

School of Electrical and Computer Engineering

Georgia Institute of Technology

Dr. Rina Tannenbaum

School of Materials Science and Engineering

Date Approved:

Georgia Institute of Technology

Dr. Oliver Brand

School of Electrical and Computer Engineering

Georgia Institute of Technology

Dr. Jennifer Michaels

School of Electrical and Computer Engineering

Georgia Institute of Technology

ACKNOWLEDGEMENTS

First, I would like to express my appreciation for my advisor, Dr. Ian T. Ferguson, for his cordial, constant advice and intimate guidance. He continuously encourages my potential to think and work creatively. During my graduate years, he has sincerely advised me to achieve my thesis work not only as an academic advisor but also as a mentor. The lessons he gave me will be treasured in my mind for the rest of my life. I also acknowledge Dr. Brand, Michaels, Ralph, and Tannenbaum for serving on my committee. Their suggestions, discussion and criticism made my works more complete.

I would like to thank my friends at Georgia Tech. I express special thanks to solid state light group members, Dr. Park, Dr. Wang, Dr Vincent, Dr. Fang, David, Matt, Nola, Omkar, Olivie, Shalini, Tahir, Will, Yong, my precious friends at Georgia Tech, for sincerely sharing my concern and passion.

I would like to express my heartfelt appreciation for my parents. Most of all, I love to thank my precious wife, Younghee Kim, for her love and unconditional sacrifice. Without her love and support, I could not even imagine achieving this thesis work.

TABLE OF CONTENTS

CHAPTER 3 : THREADING DISLOCATIONS IN III-NITRIDES…..34

LIST OF TABLES

LIST OF FIGURES

SUMMARY

The objective of this research is to design multi-functional GaN nanostructures for optoelectronic and spintronic applications and to study the growth conditions for epitaxial material using metal-organic chemical vapor deposition (MOCVD).

III-nitrides have been known as prospective materials for semiconductor device applications for a wide range of wavelengths. However, it is more difficult to produce high quality GaN-based semiconductor compounds, compared to GaAs compounds due to the absence of coherently matched substrates. The most common substrate used for GaN growth is sapphire which has a lattice mismatch of 16%. The high dislocation densities resulting from this lattice mismatch may be detrimental to light output efficiency with optoelectronic semiconductors

Nanostructures are too small to have dislocations as well as they have spatially quantized electronic energy states. This results in more stable thermal perturbation and high quantum efficiency of light emitting devices. But it is also difficult to grow and control nanostructures. In this thesis, multi-functional self-organized GaN nanostructure was investigated

We have achieved self-organized GaN nanostructures on AlN system using MOCVD. The MOCVD provided a remarkable control ability to form nanostructures. The growth techniques which are obtained from typical bulk GaN growths encouraged the self-organized nanostructure growth. We have changed growth conditions: temperature, V/III ratio, Ga flux, and introduction of anti-surfactants. Especially, the growth temperature and V/III ratio affecting Ga migration and evaporation were

optimized at around 800 ºC and 300 respectively. Growth pressure was also investigated with a wide range. A good result was obtained with lower pressures from 100 to 200 Torr. We kept the pressure 100 Torr in this work. Under these optimized growth conditions, the nanostructure height and diameter were less than 7 nm and 50nm, respectively. The nanostructure density was also enhanced up to the order of 10 cm^{-2}.

We have also achieved self-organized GaN nanostructures on AlGaN system for nearly lattice- matched system ($\leq$ 0.5%) using a new growth technique: metal droplet method. In the method, a liquid droplet condensing from vapor phase transforms crystal solid under chemical vapor deposition conditions at a high temperature. The nanostructure size and density were improved by changing growth parameters. We have optimized the TMGa flux and flow time and island size was apparently minimized and density was maximized at this optimized TMGa flow rate.

The emission wavelength for GaN nanostructure is dependent both on quantum confinement and piezoelectric effect. It was observed that larger dots obtained at a higher V/III ratio resulted in a red shift. The shift to higher energies with a decrease in nanostructure size is attributed to the decrease in piezoelectric effect rather than quantum confinement. The intensity of the PL is dependent on the density of the nanostructures. A higher PL intensity is obtained with a higher density of nanostructures. In addition, a numerical approach was performed to calculate excitonic and optical properties of GaN nanostructure system and we had a good agreement with experimental data.

The magnetic and structural properties of ferromagnetic self-assembled GaN nanostructures have been studied for spintronic applications. Transition metal (TM ; Mn or Fe) was incorporated into GaN nanostructures at a relatively low temperature, and the

ferromagnetic behavior of GaN:TM nanostructures at room temperature was observed. In addition, atomic force microscopy measurements revealed that TMs affected the surface morphology of these nanostructures.   A small amount of TM incorporation affected both island size reduction and nucleation, enhancing quantum confinement as well as ferromagnetism in the GaN:TM nanostructures. The increased island density improved the magnetic characteristic after minimization of island size.

CHAPTER 1

INTRODUCTION

The objective of this research is to accomplish multifunctional GaN-based nanostructures using metal-organic chemical vapor deposition (MOCVD) which are attractive for both optoelectronic devices with higher performance and spintronic devices with quantum-quantized and diluted magnetic semiconductors. In this study, nano-scale GaN quantum dots were grown with various growth conditions, incorporated transition metals (e.g. Mn and Fe) into, and characterized by structural, optical, and magnetic measurements.

GaN and its alloys with InN and AlN have been used for optoelectronic devices in the spectral ranges of blue and ultraviolet wavelengths because they have wide direct energy band gaps [1,2]. High dislocation densities, however present a barrier for the development of GaN-based optoelectronic devices. In dislocation sites, non-radiative combination occurs, where the energy is radiated by phonons resulting in heating instead of photons emission, thereby lowering light output efficiency. In order to improve device efficiency, many people have been studying in the other fields (i.e. growth techniques, fabrications, new structure development). In these growth techniques, buffer layer [3] and/or interlayer as a filter [4] to reduce dislocations are introduced and LEO (lateral epitaxial overgrowth) technique [5] is also employed. In the territory of fabrication, there are new techniques of p-GaN contact [6] and photonic crystal [7]. Moreover, new

structures have also been researched. Low dimensional (0, 1, or 2 D) nanostructures in an active layer of optoelectronic devices have no dislocation and even high quantum confinement, which can overcome this low efficiency issue [8,9]. For optoelectronic semiconductor devices, the size of the 0-D quantum dots must be on the order of the exciton Bohr radius for quantum confinement of carriers with an energy bandgap smaller than the surrounding semiconductor matrix. No structural defects (such as dislocations) which lead to non-radiative recombination of the bound states of electrons and holes are allowed to exist in the quantum dot layer [10, 11].

MOCVD is the most common powerful tool to grow thin films for compound semiconductor materials and devices. Since S. Nakamura researched GaN-based laser diode which constructed on herteroepitaxially grown GaN film strucuture [20], III-nitride growth using MOCVD is more attractive for optoelectronic applications. In the chapter 2, general MOCVD growth has been studied. I had firstly concentrated on the improvement of the film quality of AlN and AlGaN for QD templates by studying growth conditions, Ga/N flux ratio. The optimization of these conditions is the key to improving the quality and surface roughness of these films grown by MOCVD on sapphire. Once high-quality films were produced, GaN QDs were fabricated.

In this work, I have studied estimation of dislocations in nitride materials using XRD. Chapter 3 explained how to determine dislocation densities from XRD measurements. Since XRD is non-destructive and rapid characterization technique it is the most common technique used to optimize crystalline quality growth parameters. III-nitrides are different to other compound semiconductor materials because it is formed with large areas of crystalline material that are misaligned to each other, a columnar

structure (i.e. mosaic structure) [12]. Thus an estimate of size of those domains, the average misorientation between them and dislocation density is important in optimizing material growth. High-resolution XRD reciprocal space mapping (RSM) is normally utilized for detailed characterization of such crystalline structures. However, a much quicker and simpler method to obtain similar information utilizes the Williamson-Hall (WH) plot. This study gave me a motivation to develop another structure without dislocations which is the nanostructure.

Stranski-Krastanow(SK)-like growth mode is not supported for the lattice mismatch between GaN and AlN (~2.5%) according to the theoretical model developed by Daruka et al [13]. A 3D growth by a ripening process creating islands with infinite size is predicted for GaN/AlN heterostructures based on kinetics and thermodynamics [14]. However, under extreme growth conditions GaN nanostructures have been shown to have SK-like mode formations on SiC substrates using Molecular Beam Epitaxy (MBE) and Metal Organic Chemical Vapor Deposition (MOCVD) [15, 16]. The chapter 4 presented nucleation studies of GaN nanostructures on AlN grown on sapphire substrates by MOCVD. Further, a thermal activation step is introduced to the GaN/AlN hetero-system to support the formation of 3D islands revealing a SK-like growth mode.

GaN nanostructure / $Al_{0.2}Ga_{0.8}N$ system has a smaller lattice mismatch (< 0.5 %), which is a nearly lattice-matched system for the nanostructure growth. In the lattice-matched system, it is very difficult to grow nanostructures using SK-like growth mode. Thus, it is required for a unique growth technique to achieve GaN nanostructures on AlGaN system. In the chapter 5, a metal droplet technique was described for

nanostructure growth. In addition, effects of growth parameters on nanostructure formation were investigated and their characterizations were explained.

In the lower dimension nanostructures, excitronic and optical properties are dependent on the nanostructure size, because the size determines both quantum confinement and piezoelectronic effect. In chapter 6, numerical analysis was performed on GaN / AlN system to reveal the relationship between these properties and nanostructure size. This numerical calculation was executed with some assumptions regarding for cylindrical coordinate, boundary conditions and so on. It was found that the confinement effect was stronger than piezoelectronic effect with less than 4.1nm of nanostructure height and confinement were offset at about 4.1 nm of nanostructure height. Otherwise, piezoelectronic effect was dominant to affect excitronic and optical properties. However, GaN / AlGaN system has so small lattice mismatch that piezoelectronic effect could be ignored. Moreover, there was a good agreement with the experimental data.

III-V diluted magnetic semiconductors (DMS's) have been attractive due to the possibility to fabricate spintronic devices using both the spin and the charge freedom of the carriers from their systems. However, only DMS with Curie temperatures (T_c) > 300 K allows spintronic devices to work at room temperature (RT) [17]. In this respect, GaN has shown promise for a host material of RT ferromagnetic semiconductors, but it seems difficult to realize RT ferromagnetism on bulk or epitaxial systems [18,19]. Chapter # presents the successful incorporation of TMs (transition metals) in GaN nanostructures and ferromagnetisms in these structures.

1.1 References

[1] K. Hiramatsu, S. Itoh, H. Amano, I. Akasaki, N.Kuwano, T. Shiraishi and K. Oki. J. Cryst. Growth **115**, 628 (1991).

[2] B. Gil (editor), "Group III Nitirde Semiconductor Compounds", Oxford University Press, ISBN, 0-19-850159-5, (1998).

[3] H. Amano, N. Sakai, I. Akasaki, and Y. Todada, Appl. Phys, Lett. **48**, 353 (1986)

[4] H. Wang, J. Zhang, C. Chen, Q. Fared, J Yang, and A. Khan, Appl. Phys, Lett. **81**, 604 (2002)

[5] S. Nakamura, M. Senoh, S. Nagahama, N. Iwasa, T. Yamada, T. Matsushita, Y. Sugimoto, and H. Kiyodu, Jpn. J. Appl. Phys., Part II **36**, L1059 (1997)

[6] J. Song, J. Kwak, Y. Park, T. Sung, Appl. Phys, Lett. **86**, 062104 (2005)

[7] D. Coquillat, J. Torres, R. Legros, J. Lascaray, D. Peyrade, Y. Chen, et. al. *Proceedings of SPIE* **5450**, 540 (2004)

[8] E. Bourret-Courchesne, S. Kellermann, K. Yu, M. Benamara, Z. Liliental-Weber, J. Washburn, S. Irvine, and A. Stafford, Appl. Phys. Lett. **77**, 3562 (2000).

[9] C. Chen, J. Zhang, M. Gaevski, H. Wang, W. Sun, R. Fareed, J. Yang, and M. Khana, Appl. Phys. Lett. **81**, 4961 (2002).

[10] L. Ji, Y. Su, S. Chang, C. Chang, L. Wu, W. Lai, X. Du, and H. Chen, J. Cryst. Growth **263**, 114 (2004).

[11] H. Shecnk, P. Vennegues, O. Tottereau, T. Riemann, and J. Chreisten, J. Cryst. Growth **258**, 232 (2003).

[12] T. Cheng, L. Jenkins, S. Hooper, and C. Foxon, Appl. Phy. Lett. **66**, 1509 (1995)

[13] I. Daruka, et al., Phys. Rev. Lett. 79 (1997) 3708.

[14] F. Widmann et al., J. Appl. Phys. 83 (1998) 7618

[15] B.Daudin, et al., Physica E21 (2004) 540

[16] M. Miyamura, et al., Appl. Phys. Lett. 80 (2002) 3937.

[17] K. Sato and H Katayama-Yoshida Physica B **308** 304 (2001)

[18] V. Dmtriew. K. Irvine, A. Zubrilov, D. Tsvetkov, V. Nikolacv, M. Jakobson, D. Nelson, and A. Sitnikova, Gallium Nitride and related Materilas. MRS, (1996)

[19] A. Corrion, F. Wu, T. Mates, C. Gallinat, C. Poblenz, J. Speck, J. Crys. Growth, **289** (2006) 587

[20] S. Nakamura, M. Senoh, S. Nagahama, N. Iwasa, T. Yamada, T. Matsushita, H. Kiyoku and Y. Sugimoto, Appl. Phys. Lett., 69 (1996) 1477.

CHAPTER 2

OVERVIEW : MECHANISMS AND GROWTH TECHNIQUES OF MOCVD III-NITRIDE GROWTH

2.1. Introduction

Metal-Organic Chemical Vapor Deposition (MOCVD) is the most versatile and powerful technique for thin film growth. Its potentials have been proven by producing high quality epitaxial layers with excellent surface morphology and a precise control over layer thickness and uniformity. MOCVD has been applied to the epitaxial crystal growth technology for an impressive array of commercial devices: lasers, light emitting diodes, photocathodes, heterostructure bipolar transistors, photodetectors, and solar cells [1,2].

2.2. Growth mechanisms of MOCVD

Basic chemical reaction types in CVD technology include pyrolysis (thermal decomposition), oxidation, reduction, hydrolysis, nitride and carbide formation, synthesis reactions, disproportionation, and chemical transport. A sequence of several reaction types may be involved in more complex situations to create particular products. Major parameters are temperature, pressure, input concentrations, gas flow rates, and reactor geometry which all together determine the deposition rate and the properties of the film deposit.

However, the fundamental growing steps in MOCVD are shown in Figure 2.1 [3-12]:
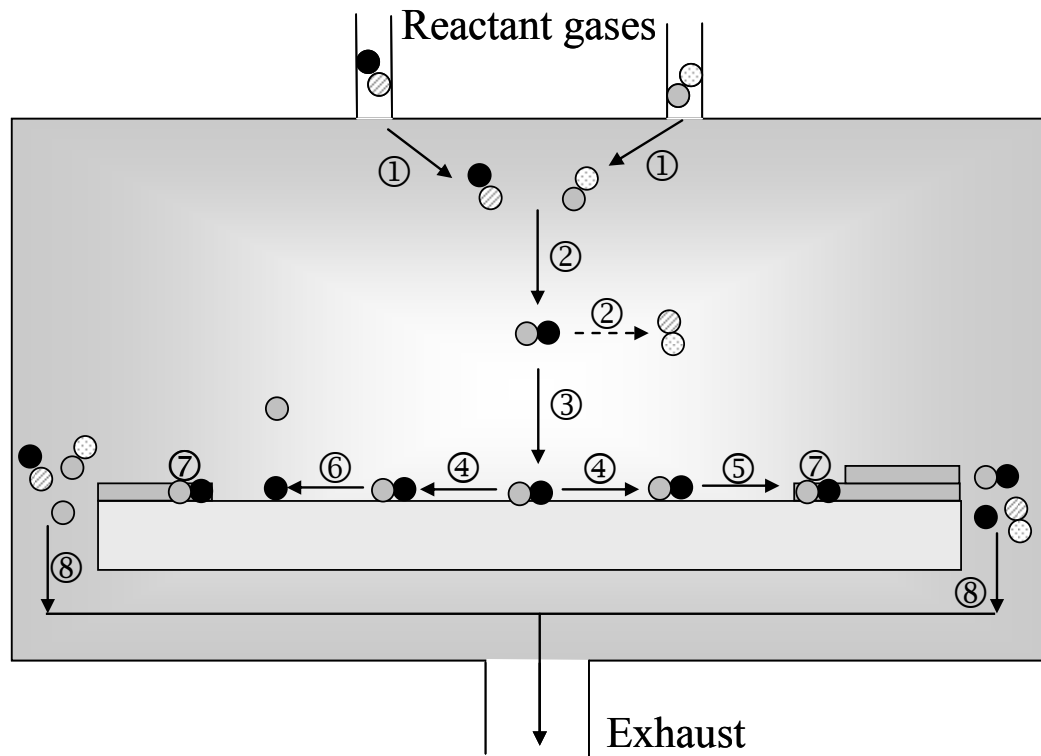
Figure 2.1 Schematic of MOCVD growth mechanisms.

① Gas phase diffusion - convective and diffusive transport of reactant gases into the reaction chamber.

② Gas phase reaction - typical chemical gas-phase reactions which generate the constituent species for deposition and by-products.

③ Transport and absorption on surface - transport of these reactants to the surface and (chemical or physical) absorption on the surface.

④ Surface diffusion - diffusion of these species on the surface.

⑤ Incorporation at kink - incorporation of these species at kinks.

⑥ Desorption - desorption or evaporation of volatile species from the surface.

⑦ Nucleation and step growth for film formation - the phase change including vapor-phase condensation, solidification, or solid-state phase transformation from gases, melts, or solid matrices leading to film formation.

⑧ Gas exhaustion - transport of the rest by-products during reactions to gas exhaust outlet.

This chapter explains pyrolysis, thermodynamics, mass transport, and kinetics for the above fundamental processes of MOCVD.

2.2.1. Pyrolysis

In MOCVD processes, it is important to consider basic chemical reactions in the reaction chamber. The most common chemical reaction is pyrolysis which is related to thermal decomposition of gaseous species such as hydrides and volatile metal-organic radicals for semiconductor material growth. The general equations for (2.1) binary, (2.2) ternary, and (2.3) quaternary compounds are given by

$$R_nA + DH_n \rightarrow AD + nRH \qquad (2.1)$$

$$xR_nA + (1-x)R_nAB + DH_n \rightarrow A_xB_{1-x}D + nRH \qquad (2.2)$$

$$xR_nA + (1-x)R_nAB + yDH_n + (1-y)EH_n \rightarrow A_xB_{1-x}D_yE_{1-y} + nRH \qquad (2.3)$$
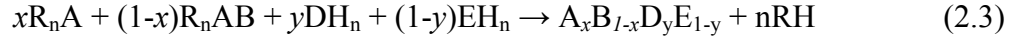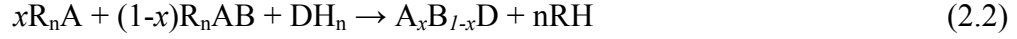
where H is hydrogen and R is an organic radical such as a methyl $[(CH_3)_3]$ or ethyl $[(C_2H_5)_3]$-radical. A, B, and D are the constituent species for the deposited solid, and they come from trimethygallium (TMGa), trimethylaluminium (TMAl), and trimethylindium (TMIn) commonly utilized as MO sources for MOCVD process. These organometallic species are diffused to the reaction chamber with carrier gases, hydrogen or nitrogen or a mixture of these two [13, 14]. For instance, the pyrolysis of GaN is given by $(CH_3)_3Ga + NH_3 \rightarrow GaN + 3CH_4$.

2.2.2 Thermodynamics

Thermodynamics is a main driving force to contribute desired deposition materials formed by the pyrolysis process for epitaxial growth, where precursors are unstable at growth temperatures. The basic consideration of thermodynamics is to define the relationship between the compositions of the various phases in an equilibrium state where Gibbs free energy (G) per mole is a minimum at constant temperature and pressure. In thermodynamics, the Gibbs free energy is the energy portion of a thermodynamic system. The Gibbs free energy is a thermodynamic potential and is therefore a state function of a thermodynamic system [15, 16]. The Gibbs free energy, G, is defined as

$$G = H - TS \qquad (2.4)$$

where S is the entropy of the system and H is the enthalpy, as $H = E + PV$ where E is the

internal energy, P is the pressure, and V is the volume.

In III-nitride systems, the strong triple bond in the N_2 molecule (4.9 eV/atom) lowers the thermodynamic potential (Gibbs free energy, G) of the system including nitride constituents. Since this free energy of these constituents decreases with higher temperature, nitrides lose their thermodynamic stability at high temperatures required for effective synthesis and bulk crystallization.

The reaction of the synthesis of one mole of metal nitride MeN is Me + ½N_2 → MeN. Free energy change, ΔG, for this reaction:

$$\Delta G = G_{MeN} - (G_{Me} + \frac{1}{2}G_{N2})$$

$$= H_{MeN} - (H_{Me} + \frac{1}{2}H_{N2}) - T\,[S_{MeN} - (S_{Me} + \frac{1}{2}S_{N2})\,]$$

$$= \Delta H - T\Delta S \tag{2.5}$$

In equilibrium ΔG = 0. If ΔG < 0, nitride is stable. In addition, these equations give the general basis for the phase diagram [17].

2.2.3 Mass Transport

Thermodynamic calculation only sets the maximum value for growth rate. Growth rate also depends on mass transport which affects the thickness uniformity of deposited film. However, the mass transport is the process of volatile species flowing in the reaction chamber. This mass transport is mainly divided into two terms, diffusion and hydrodynamics. Diffusion is the motion of individual atomic or molecular species, while hydrodynamic flow is the motion of a group of gases as a whole, such as viscous flow and convection [18, 19].

Diffusion is mass transport from a higher chemical potential to a lower chemical potential in gases and condensed phases. When two different gases flow in and are mixed, their movements interact and the entropy of the system rises. However, the diffusion is usually represented by the diffusivity, D, in gases which is influenced by pressure and temperature as given by

$$D = D \times P_0 / P \times (T / T_0)^{1.8} \qquad (2.6)$$

where D_0 is the value of D at $T_0 = 273$ K and $P_0 = 1$ atm.. Therefore, diffusion can be enhanced by decreasing pressure or increasing temperature in the reaction chamber [20,21].

The viscous flow, one of the hydrodynamic flows, should be considered under a pressure of 10 Torr. The typical movement of reactant gases is acquainted with streamline-like flow. But this flow could be disturbed, referred as a turbulent flow when the flow moves against a boundary of deposition area. Thus, control of the turbulent flow is important to achieve a good thickness uniformity of deposited film. The viscous flow is described by the coefficient of viscosity η which varies with temperature, $T^{0.5}$, but is independent of pressure [22, 23].

Furthermore, convection is heat transfer in liquids and gases. This is a term used to characterize the combined effects of conduction and fluid flow. In convection, enthalpy transfer occurs by the movement of hot or cold portions of the fluid as well as heat transfer by conduction [24].

2.2.4 Kinetics

In general, both thermodynamics and kinetics play essential roles in the process of thin film growth by MOCVD. While thermodynamics governs the behavior of the system at equilibrium, kinetics controls the tendency of the system to move towards the equilibrium state under a given growth condition. The kinetics depends on many parameters related with reactant movement to the surface and heterogeneous surface reaction. The reactant movement includes adsorption of reactants, surface diffusion, and desorption of gas products, while the heterogeneous surface reaction between gases and solid on the surface leads to film growth [25, 26].

2.2.5 Growth regimes

The practical process conditions in MOCVD growth are under excess, uninterrupted, and nonstoichiometric group V species, which improves the pyrolysis efficiencies and compensates for the much greater volatility of the group V atoms in the desired solid films. Thus, the growth rate of MOCVD epitaxial layers mainly depends on the group III alkyl constituents. Figure 2.2 shows three discrete growth regimes which are composed of surface kinetics, mass transport, and thermodynamics.

The first regime, at relatively low temperatures, is a region of surface kinetics limited growth. The alkyl pyrolysis efficiency usually is steep, so this growth regime has a narrow temperature range.
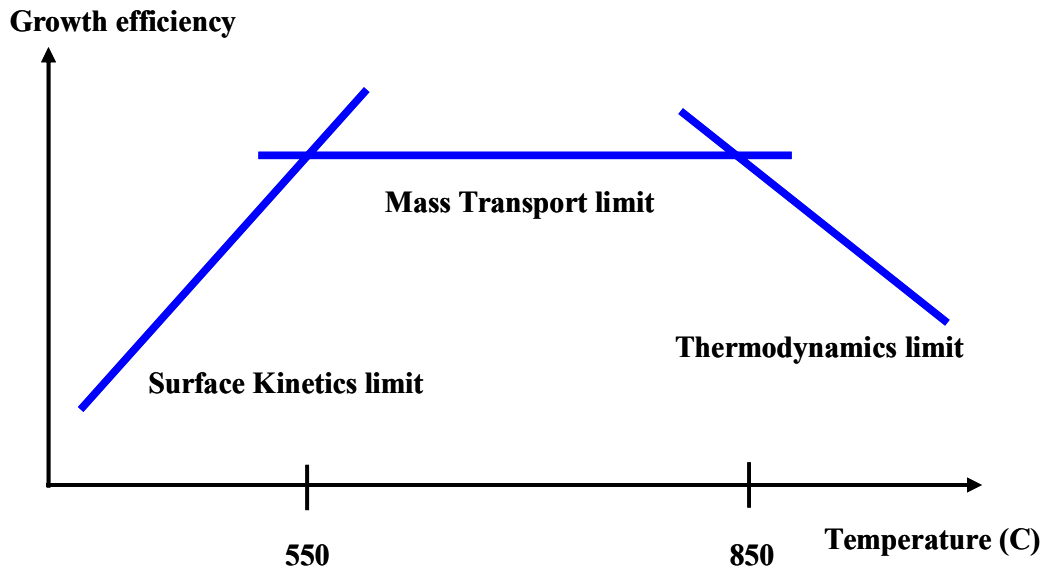
Growth efficiency

Figure 2.2 Growth efficiency as a function of temperature with three growth regimes.

Once unity pyrolysis efficiency is reached, generally for all temperatures greater than 500 ºC, a regime of mass transport limited growth is followed. This region is usually several hundred degrees Celsius. Diffusion is the major factor in this regime. The gas-phase diffusion coefficient of the alkyls is only weakly dependent on temperature but is moderated by the boundary layers which are generated by the hydrodynamics through the reactor chamber [27, 28].

At some still higher temperatures, the temperature of the gas becomes high enough and far enough above the surface where gas-phase pyrolysis of the hydrides becomes dominant and their solid particles can be formed without depositing on the substrate. Therefore, spontaneous gas phase nucleation, deposition on the reactor wall, and higher rate desorption of the reactant species disturb the desired deposition and reduce growth rate, as shown in Figure 2.2 [29].

14

2.3. MOCVD precursors for group III metals and nitrogen

Most sources have high vapor pressure and are delivered using carrier gases. These sources should be easily synthesized and purified and have reasonable vapor pressures. As seen in table 2, trimethyl and triethyl molecules are widely used for the group III precursors. TrimethylGallium (TMGa), trimethylaluminium (TMAl), and trimethylindium (TMIn) are commonly used. They have high vapor pressure at room temperature. Hence, these are transferred to the reactor with carrier gases.

Ammonia (NH_3) is usually used as the nitrogen source. The gas phase of ammonia has strong bond energy and a very high thermal stability, so a relatively high temperature is needed to decompose NH_3 [30]. However, ammonia prevents the deposited film from decomposing under this high temperature. In addition, hydrogen is commonly used as a carrier gas for MOCVD. But in some cases, for example GaN on ZnO growth, nitrogen should be substituted for hydrogen. But the nitrogen as the carrier gas should has high purity through the purification by an appropriate point of use purifier.
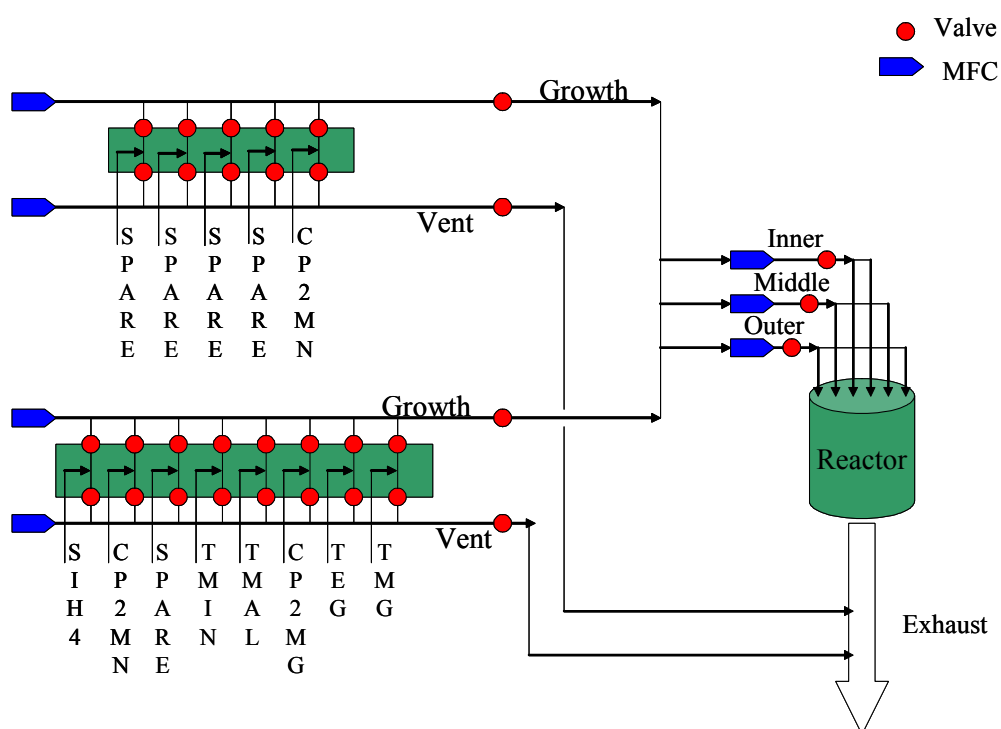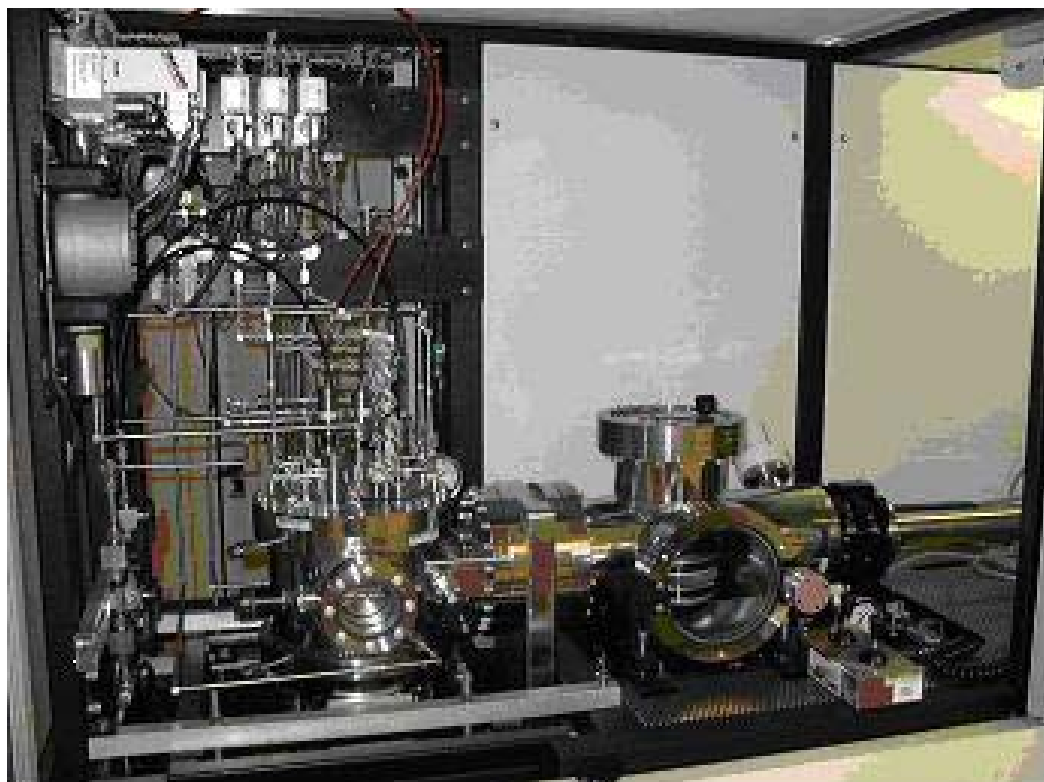
Figure 2.3 A photograph and gas flow schematic of a highly modified vertical MOCVD growth tool.

2.4. MOCVD equipment

MOCVD growth is facilitated by introducing group III precursors and ammonia with carrier gases into a reactor at appropriate temperature and deriving growth processes as seen in Figure 2.3. A typical MOCVD system consists of four major parts; gas delivery system, reactor, heating system, and exhaust system.

2.4.1 Source pick-up and gas mixing system

The gas delivery system includes all of the valves, MFCs, regulators, and equipment for transporting sources to the reactor chamber. Thus, it is important to control the gas flows, mixtures, and distribution into the chamber as well as to be clean and leak tight.

2.4.2 Reactor chambers

The reactor system (comprising the reaction chamber and all associated equipment) for carrying out CVD processes must provide several basic functions to all types of systems. It must allow reactants and diluent gases to move to the reaction site and provide activation energy to the reactants (heat, radiation, plasma) while maintaining a specific system pressure and temperature. Moreover, the reactor allows the chemical processes for film deposition to proceed optimally and to remove the by-product gases and vapors. These functions must be implemented with adequate control, maximal effectiveness, and complete safety.

The reaction chamber is the vessel in which the source gases are mixed and introduced into a heated zone where an appropriate substrate is located, and then the basic pyrolysis reactions described above take place. There are two basic reaction chamber geometries [13, 31] commonly used for MOCVD growth, which have a number of design features in common. Both designs are cold-wall systems that reflect the basic pyrolysis nature of the process. They contain a relatively small diameter inlet into some form of transition region and make use of an indirectly heated (radio-frequency induction heated or infrared radiant heated) silicon carbide-coated graphite susceptor. The chamber itself can be quartz, stainless steel, or quartz-lined stainless steel.

(a)   (b)
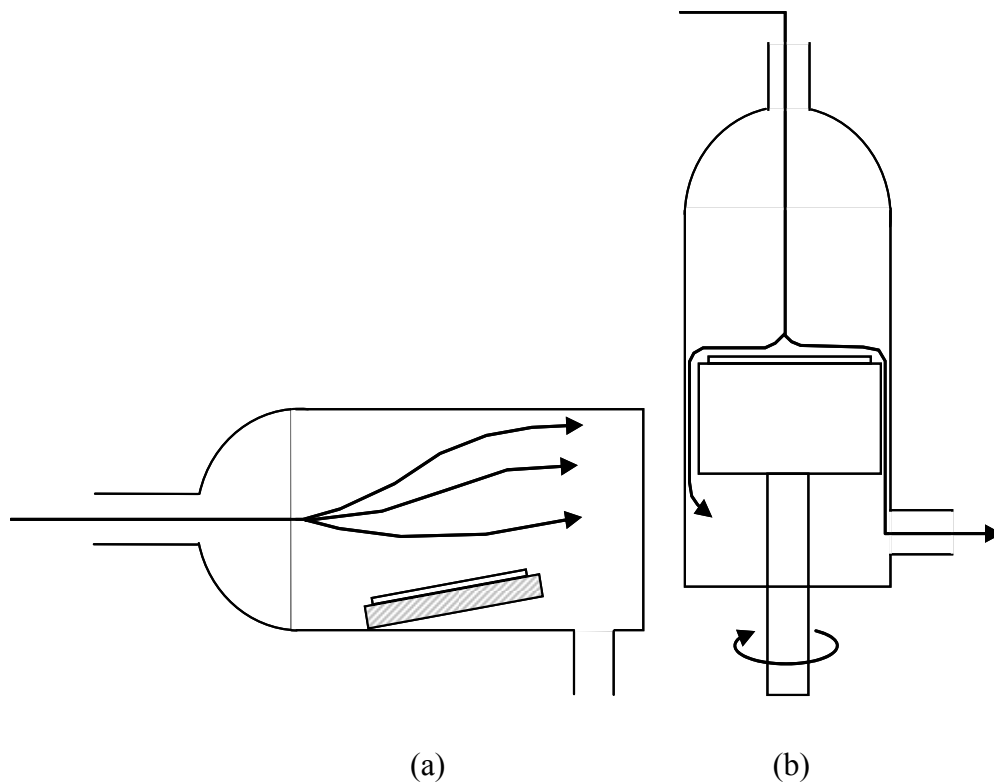
Figure 2.4 Two typical reaction chamber geometrics for MOCVD growth
(a) horizontal reactor chamber and (b) vertical reactor chamber.

In the horizontal reaction chamber [see Figure 2.4 (a)] the process gases enter from the small inlet to the left and expand to an approximately laminar flow across the heated susceptor, which is tilted by a small angle to account for reactant depletion. Multiple wafers can be accommodated along the length of the susceptor, or even side by side if the susceptor width is large enough. Uniformity can be improved by incorporating a rotating disk. However, in the vertical reaction chamber [see Figure 2.4 (b)], the process gases enter at the top and are deflected by a baffle before moving downward through a cold transition region and approaching normal to the heated susceptor. The gas flow is forced to the sides by the susceptor with a velocity profile dependent on geometry and affected by the thermal profile in the system. Better uniformity is obtained by rotating the susceptor. Exhaust gases escape through the base of the reaction chamber. Large susceptors can accommodate multiple wafers.

2.4.3 Other systems

The substrate, where film is deposited, is placed on a heated susceptor. There are three ways to heat the susceptor: RF (radio frequency) induction heating, radiative heating, and resistance heating. In the resistance heating type, electric current supplies heat energy to the susceptor which is usually made with graphite.

Safety is the most important issue in MOCVD because of various toxic gases used as sources. Process gases should be piped in leak-free coaxial tubing with an inert purge gas or vacuum in the outer tube. Adequate exhaust hoods and cabinets should be used to contain the growth apparatus itself. Waste gases should be processed with filters,

19

combustion discharge, oxidation, wet chemical scrubbing, or a combination of these methods. Automatic shutdown of source gases and a switch to inert purge gases should take place in the event of power failure when inadequate backup power is available. In addition, adequate toxic- and flammable-gas monitoring should be provided at all points along the process chain, including attics, halls, labs, cabinets and hoods, purge lines, and effluent gas lines.

Table 2.1 List of MO sources.

Compound		P at 298 K (torr) Log P = B – A/T	A	B	Melt Point (°C)
$(CH_3)_3$ Al	TMAl	14.2	2780	10.48	15
$(C_2H_5)_3$ Al	TEAl	0.041	3625	10.78	-52.5
$(CH_3)_3$ Ga	TMGa	238	1825	8.50	-15.8
$(CH_3)_3$ In	TMIn	4.79	2530	9.19	-82.5
$(C_2H_5)_3$ In	TEIn	0.31	2815	8.94	-32
$(C_2H_5)_2$ Zn	DEZn	8.53	2190	8.28	-28
$(C_5H_5)_2$ Mg	Cp$_2$Mg	0.05	3556	10.56	175

Moreover, Figure 2.5shows a schematic of source bubbling and metal organic (MO) sources in Table 2.1, which are commonly utilized to grow III-nitride materials using MOCVD.
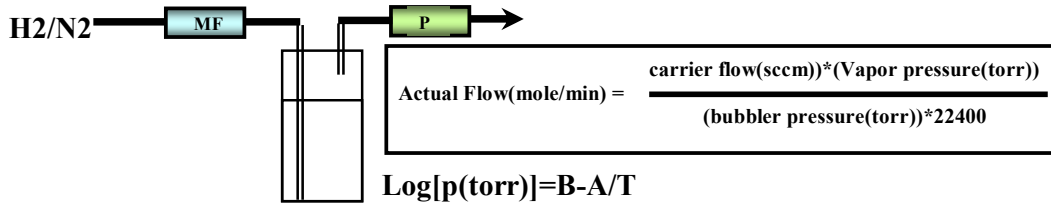
Figure 2.5 Schematic of source bubbling.

2.5. III-Nitride MOCVD growth

Table 2.2 Melting temperatures and decomposition N_2 pressures for A1N, GaN and InN.

III-nitride	T_{melt} (°C)	E_{bond} [eV]	P_{dec} (Torr)
AlN	~ 3500	11.52	0.2E7
GaN	~ 2800	9.12	3.4E7
InN	~ 2200	7.72	4.5E7

A1N, GaN and InN are semiconductor materials with a large direct energy gap which attracts a lot of interest for wide ranges of wavelength optoelectronics and high temperature electronic applications [32. 33]. However, bulk crystals of these nitrides cannot be obtained by the well-known methods such as Czochralski or Bridgman growth from stoichiometric melts due to extremely high melting temperatures and very high

decomposition pressures at melting (see Table 1) [34-36]. However, for most semiconductor materials, high quality growth would be practically impossible at these conditions. Therefore, the crystals have to be grown by methods requiring lower temperatures. MOCVD growth is the most common technique for these materials.

2.5.1 GaN MOCVD growth

GaN is by far the most heavily studied of all the III-nitrides. In the past, many researchers have suffered from large background n-type carrier concentrations, the lack of a suitable substrate material, difficulties with GaN p-type doping, and processing difficulties. However, modern researchers have improved crystal quality and processing technology to overcome many of these difficulties. Many research groups have consistently achieved high quality GaN with n-type background concentrations as low as 4×10^{16} cm^{-3}. One group has developed a process for obtaining p-type GaN which allowed them to demonstrate the first pn junction LED. Currently, GaN-based devices have prevailed in optoelectronic and electronic applications.

2.5.1.1 Various properties of GaN

GaN, which has a high thermal stability, allows high temperature processes using MOCVD. Its structure is wurtzite type with lattice constants, a-spacing = 3.189 Å and c-spacing = 5.185 Å [37]. Room temperature mobility of unintentionally doped GaN is less than 1000 cm^2/Vs. In addition, optical properties of GaN give interest for its potential as a blue and ultraviolet light emitter. GaN has a direct bandgap energy of 3.44 eV.

2.5.1.2. MOCVD growth process

      Since bulk GaN substrate is not common yet, most crystal GaN films are grown on substrates of foreign materials, which results in lattice mismatch leading to s major barrier for GaN growth. A (0 0 0 1) c-plane sapphire is commonly used as a substrate which is suitable for high temperature processes (over 1000 ºC). In MOCVD GaN growth, TMGa or TEGa is used as a group III precursor and NH_3 is the group V source. A normal GaN growth process has a two-step process which is a low temperature buffer followed by high temperature GaN growth. Figure 2.6 (a) shows the growth process according to growth temperature changing.

① Pre-baking substrate: chamber temperature ramps up to 1100 ºC and the substrate is heated for 3 ~ 4 minutes under a hydrogen ambient. From this process, the substrate is reorganized and has a good surface quality. Ammonia is introduced, which leads to a nitridation of the substrate surface and improves crystal quality of the following layers.

② Low temperature buffer growth: after the pre-baking, the temperature ramps down to 550 ºC. A GaN or AlN buffer layer is deposited on the substrate at that relatively low temperature for a couple of minutes. Growth of a low temperature buffer has some merits: it improves crystalline quality and electrical properties by decreasing residual n-type background concentrations which cause production of intrinsic defects from nitrogen vacancies. Reducing the residual donor also decreases the possibility of extrinsic impurities resulting from vacancy generation. In addition, the mobility is improved. Therefore, buffer thickness is the most important factor affecting GaN layer quality. The thickness, generally between 20 ~ 40nm, can be controlled by precursor flows.
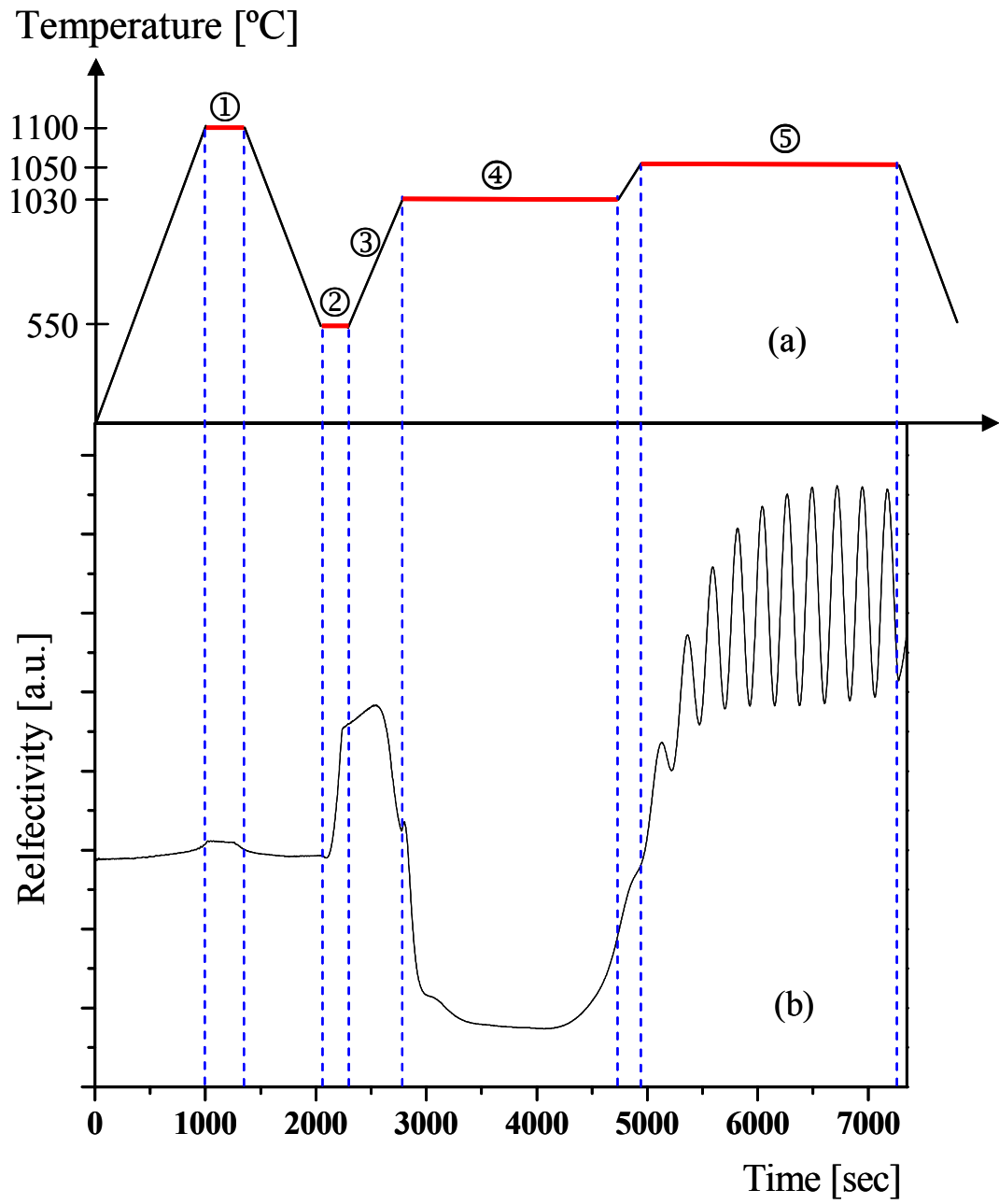
Figure 2.6 (a) in-situ measurement data and (b) sketch of the growth process with growth temperature during GaN growth.

③ Thermal activation of the buffer layer: the buffer layer's crystal quality is poor due to low temperature growth. The buffer layer is recrystallized while ramping the temperature to 1030 ºC under ammonia ambient. These two buffer processes result in strain relief caused by lattice mismatch from the substrate and high density of nucleation which will be seeds for GaN growth.

④ Rough GaN growth: before the main GaN layer growth, a rough GaN layer is grown at 20 ºC lower growth temperature than the main GaN growth, and the growth rate is also lowered. This process improves the main GaN crystal quality proven by X-ray diffraction measurements.

⑤ GaN growth : the main GaN layer is grown at around 1050 ºC. The general growth rate in MOCVD growth is ~2μm/hour which is mainly affected by growth temperature and V/III molar ratio.

Moreover, the MOCVD machine has an *in-situ* characterization tool capable of monitoring the growth processes in real time using normal incidence reflectometry. The overall reflectivity determining growth rate and growth status results from overlapping the reflectance of light from different interfaces. As the layer grows, the interference conditions change, causing the sample reflectivity to oscillate with a frequency determined by the growth rate, the incident wavelength, and refractive index of the layers. Figure 2.6 (b) shows the *in-situ* measurement data during GaN growth.

<u>2.5.1.3 Growth conditions and their effects</u>

The major process parameters to influence GaN film are growth temperature, V/III ratio, and growth rate. In order to obtain good crystalline quality, a general growth temperature for MOCVD GaN is around 1050 ºC with TMGa precursor, even though some groups grow using TEGa and NH_3 at 400 ~ 650 ºC [38]. However, it has been found that the growth temperature influences the optical quality of GaN, especially yellow luminescence between 500 and 600 nm. The lower growth temperatures lead to higher defect density because the possibility of impurity incorporation increases when the growth temperature is reduced. Whereas, excessively high growth temperature could alter surface kinetics of growth mechanisms, contributing to desorption or decomposition rather than film deposition.

In GaN growth, a nitrogen vacancy is referred to as one electron and a gallium vacancy as three holes [39]. These vacancies affect electrical properties. Usually, more impurities are incorporated into sublattices as the density of intrinsic defects increases. The V/III ratio mainly influences electrical properties of GaN. This ratio is the crucial factor to change material stoichiometry which is determined by existence of vacancies or interstitial atoms. When the V/III ratio increases, the concentration of nitrogen vacancy increases and the concentration of gallium vacancy decreases. An interaction between these two kinds of vacancies determines the carrier mobility. However, an excessively high V/III ratio restricts gas phase reactions, resulting in degraded crystalline quality of GaN. This ratio also affects the optical properties related to impurity incorporation, just as the growth temperature does.

2.5.1.4 Ex-situ characterization

Ex-situ characterization is important to analyze material quality, to optimize growth parameters, and to predict device performance prior to device fabrication. Photoluminescence (PL), cathodluminescence (CL), and electroluminescence (EL) are powerful *ex-situ* characterization methods utilized for optical properties. Hall, four point probe and I-V curve measurements characterize electrical properties. Microscope, scanning electron microscopy (SEM), and atomic force microscopy (AFM) are used for surface morphology. X-ray diffraction (XRD), transmission electron microscopy (TEM), Raman spectroscopy, x-ray photoelectron spectroscopy (XPS), Auger spectroscopy, energy dispersive X-ray spectroscopy (EDX), and Rutherford backscattering spectroscopy (RBS) are employed for crystalline quality and interface analysis.
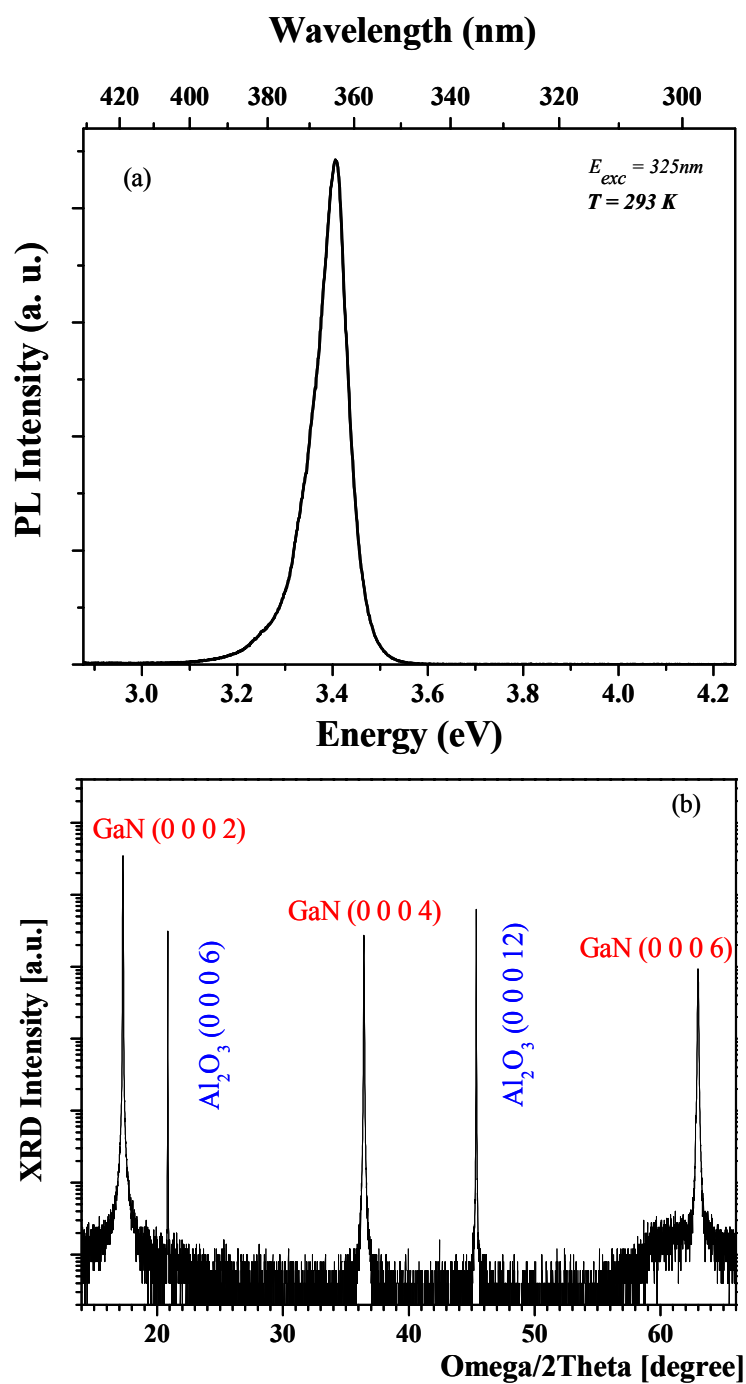
Figure 2.7 (a) PL data and (b) XRD data on 1 μm-thick GaN grown on a sapphire substrate using MOCVD.

PL is the common optical characterization for GaN. PL is the process of radiative recombination of carriers generating light emission when the carriers are excited. PL provides information about the relationship between the intensity and the wavelength of the emission of radiation. As seen in Figure 2.7 (a), a visual GaN peak is located at around 364 nm, where the band to band recombination process occurs. However, there are several processes: donor to valence band transition, conduction band to acceptor transition, and donor to acceptor pair transition which can be easily observed by measuring at low temperatures.

XRD is a widespread analytical tool for the non-destructive characterization of compound structure. The reflected diffraction pattern from the epilayer determines a-spacing and c-spacing lattice constants of a material according to Bragg's law. The linewidth of rocking curve, i.e. full width at half maximum (FWHM), determines the crystalline quality. Figure 2.7 (b) shows a wide scan of GaN along the c-axis. This evaluates the c-spacing of GaN, 5.18 Å and a relative scan along the a-axis provides the a-spacing, 3.18 Å. In addition, a rocking curve scan on an a-axis or c-axis estimates crystalline quality. MOCVD growth gives FWHM between 200 ~ 300 arcsec from XRD peak on (0 0 0 2) reflection plane of GaN.

AFM is a prevalent characterization to examine surface morphology of a material. In AFM, a flexible cantilever with a keen-edged tip drags over the sample surface in the XY plane and detects the interaction force between the tip and the sample.   A laser beam is focused on the back of the cantilever and bounced off towards a photodiode detector which is used to detect the deflection of the cantilever. The minute changes in the deflection of the cantilever caused by the varying interaction forces between the apex of

the tip and the sample are detected via the photodiode detector. Current signals from the

segmented photodiode are used as a sensitive measure of the forces experienced by the

scanning cantilever and as a means of generating height data, i.e., in the Z scale. As seen

in Figure 2.8, An AFM image of GaN shows a step-flow surface morphology which is

usually observed in MOCVD growth, and a general value of RMS (root mean square)

surface roughness for GaN grown by MOCVD is around 3~5 Å. Black holes in the image

are defects in GaN, i.e. dislocations which are normally between 10^8 and 10^{10} cm^{-2}. In the

next chapter, we will discuss dislocation determination in III-nitride materials. In addition,

Hall effect measurement is the tool to characterize electrical properties obtained by

doping concentration, mobility, and resistivity.
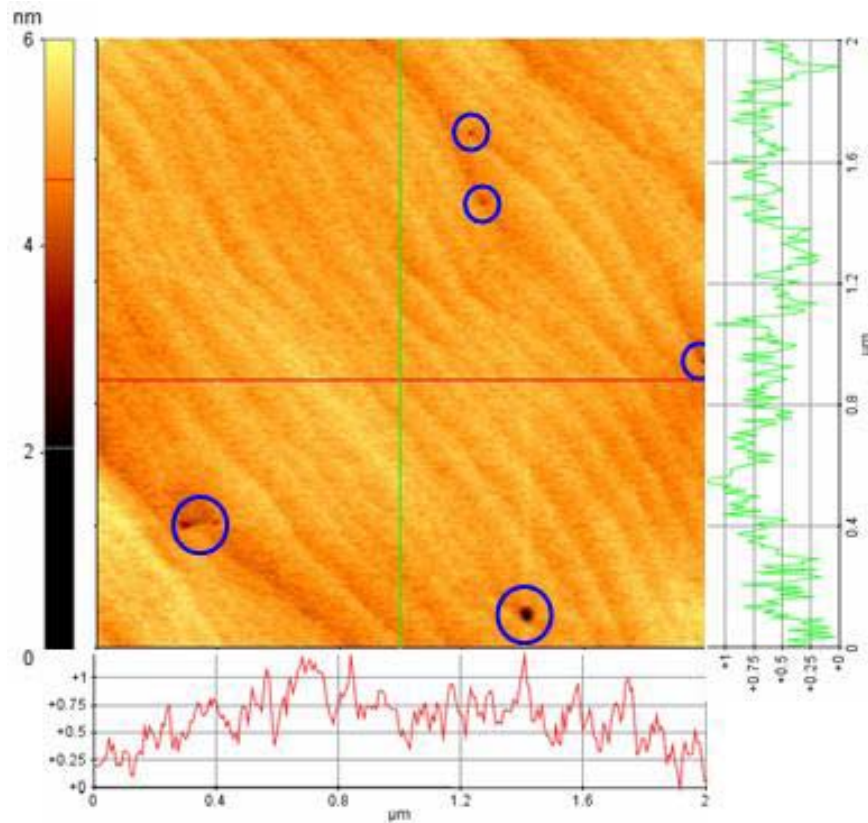
Figure 2.8 A 2μm*2μm AFM image of GaN grown by MOCVD.

2.6 References

[1] S. Nakamura, M. Senoh, N. Iwasa, S. Nagahama, Jpn. J. Appl. Phys. 34 (1995) L797.

[2] S. Nakamura, M. Senoh, S. Nagahama, N. Iwasa, T. Yamada, T. Matsushita, H. Kiyoku, Y. Sugimoto, Appl. Phys. Lett., 8 (1996) 2105.

[3] H. Manasevit, *J*. Cryst. Growth, 55, (1981) 1.

[4] J. Duchemin, J. Vac. Sci. Technol., 18, (1981) 753.

[5] S. Hersee and J. Duchemin, Ann. Rev. Mater. Sci., 12, (1982) 65.

[6] P. Dapkus, Ann Rev. Mater. Sci., 12, (1982) 243.

[7] G. B. Stringfellow, *"Organometallic vapor-phase epitaxial growth of III–V semiconductors,"* in Semiconductors and Semimetals, W. T. Tsang, Ed. New York: Academic, 1985.

[8] M. Razeghi, "*Low-pressure metallo-organic chemical vapor deposition of $Ga_xIn_{1-x}As_yP_{1-y}$ alloys*," in Semiconductors and Semimetals, W. T. Tsang, Edited. New York: Academic, 1985.

[9] J. Coleman and P. Dapkus, "*Metalorganic chemical vapor deposition*," in Gallium Arsenide Technology, D. K. Ferry, Ed. Indianapolis, IN: Sams, 1985.

[10] L. Miller and J. Coleman, CRC Crit. Rev. Solid State Mater. Sci., 15, (1988) 1.

[11] P. Dapkus and J. Coleman, "*Metalorganic chemical vapor deposition*," in III–V Semiconductor Materials and Devices, R. J. Malik, Ed. Amsterdam: North-Holland, 1989.

[12] G. B. Stringfellow, "*Organometallic Vapor-Phase Epitaxy*". New York: Academic, 1989.

[13] H. Manasevit, Appl. Phys. Lett., 12 (1968) 156.

[14] H. Manasevit and K. Hess, J. Electrochem. Soc., 126 (1979) 2031.

[15] J. Karpinski, J. Jun, and S. Porowski, J. Crystal Growth 66 (1984) 1.

[16] M. Ohring, " Materials Science of Thin Films, Deposition and Structure", San Diego, Academic, 2002.

[17] S. Porowski, I. Grzegory , J. Crystal Growth 178 (1997) 174.

[18] D. Reep and S. Ghandhi, J. Electrochem. Soc., 130 (1983) 675.

[19] Y. Mori and N. Watanabe, J. Appl. Phys., 52 (1981) 2792.

[20] C. Mitchell, E. Michael, and J. Han, J. Crystal Growth 222 (2001) 144.

[21] Y. Galeuchet, P. Poentgen, and V. Graf, Appl. Phys. Lett., 68 (1990) 560.

[22] W. Holstein and J. Fitzjohn, J. Crystal Growth 94 (1989) 145.

[23] L. Giling, J. Electrochem. Soc., 129 (1982) 634

[24] F. Durst, L. Kadinskii, M. Peric, M. Schafer, J. Crystal Growth, 125 (1992) 612.

[25] A. McGinnis, D. Thomson, R. Davis, E. Chen, A. Michel, and H. Lamb, Surface Science, 494 (2001) 28.

[26] N. Ingle, C Theodoropoulos, T. Mountziaris, R. Wexler, and F. Smith, J. Crystal Growth, 167 (1996) 543.

[27] D. Shaw, in *Crystal Growth Theory and Techniques Vol. 1* edited by C. Goodman, Plenum, New York 1974.

[28] L. Donaghey, in *Crystal Growth*, edited by B. Pamplin, Oxford Univ. Oxford, 1980.

[29] G. Costrini and J. J. Coleman, *J. Appl. Phys.,* vol. 57, p. 2249, 1985.

[30] V. Ban, J. Electrochem. Soc., 119, p761, 1972.

[31] S. J. Bass, *J. Cryst. Growth,* vol. 44, pp. 29–33, 1978.

[32] S. Pearton, J. Zolper, R. Shul, and F. Ren, J. Appl. Phys. 86 (1999) 1.

[33] O. Ambacher, J. Phys. D 31 (1998) 2653

[34] A. Kinoshita, H. Hirayama, M. Ainoay, A. Hirata, and Y. Aoyagi, Appl. Phys. Lett., 77 (2000) 175.

[35] J.A. Van Vechten, Phys. Rev. B 7 (1973) 1479.

[36] J. Karpinski, J. Jun and S. Porowski, J. Crystal Growth 66 (1984) 1.

[37] H. Maruska and J. Tietjen, Appl. Phys. Lett., **15**, 327 (1969).

[38] A. Dissanayake, J. Lin, H. Jiang, Z. Yu, and J. Edgar, Appl. Phys. Lett., **65**, (1994) 2317.

[39] J. Neugebauer and C. Vandewalle, Mat. Res. Soc. Symp. Proc., **395**, 645 (1996).

CHAPTER 3

THREADING DISLOCATIONS IN III-NITRIDES

3.1 Introduction

III-nitrides have been reported as prospective materials for semiconductor device applications for a wide range of wavelengths. The wurtzite structures of GaN, AlN, and InN form a continuous alloy system with a direct bandgap ranging from 0.7 eV for InN to 3.4 eV for GaN to 6.2 eV for AlN. Thus, these nitride materials can potentially be fabricated into devices which are active at wavelength ranging from the red to the ultraviolet [1, 2].

However, high quality III-nitrides are more difficult to produce compared to the standard III-V compounds due to the absence of coherently matched substrates, like bulk GaN. The most common substrate used for GaN growth is sapphire which has a lattice mismatch of 16% [3]. The high dislocation densities resulting from this lattice mismatch may be detrimental to light output efficiency with optoelectronic semiconductors.

The dislocation densities act as a line defects. The line of dislocation moves along the core of the dislocation, where the distortion with respect to a perfect lattice is greater [4]. These dislocations significantly reduce the efficiency and lifetime of optoelectronic devices due to formation of non-radiative recombination centers or carrier leakage.

3.2 Hexagonal wurtzite structure and dislocation densities
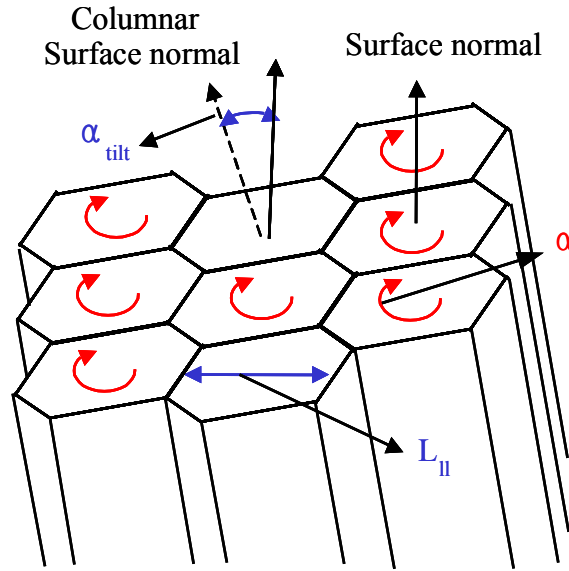
Figure 3.1 Hexagonal columnar structure of GaN.

The III-nitride is formed with different crystalline orientations (i.e. grains) that are misaligned to each other. The structure of the single crystalline III-nitride is known as a hexagonal columnar structure (i.e. mosaic structure). As shown in Figure 3.1, the hexagonal columnar structure of GaN has three different parameters: the tilt angle, α_{tilt}; the twist angle, α_{twist}; and the lateral coherence length, L_{ll}.   The tilt angle is out-of-plane misorientation, and the twist angle is in-plane misorientation. Thus, these two angles are called angular misorientations. However, the lateral coherence length is a finite length component parallel to the surface, and it can be a physical scale used to evaluate the columnar structure. These three parameters are crucial in calculating threading

dislocation density [5, 6].
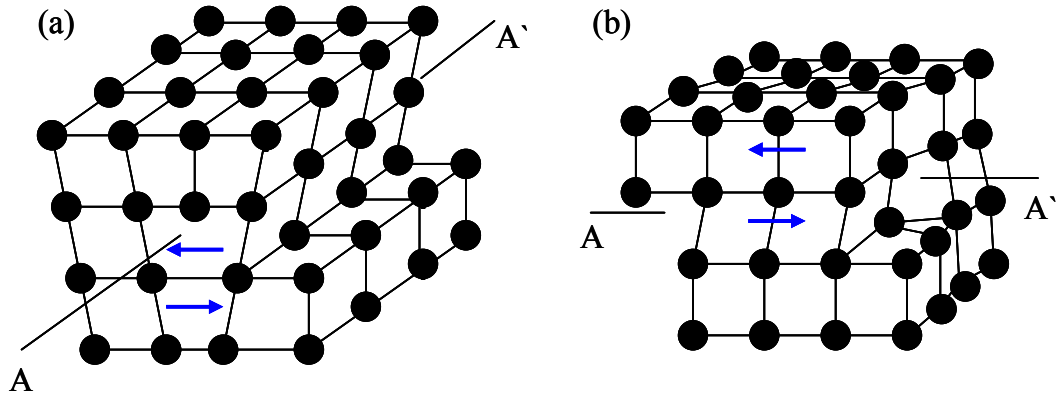
Figure 3.2 Two types of dislocations; (a) edge and (b) screw dislocation.

There are three types of threading dislocations; screw dislocation along the c-axis, edge dislocation in the a-axis and a mixed edge and screw dislocations. As seen in Figure 3.2, the screw dislocation has its Burgers vector (i.e, a unit vector tangent of the dislocation line) parallel to the dislocation line. The Burgers vector of the edge dislocation is perpendicular to the dislocation line. And the mixed dislocation has characteristics of both edge and screw dislocations. In this chapter, effects of the dislocation, its measurement methods, and techniques to reduce the dislocation are introduced.

3.3. XRD techniques to determine dislocation densities

Typical methods for determining dislocation density are transmission electron

microscopy (TEM) and atomic force microscopy (AFM). TEM is a destructive and difficult technique while AFM is a non-destructive surface morphology technique but it can not characterize inside the sample [7, 8].

XRD (X-Ray Diffraction) is another easy non-destructive technique used to characterize the structures of films. This technique is based on Bragg's law, $n\lambda=2d\sin\theta$, where n is an integer, λ is the wavelength of the x-ray source, d is the lattice spacing, and θ is the Bragg angle. Every crystal material has a unique lattice constant corresponding to a unique Bragg angle.

3.3.1 Williams-Hall Plot

We can determine the quality of the crystal material from a rocking curve scan of XRD. A narrower width of the x-ray spectrum indicates a higher crystal quality. The deviation between the experimental and theoretical Bragg's angles reveals strain in the film. Two XRD techniques: Williamson-Hall (WH) plot and reciprocal space mapping (RSM) are performed to determine the geometric size of the hexagonal columnar structure, resulting in an estimate of the dislocation density. RSM is normally used for detailed characterization of such crystalline structures. The WH plot, however, is a quicker and simpler method.

L_{ll} and α_{tilt} can be obtained through the use of WH plots. Broadening of the rocking curve scan on symmetric reflections is affected only by L_{ll} and α_{tilt}. WH plots make it possible to distinguish these two broadening mechanisms. As shown in Figure 3.3 (a), $\beta_\omega(\sin\theta)/\lambda$ is plotted against $(\sin\theta)/\lambda$ for each reflection, and a straight line is fitted. In this plot, the y-intersect (Y_o) of the fitted line is used to estimate the lateral coherence

(a)

$\beta_\omega * \sin\theta / \lambda$

(0006)

(0004)

slope of the line
$\Rightarrow \alpha_{tilt}$

(0002)

$L_{ll} = 0.9 / (2Y_o)$

Y-intercept of the line, Y_o

$\sin\theta / \lambda$

Layer Surface

(b)

Reflection
Plane

L_{tilt}

L_{coh}

Surface Normal

To the origin
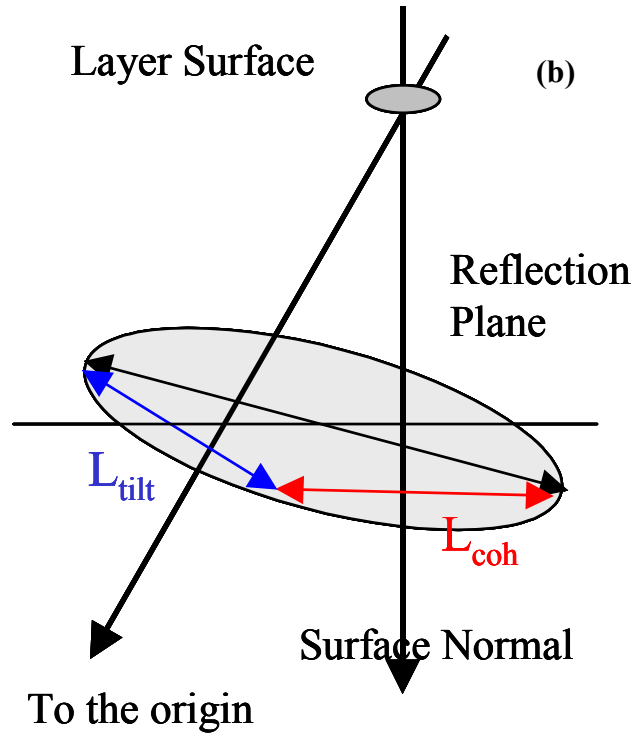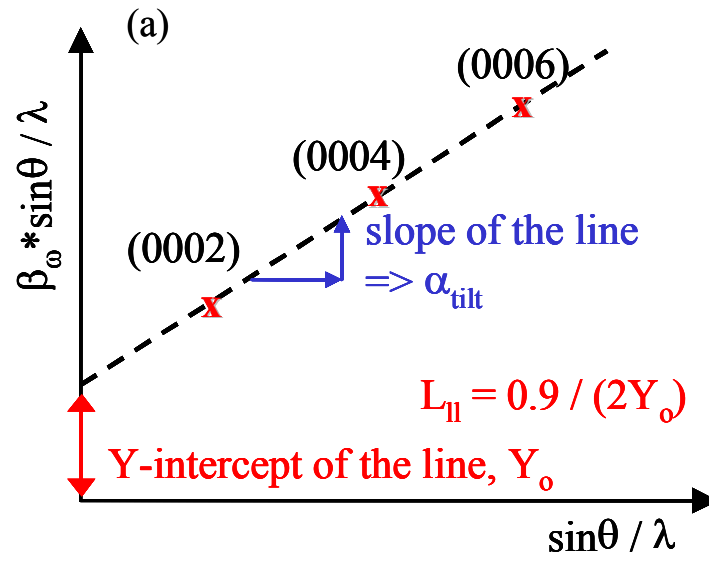
Figure 3.3 (a). Schematic of WH plot and (b) Schematic of RSM on an asymmetric
reflection.

length, L_{ll} (= 0.9 / 2Y$_o$), where β_ω, θ, and λ are the integral width of the measured profile, the Bragg reflection angle, and the x-ray wavelength, respectively [5, 6, 9, 10]. In addition, the slope of the fitted line corresponds to the tilt angle, α_{tilt}. These values obtained from WH plots will be used later to calculate dislocation densities.

3.3.2 Reciprocal Space Mapping

Secondly, RSM on a reflection plane can be plotted by recording equivalent intensities from a series of rocking curve scans with respect to the 2Θ direction. RSM is used to obtain information about the columnar structure since the linewidths of these scans are broadened according to L_{ll}, α_{tilt}, and α_{twist} of the columnar structure. As illustrated in Figure 3.3 (b), L_{ll} is the reciprocal of the full width at half maximum (FWHM) component parallel to the surface, L_{coh}, in the RSM on an asymmetric reflection. Similarly, α_{tilt} is the vertical component of the FWHM ellipse from the RSM of a symmetric reflection plane. Lastly, from the RSM on reflection planes in the a-axis direction, the vertical component of the FWHM ellipse is α_{twist} [11-13].

3.3.3 Dislocation densities

As mentioned above, the threading dislocations are classified into three different types; screw dislocations along the c-axis, edge dislocations in the a-axis, and mixed screw and edge dislocations. Screw and edge dislocation densities are distinguished by Burgers vectors: b_c = [0001] and b_a = ⅓ [11-20] respectively. WH plot or RSM method determine α_{tilt} which in turn finds the screw dislocation density, N_{screw}, expressed as [6, 14, 15]

$$N_{screw} = \alpha_{tilt}{}^2 / (4.35 \, |b_c|^2), \qquad\qquad (3.1)$$

The same is done with L_{ll} and α_{twist} to determine the edge dislocation density, N_{edge}, expressed as [6, 14, 15]

$$N_{edge} = \alpha_{twist} / (2.1 \, |b_a| \, L_{ll}), \qquad\qquad (3.2)$$

However, in this study, the mixed dislocation was not considered since pure screw and edge dislocation densities dominate the total dislocation density.

3.4. Dislocations in GaN

GaN, a typical III-nitride material for promising UV optoelectronic devices, is believed to have dislocations greater than 10^{10} cm^{-2} [5]. The investigation of defects in GaN gives us basic techniques and information to determine dislocation densities in III-nitrides.

All GaN samples were grown by MOCVD on (0 0 0 1) sapphire. TMGa, TMAl, and NH$_3$ were used as the source precursors for Ga, Al, and N, respectively. A 30nm low temperature (550 °C at 300 Torr) GaN nucleation layer was used for undoped GaN samples A, B, and C; 2.2, 1.9, and 2.2 um thick, respectively. The GaN epilayers were grown at 1050 °C with a V/III ratio of 4000 and a growth rate of ~2μm/h.

A reciprocal space mapping (RSM) of GaN A is shown in Figure 3.4 (a), from which lateral coherence length is determined as the reciprocal of L_{coh}. The α_{tilt} and α_{twist} are given by (0004) and (1-2 1 1) RSMs (not shown here), respectively. Furthermore, $L_{\parallel}$, α_{tilt}, and α_{twist} are determined in the same manner for GaN B and C. In addition, WH plots have also been used to extract values for $L_{\parallel}$ and α_{tilt} for these samples in Figure 3.4 (b). Values for α_{twist} were obtained directly from Φ-scans on asymmetric reflections.
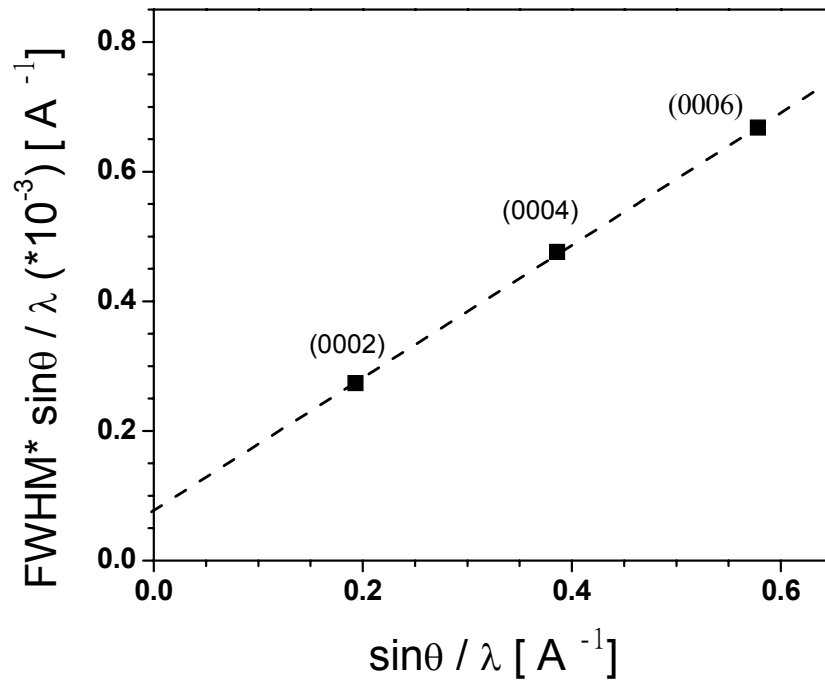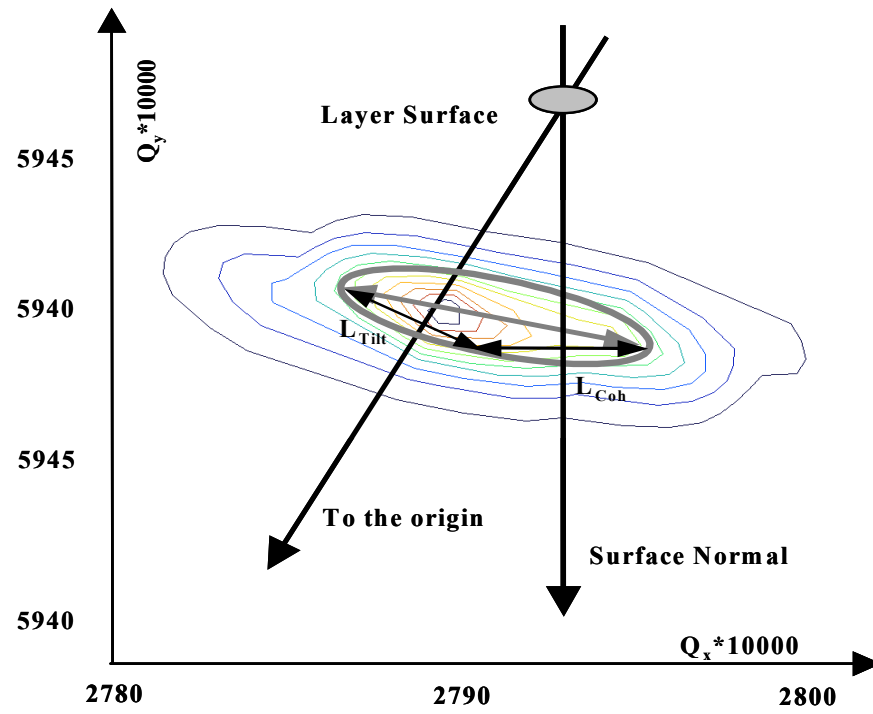
Figure. 3.4 (a) RSM and (b) W-H Plots for undoped GaN samples #1, #2, and #3.

Table 3.1 Summary of the mosaic structure factors of GaN samples #1, #2, and #3
        by various methods.

	Method	GaN #1	GaN #2	GaN #3
L_{ll} [um]	WH plot	0.82	0.58	0.48
	RSM	0.33	0.25	0.28
Tilt [aresec]	WH plot	216	211	308
	RSM	274	266	335
Twist [arcsec]	Φ scan	835	662	792
	RSM	792	655	702
N_{scew} [cm^{-2}]	WH plot	9.4E+07	9.0E+07	1.9E+08
	RSM	1.5E+08	1.4E+08	2.3E+08
N_{edge} [cm^{-2}]	WH plot	7.4E+08	8.3E+08	1.2E+09
	RSM	1.7E+09	1.9E+09	1.8E+09

The data for GaN obtained by both these techniques is summarized in Table 3.1. The mean N_{screw} with the Burgers vector ($|b_c|$=5.185 Å) and N_{edge} with the Burgers vector ($|b_a|$=3.189 Å) obtained using a WH plot have been compared with those obtained using RSM. The α_{tilt} values by WH are larger than those by RSM methods. This may be explained by annihilation of the defects with respect to the growth direction (i.e. c-axis) during the growth process [14, 15]. Since the tilt angle along the c-axis is relaxed during growth, the average α_{tilt} by WH is smaller than a transition α_{tilt} value by RSM. The mean L_{ll} value by WH is smaller than a transition L_{ll} value by RSM, since L_{ll}, a component length with respect to parallel to surface, is smaller as α_{tilt} gets larger. These differences lead to dissimilarity between two methods for N_{screw} and N_{edge} due to relaxation of defect during growth. The WH plot provides the mean size and angular distribution of the columnar structure from a combination of the (0002), (0004), and (0006) reflections,

while RSM provides a specific value from a specific reflection. Therefore, the WH plot may be expected to provide a more reliable estimate of the average values for the columnar structure of GaN, even though RSM measurements will provide more accurate information. It should be noted that the values obtained for N_{screw} and N_{edge} are less accurate than those typically measured by TEM and this is being investigated.[3] However, both the WH plot and RSM still allow a relative measure of material quality.

3.5. Dislocation densities in AlGaN

In order to form self-organized nanostructures it is necessary to understand the beginning of the growth process, especially nucleation, because growth modes are determined after the nucleation process. Nucleation also affects dislocation generation. Determination of dislocation densities in AlGaN grown on AlN reveals the nucleation process and growth mechanism for the future GaN nanostructure growth.

Numerous samples were investigated; however, this chapter focuses on a systematic series of $Al_xGa_{1-x}N$ samples (A, B, and C) with different Al molar fraction. All of the samples were grown by MOCVD on (0001) sapphire substrates. Trimethyl gallium (TMGa), trimethyl aluminium (TMAl), and ammonia (NH_3) were used as the source precursors for Ga, Al, and N, respectively. All three samples had the same structure of nucleation layers, consisting of a 30 nm low temperature AlN layer and an 80 nm high temperature AlN layer. The growth of these nucleation layers was followed by the growth of nominally undoped $Al_xGa_{1-x}N$ epilayers. These $Al_xGa_{1-x}N$ layers A, B, and C with Al compositions (x) of 0.48, 0.56, and 0.6 have thicknesses of 0.6, 0.36, and 0.45 μm, respectively.
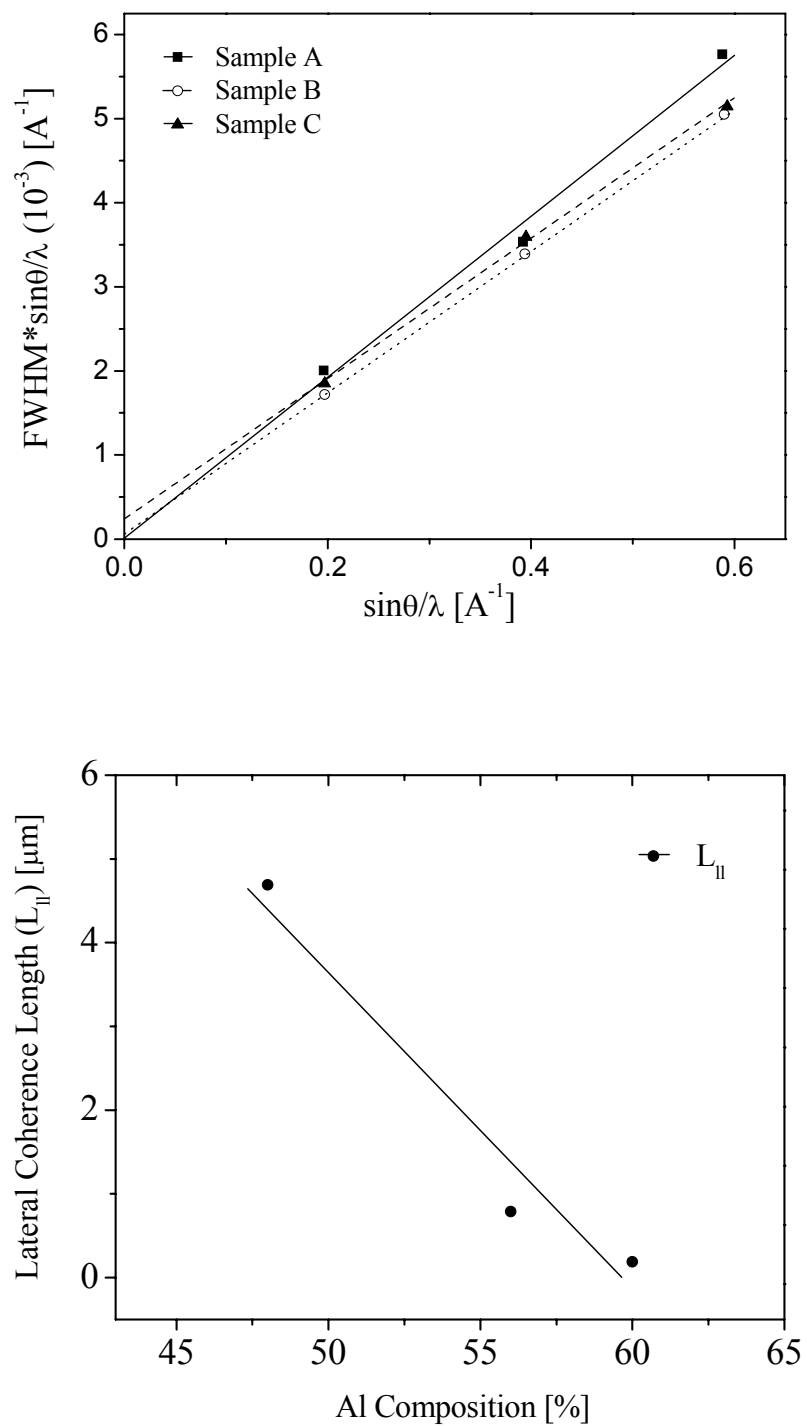
Figure 3.5 (a) Williamson-Hall plots for samples: A, B, and C (b) Lateral coherence length with Al composition.

Williamson-Hall plots for systematic series of samples highlighted in this work are shown in Figure 3.5 (a). Variation of FWHM of rocking curve measurements for the symmetric reflection planes depends on lateral coherence length and tilt angle. The linewidths of the rocking curve scan for all samples decreased with higher order reflections due to the lattice alignment (spacing).

The physical size of columnar structures depends on Al concentration in $Al_xGa_{1-x}N$ film. Figure 3.5 (b) shows variation of lateral coherence length with Al composition. The lateral coherence length associated with the edge dislocation decreases with Al composition due to the smaller lattice parameter of $Al_xGa_{1-x}N$. Investigation into the dependence of twist angle reveals that twist angle has a stronger effect to thickness than Al content in Figure 3.6 (a). However, Figure 3.6 (b) shows the dependences of tilt angle, a significant factor to determine screw dislocation density, on Al content and layer thickness of the film. The tilt angle decreased with higher Al content but increased with thicker layer.
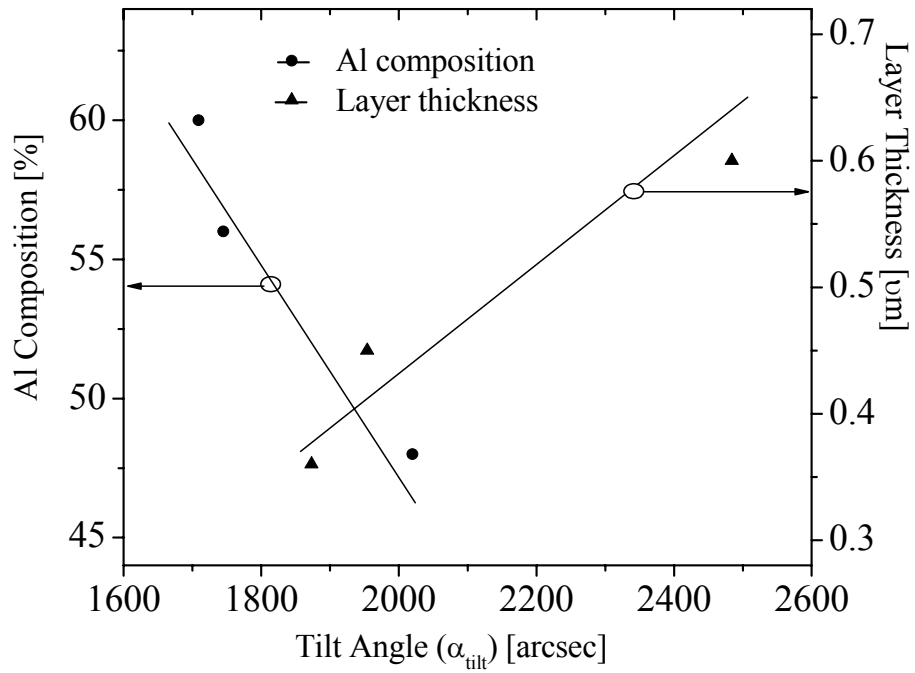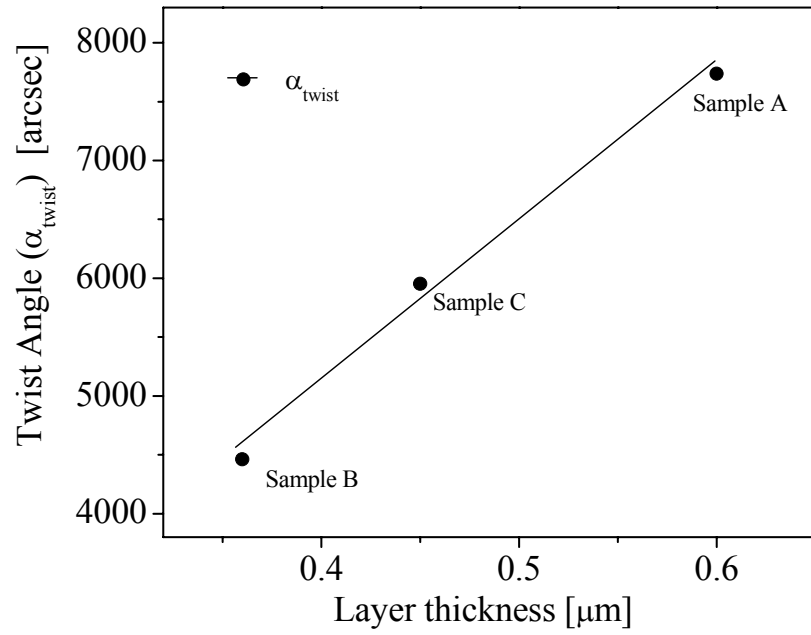
Figure 3.6 (a) Twist angle with thickness of $Al_xGa_{1-x}N$ layer. (b) Tilt angle with Al composition and layer thickness.
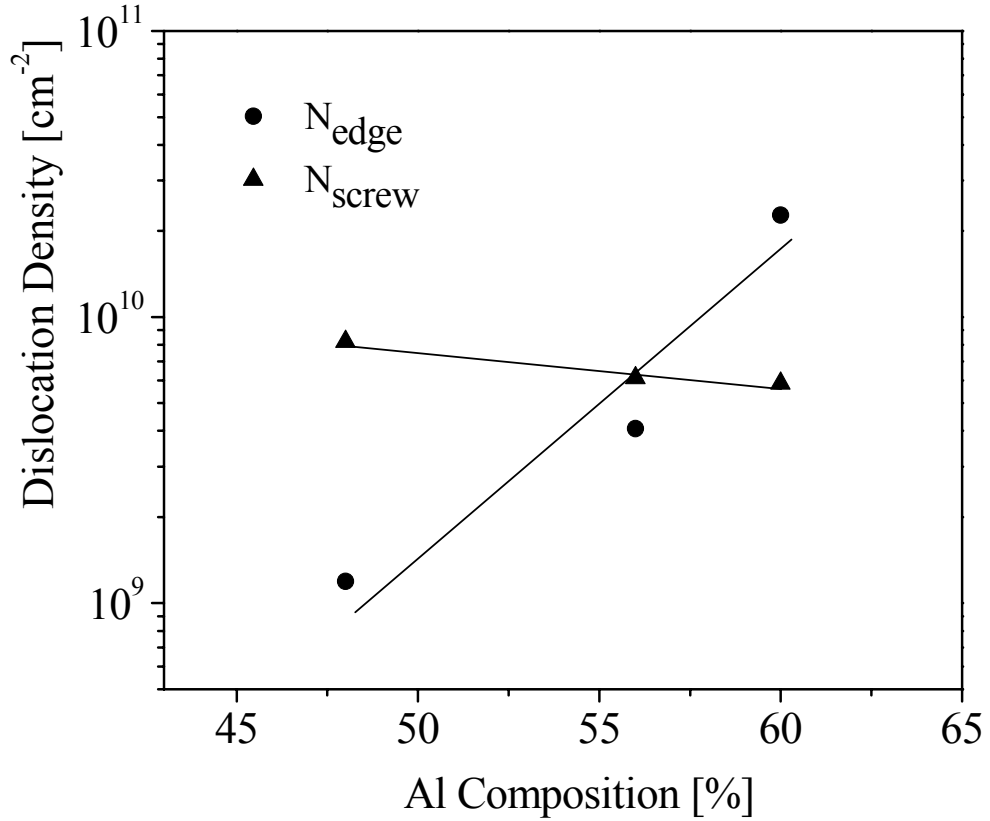
Figure 3.7 Screw and edge density with Al composition in the AlGaN grown by MOCVD.

The dislocation densities were calculated by estimation of α_{tilt}, α_{twist}, and L_{ll} of columnar structures obtained from Williamson-Hall technique, as shown in Figure 3.7. An $Al_xGa_{1-x}N$ film grown on AlN/Sapphire is compressively strained, since the lattice parameters of $Al_xGa_{1-x}N$ are larger than the underlying AlN layer and sapphire substrate. Therefore, the a-lattice parameter and lateral coherence length decreases as Al composition increases. Moreover, smaller lateral coherence length causes smaller grain area (i.e. c-plane face of columnar structure) for quantitative estimation of edge dislocation. Therefore, the edge dislocation increases as Al composition increases. On

the other hand, the c-lattice parameter of $Al_xGa_{1-x}N$ is elongated due to compressive strain in $Al_xGa_{1-x}N$. The c-lattice parameter increases as Al composition increases. The screw dislocations along c-direction are caused by vertically tilt boundary, but they are normally decreased during growth. Therefore the screw dislocation is reduced with higher Al composition. However, the total threading dislocation density increases with higher Al compositions.

Table 3.2 Summary of the mosaic structure factors of $AlxGa_{1-x}N$ by these two methods.

	Methods	Sample A	Sample B	Sample C
L_{ll} [um]	WH plot	4.69	0.79	0.19
	RSM	0.41	0.53	0.37
Tilt [arcsec]	WH plot	2020	1745	1709
	RSM	2484	1873	1954
Twist[arcsec]	Φ scan	7736	4460	5952
	RSM	7157	4323	5724
N_{screw} [cm^{-2}]	WH plot	8.20E+09	6.12E+09	5.87E+09
	RSM	1.24E+10	7.05E+09	7.68E+09
N_{edge}[cm^{-2}]	WH plot	1.19E+09	4.08E+09	2.27E+10
	RSM	1.25E+10	5.87E+09	1.11E+10

In Table 3.2, the data obtained by two different techniques is summarized. Although there is good agreement between the trends observed by both techniques, there is a discrepancy between the absolute numbers. This is due to the interpolation of c-spacing parameters of columnar structure by the Williamson-Hall plot, whereas RSM

gives specific values for columnar structure on a specific reflection plane. In Williamson-Hall plot, the columnar structure parameters are determined by estimating a trend among different reflection planes, but in RSM, a specific value on a specific reflection plane is used to estimate the parameters of columnar structures. Thus, these differences are derived from non-uniform columnar structures when measuring on different reflection planes.

It is necessary to understand the nucleation mechanism of the GaN growth processes in order to explain the origin of threading dislocations. For example, during the growth of GaN the epitaxial layer is normally dominated by the nucleation process, and two step nucleation techniques have been important in optimizing GaN [19,20]. To understand the growth mechanism for $Al_xGa_{1-x}N$ on AlN it is important to consider both the surface free energy which drives the growth mode and the surface diffusion which drives the nucleation rate.

In the first instance the growth mode is governed by the inequality, $\sigma_{substrate} > \sigma_{film} + \sigma_{interface}$, (where $\sigma_{substrate}$, σ_{film}, and $\sigma_{interface}$ are surface free energies of the substrate, epitaxial layer and interface respectively), which leads to wetting of the film and 2D growth, or $\sigma_{substrate} < \sigma_{film} + \sigma_{interface}$, leading to islanding and 3D growth [21-25]. It has been found that the surface free energy of AlN (0001) surface is much larger than that of the GaN (0001) surface. Compared with AlN growth, GaN films grown on AlN generally tend toward 2D growth (i.e. a wetting layer) rather than 3D growth (i.e. island formation) since Ga lowers the surface free energy of the system [22, 26-28].

Lower Al concentration / **Higher Al concentration**

: Al adatom
: Ga adatom
: N adatom

Absorption and incorporation of adatoms into the surface

Exchange of Ga adatoms with Al adatoms and diffusion of Ga adatoms on the surface

: nucleation

Reabsorption of Ga adatoms, incorporation and formation of nuclei in the surface

Nuclei movement and Island growth

Island coalescence and formation of dislocation

2D film formation

Figure 3.8 Schematic of growth mechanism in $Al_xGa_{1-x}N$ film.

50

However, when even a small amount of Al is introduced, Al adatoms are easily exchanged with some of Ga adatoms in the film due to larger Al-N bond energy (E_{AlN} = 2.88eV) than Ga-N bond energy (E_{GaN} = 2.2 eV).   The growing surface associated with Al, Ga, and N adatoms have relatively higher surface free energy and tend to induce 3D growth (i.e. islands) [21, 27-31].   Thus, the larger surface free energy of $Al_xGa_{1-x}N$ film with higher Al content should influence the 3D growth mode.

Moreover, during $Al_xGa_{1-x}N$ growth, surface diffusion could further affect the growth mode by modifying the density of nucleation sites [32]. This would occur through the exchange of Ga adatoms with Al adatoms. Ga desorption increases as Al content increases and it leads to more metal-rich condition [33, 34]. The desorbed Ga atoms can enhance diffusion lengths and surface migration and they lead to droplet formations, which in turn generates more nucleation sites.   As seen in the Figure 3.8, the growth mechanism of $Al_xGa_{1-x}N$ is influenced by both the higher surface free energy and longer Ga adatom diffusion length.   Therefore, higher Al content increases the number of nucleation sites by improving Ga adatom surface migration.   This enhances island formation by suppressing the effect of Ga adatoms on 2D growth, which results in smaller lateral coherence length of columnar structure in Figure 3.6 (a).

The edge dislocations mainly arise from formation of island coalescence (i.e. grain boundaries) [35-37]. The lateral dimension of grain (i.e. L_{ll}) decreases, as Al concentration increases, and so the edge dislocations are reduced, Figure 3.7. In other words, the island coalescence or grain mergence rate per unit area increases, which leads to more edge dislocations, as Al concentration increases. On the other hand, the screw dislocations are caused by displacement along c-direction [38]. Misfit dislocations are

generated when thickness of the film exceeds critical thickness [39]. Therefore, higher Al concentration (i.e. smaller misfit between $Al_xGa_{1-x}N$ and AlN) increases critical thickness and decreases screw dislocations density. In this work, when a comparison was completed between edge dislocations and screw dislocations, total threading dislocation was found to depend more strongly on the density of edge dislocations. In turn, the density of edge dislocations in the $Al_xGa_{1-x}N$ films primarily depended on Al concentration rather than film thickness.

3.6. Dislocation densities in InAlGaN

Indium was incorporated into AlGaN layer and effects of indium as a surfactant on dislocation density and nucleation were investigated. An $Al_xGa_{1-x}N$ (where x is 0.17) layer was grown on a sapphire (0001) substrate with an intermediate growth of low temperature AlN nucleation layer at 600 °C followed by a high temperature AlN nucleation layer at 1075 °C. In order to improve the surface morphology and the film quality, variable flow rates of trimethyl indium (TMIn) (0, 50 and 500 sccm) were introduced for the incorporation of indium at percentages of 0, 0.04, and 0.15. AFM measurements using PSIA XE100 instrument were performed after a chemical wet etch to obtain the etch-pit count.
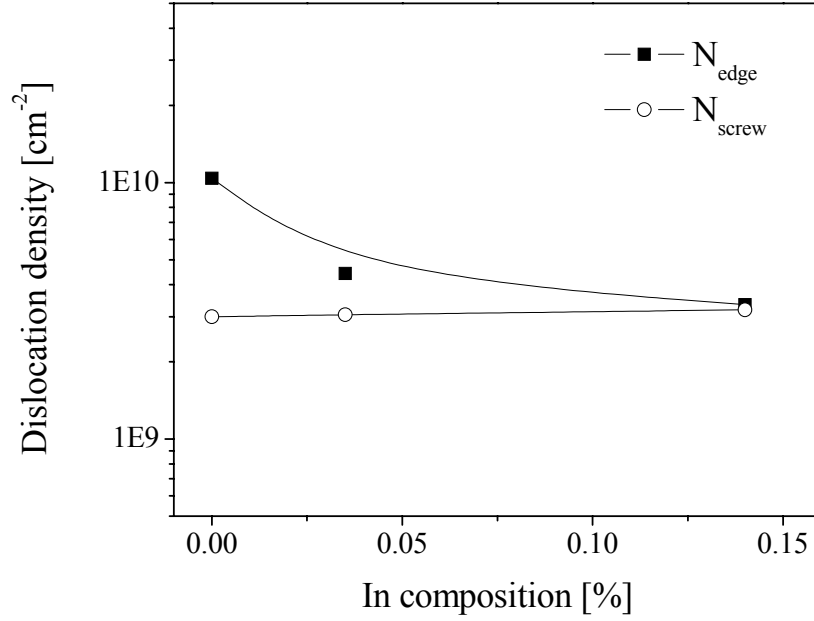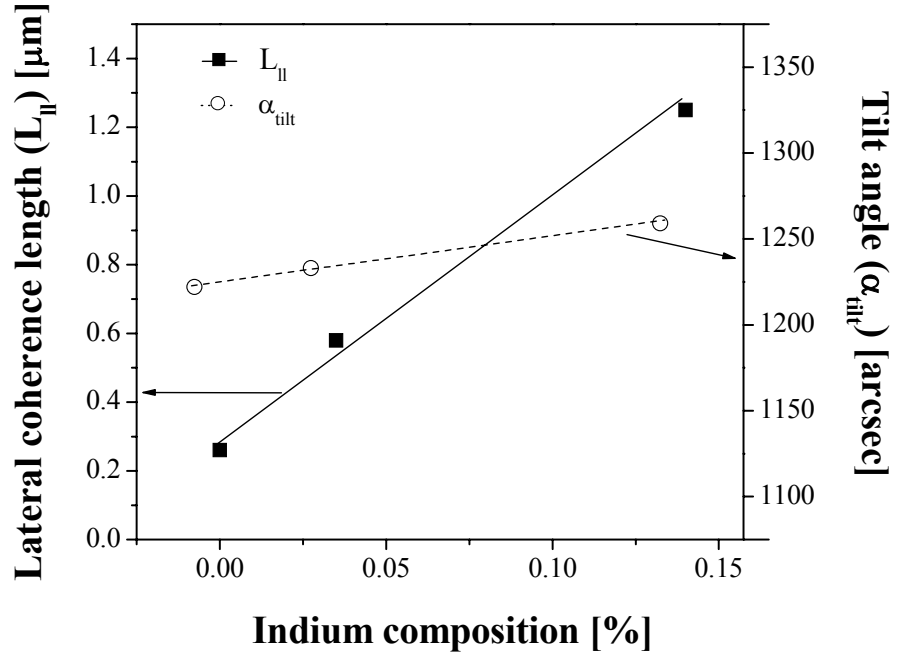
Figure 3.9 (a) Lateral coherence length and tilt angle as a function of Indium
composition (b)Variation of edge dislocation (N_{edge}) and screw dislocation
(N_{screw}) densities with In composition.

Figure 3.9 (a) indicates that the lateral coherence length and the tilt angle increase with indium composition, resulting from the WH plot, but the increase in lateral coherence length is larger than in tilt angle. This result can be explained based on the unit cell parameters of the components: GaN, AlN, and InN. InN has the largest lattice parameters (a = 3.544, c = 5.718 nm [40]) among these three nitrides. Therefore, the physical size of growing species (i.e. lateral coherence length) in the InAlGaN columnar structures increases, while the angular orientation (i.e. tilt angle) of the columnar structures is relatively less changed as indium incorporation increases. Thus, it can be stated that a small amount of indium affects the geometric size of columnar structure with a minimal effect on the strain component. Moreover, indium is incorporated as a surfactant during growth which gives rise to a decreasing the surface free energy and 2D growth, thus enhancing smoother nucleation growth with larger domain structures [28, 42].

The edge dislocations are mainly formed by island coalescence (i.e. grain boundaries), but the screw dislocations are caused by displacement along the c-direction [38]. In the Figure 3.9 (b), the screw dislocation density does not vary much with indium contents. However, the edge dislocation density is noticeably reduced with incorporation of small amounts of indium in the layer. A small amount of indium incorporation increases the physical size of the columnar structure in epilayers, which leads to less island coalescence without degrading the crystalline quality of these layers. Thus, there is an effective decrease in the total threading dislocation density which is the combination of these two dislocation densities with increased indium composition. In other words, the tilt angle and twist angle are the dominant causes of defects, while the larger lateral

coherence length affects the annihilation of dislocation density with higher indium content. However, an excess amount of indium incorporation might have influence on increasing the defects by altering growth mode.
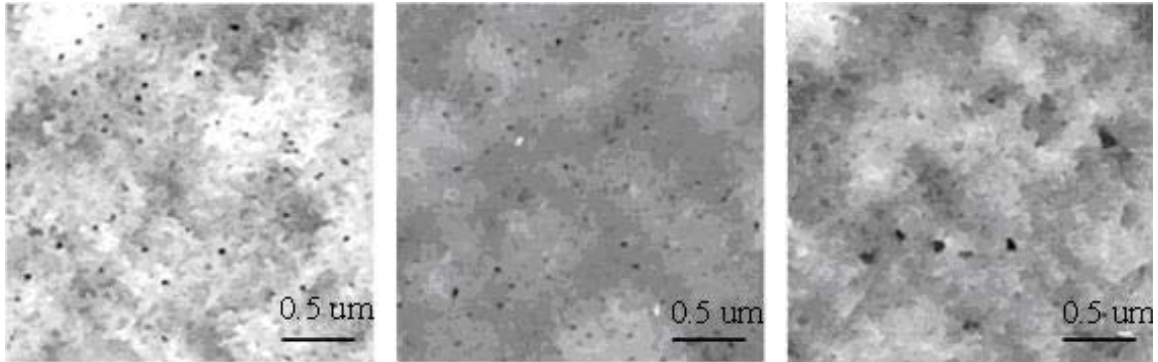
Figure 3.10 AFM images for etch-pit density after etching by H_3PO_4 (a) sample A, In = 0%, (b) sample B, In = 0.04 %, and (c) sample C, In = 0.15%.

In order to verify the effect of small amount of indium incorporation, etched pits were measured using AFM as seen in Figure 3.10. The dislocation density was estimated by counting the etched pits over a specific area. The results show that the number of etched pits is decreased, as indium is incorporated. However, in these AFM images, the black etching spots enlarged with higher indium incorporation due to the fact that indium is easily amassed around these defects.

In Figure 3.11, PL measurements revealed that a small amount of indium incorporation enhanced the emission efficiency. The PL emission intensity at room temperature was improved from 23% to 28% with higher indium incorporation. Moreover, an emission band related to intrinsic defects around 3.4eV appearing in AlGaN

epilayers apparently decreased as indium content increased. However, the energy band gap and FWHM of PL spectra showed little change with these small amounts of indium content. It has been found that screw density as well as the mixed dislocations affect PL intensity and photon lifetime [38, 42]. In this work, we could surmise that the mixed dislocations (not evaluated in this letter, but relatively proportional to pure screw dislocations) have decreased more than pure screw dislocations and played a major role for the improvement of radiative efficiency.
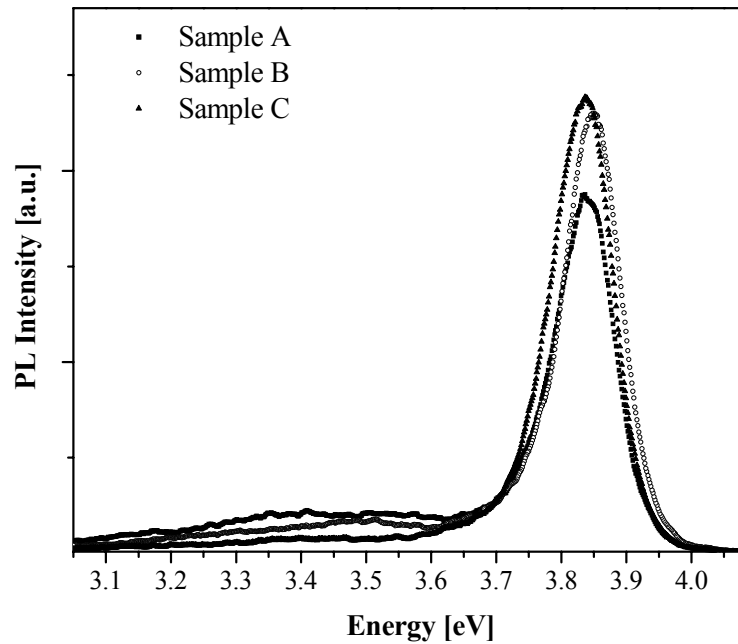
Figure 3.11 Photoluminescence spectra of sample A, B and C at room temperature.

In summary, it is found that a small amount of indium incorporation appears to improve the structural properties of the columnar growth structures in AlGaN. The results reveal the reduction of dislocation density with infinitesimal indium incorporation. This

means that integration of columnar structure with larger size can relax the dislocation density in epilayers. In other words, the local incorporation of indium enhances the annihilation of the defects in the epilayers, thereby improving the growth quality of the films. However, it should be noted that larger values of indium incorporation might increase the defect density. The values of physical parameters and the dislocation density obtained by these two methods are tabulated in Table 3.3.

Table 3.3 Summary of columnar structure factors of AlGaN with different indium content.

	Method	Sample A	Sample B	Sample C
L_{ll} [um]	W-H plot	0.26	0.58	1.25
α_{tilt} [aresec]	W-H plot	1222	1233	1259
α_{twist} [arcsec]	Φ scan	3750	3539	5592
N_{scew} [cm^{-2}]	W-H plot	3.00E+09	3.05E+09	3.19E+09
N_{edge} [cm^{-2}]	W-H plot	1.40E+10	4.42E+09	3.24E+09
TD density [cm^{-2}]	Etch Pits	2.20E+09	2.00E+09	1.70E+09

3.7. Motivation for GaN nanostructure growth

Many studies have been done to reduce the dislocation density in III-nitride materials. In-situ growth techniques have been reported, since the beginning of III-nitride

growth. A low temperature buffer layer has been commonly used [5]. However, superlattice structure as a filter layer is inserted after the buffer layer grown. The main role of this filter layer is to annihilate dislocations caused by lattice mismatch, but it is not enough to reduce dislocations.

Epitaxial lateral overgrowth [43], pendo epitaxy [44], and facet-initiated epitaxial lateral overgrowth [7] give a remarkable reduction of dislocations, but these methods need complicated fabrication processes and strict control of the growth mode. Besides, ZnO is a promising material with a lattice constant matched with GaN [45], but growing crystalline ZnO is also a challenge.

Nanostructures are too small to have dislocations and electronic energy states are spatially quantized. This results in more stable thermal perturbation and high quantum efficiency of light emitting devices. But it is also difficult to grow and control nanostructures. In this thesis, multifunctional self-organized GaN nanostructure was investigated to achieve realization of high performance devices.

3.8. References

[1] T. Metzger, R. Hopler, E. Born, and O. Ambacher, Phil. Mag., **A 77**, (1998) 1013.

[2] H. Wang, J. Zhang, C. Chen, Q. Fareed, and J. Yang, Appl. Phys. Lett., **81**, (2002) 604.

[3] M. Leszczynski, T. Suski, H. Teisseyre, P. Perlin, I. Grzegory, J. Jun, S. Porowski, T. Moustakas, J. Appl. Phys. 76 (1994) 4909.

[4] H. Heinke, V. Kirchner, S. Einfeldt, and D. Hommel, Appl. Phys. Lett. **77**, (2000) 2145.

[5] J. Weertman "Elementary Dislocation Theory", Oxford University Press, ISBN 0-19-506900-5, (1992)

[6] F. Ponce, *Microstructure of Epitaxial III-V Nitride Thin Films*, 1997

[7] H. Heinke, V. Kirchner, S. Einfeldt, and D. Hommel, Phys. Stat. Sol., **A 172**, (1999) 391.

[8] P. Fewster, "*X-Ray Scattering from semiconductors*", Imperial Press, London, (2000) 345.

[9] P. Fewster, "X-Ray and Neutron Dynamical Diffraction: Theory and Applications", NATO ASI Series B: Physics, **357,** 321 (1996).

[10] D. Bowen, "High Resolution XRD and Topography", Talyor & Francis, 67 (2001).

[11] G. Williamson and W. Hall, Acta. Metall., **1**, 22 (1953).

[12] De Keijser et al, J. Appl. Crystallogr, 16, 309 (1983).

[13] Gerald B. Stringfellow, 'Organometallic Vapor-Phase Epitaxy, Theory and Practice", Academic Press, ISBN 0-12-673842-4 (1999)

[14] V. Dmtriev, K. Irvine, A. Zubrilov, D. Tsvetkov, V. Nikolacv, M. Jakobson, D. Nelson, and A. Sitnikova, *Gallium Nitride and Related Materials*, MRS, 1996.

[15] P. Bhattacharya, Semiconductor Optoelctronic Devices, Prentice Hall, 1997.

[16] D. Woodruff, and T. Delchar, "Modern Techniques of Surface Science", Cambridge University Press, ISBN 0-521-42498-4, 1999.

[17] S. Molina, A. Sanchez, F. Pacheco, and R. Garcia, Appl. Phys. Lett. **74**, (1999) 3362.

[18] L. Kirste, D. Ebling, C. Haug, and K. Tillmann, Mater. Sci. Eng., B **82** (2001) 9.

[19] I. Akasaki, H. Amano, Y. Koide, K. Hiramatsu, and N. Sawaki, J. Crys. Growth **98**, 209 (1989).

[20] K. Hiramatsu, S. Itoch, H. Amano, I. Akasaki, N. Kuwano, T. Shiraishi, and K. Oki, J. Crys. Growth **115**, 628 (1991).

[21] M. Copel, M. Reuter, E. Kaxiras, and R. tromp, Phys. Rev. Lett., **63** 632 (1989)

[22] S. Tanaka, S. Iwai, and Y. Aoyagi, Appl. Phys. Lett., **69**, 4096 (1996)

[23] D. Eaglesham, F. Unterwald, and D. Jacobson, Phys. Rev. Lett., **70** 966 (1993)

[24] T. Shitara, J. Zhang, J. Neave, and B. Joyce, J. Appl. Phys. **71**, 4299 (1992)

[25] S. Dosanjh, X. Zhang, D. Sansom, J. Harris, M. Fahy, B. Joyce, and J. Clegg, J. Appl. Phys. **74**, 2481 (1993)

[26] N. Gognequ, D. Jalabert, E. Monroy, T. Shibata, M. Tanaka, and B. Daudin, J. Appl. Phys. **94**, 2254 (2003)

[27] E. Iliopoulos, and T. Moustakas, Appl. Phys. Lett. **81**, 295 (2002)

[28] E. Monroy, B. Daudin, E. Bellet-Amalric, N. Gogneau, D. Jalabert, F. Enjalbert, J. Brault, J. Barjon, and Le Si Dang, J. Appl. Phys. **93**, 1550 (2003)

[29] A Rosa, J. Neugebauer, J. Northrup, C. Lee and R. Feenstra, Appl. Phys. Lett. **80**, 2008 (2002)

[30] N. Grandjean and J. Massies, Phys. Rev. B 53, R13231 (1996)

[31] K. Nakajima, T. Ujihara, N. Usami, K. Fujiwara, G. Sazake, and T. Shishido, J. Crys. Growth, **170**, 329 (1997)

[32] J. Salik J. Appl. Phys., **57**, 5017 (1985)

[33] E. Iliopoulos, K. Ludwis, T. Moustakas, P. Komninous, T. Karakostas, G. Nouet, and S. Chu, Mater. Sci. Eng., B **87**, 227 (2001)

[34] J. Jenny, J. Van Nostrand and R. Daspi, Appl. Phys. Lett. **72**, 85 (1998).

[35] T. Bottcher, S. Einfeldt, S. Figge, R. Chierchia, H. Heinke, and D. Hommel, and J. Speck, Appl. Phys. Lett. **78**, 1976 (2001)

[36] S. Tanaka, S. Iwai, and Y. Aoyagi, J. Crys. Growth, **170**, 329 (1997)

[37] W. Wu, D. Kapolnek, S. Keller, Y. Li, B. Keller, S. DenBaars, and J. Speck, Appl. Phys. Lett. **68**, 643 (1996).

[38] J. Northrup, Appl. Phys. Lett. **78**, 2288 (2001)

[39] R. People and J. Bean Appl. Phys., **47**, 322 (1985)

[40] K. Osamura, S. Naka and Y. Murakami, J. Appl. Phys., **46**, 3432 (1975)

[41] J. Neugebauer, Phys. Stat. Sol. (c) **0**. No. 6. 16551 (2003)

[42] T. Hino, S. Tomiya, T. Miyajima, K. Yanashima, S. Hashimoto, and M. Ikeda, Appl. Phys. Lett. **76**, 3421 (2000).

[43] X. Zhang, P.Dapkus, D. Rich, I. Kim, J. Kobayashi, N. Kobayashi, J. Electr. Mat. 29 (2000) 10.

[44] T. Geherk, K. Linthicum, D. Thomoson, P. Rajagopal, A. Batcheiro, and R. Davis, MRS Internet J. Nitride Semicond. Res. 4S1 (1999) G3.2

[45] U. Ozgur,a_ Ya. I. Alivov, C. Liu, A. Teke,b_ M. A. Reshchikov, S. Doðan,c_ V. Avrutin, S.-J. Cho, and H. Morkoçd_ J. Appl. Phys., 98, (2005) 041301.

.

CHAPTER 4

SELF-ASSEMBLED GaN NANOSTRUCTURES ON AlN

4.1. Fundamental theories of quantum dots

4.1.1 Introduction

Quantum dot is so small that it behaves like a particle in a nano-scale cage and electronic carriers in the particle affect its properties. It has been revealed that the quantum dots have unique characteristics such as (1) quantum-dot *shape* dependent transitions, (2) size-dependent (red) shifts between absorption and emission, (3) emission from high excited levels, (4) surface-mediated transitions, (5) exchange splitting, (6) strain-induced splitting, and (7) Coulomb-blockade transitions [1-3].
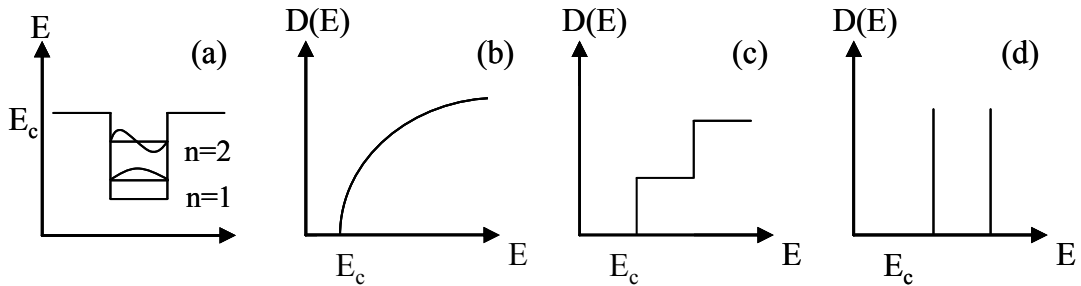
Figure 4.1 (a) quantized electronic states, and density of electronic states in (b) bulk materials, (c) quantum well, and (d) quantum dot.

The electronic energy level of quantum dot is discrete energy states of quantized electronics and is spatially localized as Figure 4.1 (d) shows the density of electronic state in quantum dot [4].

4.1.2. Physical properties

Compared to higher-order dimension structures, quantum dot is the prototype of zero dimensional system and possesses many unique properties. The electronic states in a quantum dot are spatially localized and the energy is fully quantized, similar to a single atom or atomic system. Thus, quantum dot is a highly stable system against any thermal perturbation. In addition, due to quantization, the electron density of states near the band gap is higher than 2D and 3D systems, leading to a higher probability of optical transition. Electron localization may dramatically reduce the scattering of electrons by bulk defects and reduce the rate of non-radiative recombination. These properties are directly relevant to the high thermal stability and high quantum efficiency in light emitting and detecting devices and are of great importance in terms of device application [5-7].

4.1.3. Growth Mechanisms

Many lithography and processing technologies have been developed, but they cannot still make less than 10 nm scale structures yet. Another approach which we have been aiming at is self-organization of nanostructures on the surface. In the self-organized nanostructure growth, it is necessary to understand thermodynamic and kinetic issues, because the growth mechanism results from mutual effects between kinetic energy of adatoms and surface free energies of substrate, film and interface [8].

Surface free energy is a term of dangling energy of atoms on the substrate ($\sigma_{substrate}$), film (σ_{film}), and film-substrate interfacial interaction ($\sigma_{interface}$) [9]. Atoms at free surfaces are more energetic than atoms within the underlying bulk. The difference in interatomic energy of atoms at these tow sites is brought out by surface free energy. The surface free energy mainly plays a role in nucleation which should influence nanostructure growth. Thus, the surface free energy is an important factor to determine the dimension, density or rate of nucleus [10-12].

There are basic three different growth modes: Frank-Van Der Merwe (FM), Volmer-Weber (VW), and Stranski-Krastanow (SK) as shown in Figure 4.2.
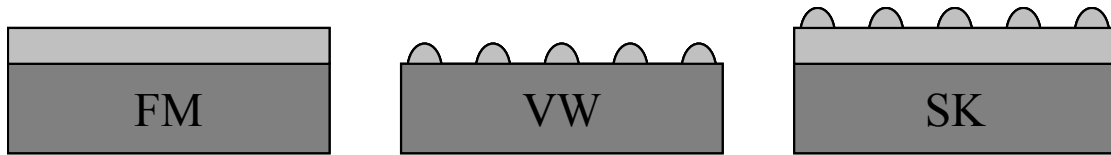
Figure 4.2 Schematic structures of the three growth mechanisms; (a) FM, (b) VW, and (c) SK.

(a) Frank-Van Der Merwe mode

In the case of $\sigma_{substrate} > \sigma_{film} + \sigma_{interface}$, the growing species reduce the surface free energy and wet the substrate to form a monolayer (or 2D layer). Then the growing species deposit on the first monolayer and form a second monolayer, which is also called layer-by-layer growth [13, 14].

(b) Volmer-Weber (VW) mode

As the term of $\sigma_{film} + \sigma_{interface}$ increases, the growth mode transits from the FM to the VW growth mode. Initial growing species aggregate as small 3D islands, which increase in size as further deposition continues until they touch and coalescence to form a continuous film. Such nucleation occurs when the binding energy of adatoms to each other is stronger than their binding energy to the substrate [15, 16].

(c) Stranski-Krastanow (SK) mode

For a strained epilayer with small interface energy, initial growth may occur layer by layer, but a thicker layer has larger strain energy and can lower its energy by forming isolated islands in which strain is relaxed. Thus the SK mode is the combination mode of FM and VW modes [17-19].

In addition, Owtwal ripening process is a thermal activation process utilized to form nanostructures after deposition of a few 2D monolayers [20]. When a temperature ramp is immediately applied under a nitrogen atmosphere, these 2D layers are transformed to 3D growth mode by the thermal activation. If the coherent 3D nanostructures (i.e. islands) are larger, they have larger contact area with the substrate and so dislocations occur during ripening islands at some point. Therefore, in the nanostructure growth, it is important to control growing islands by the thermal activation until they reach the critical size value [21-23].
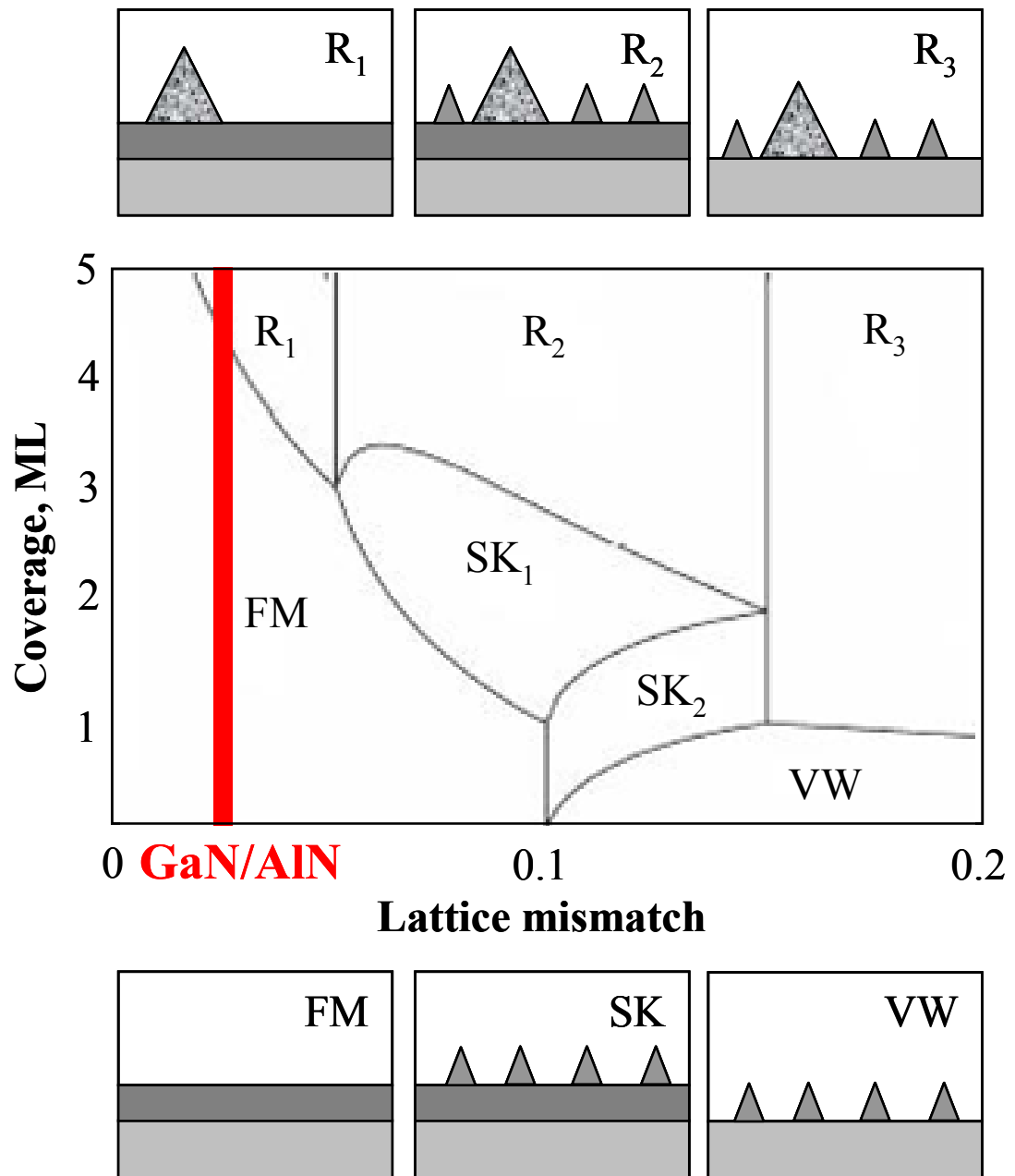
Figure 4.3 Equilibrium phase diagram as a function of coverage and lattice misfit. GaN/AlN has 2.5% lattice misfit.

Figure 4.3 shows an equilibrium phase diagram of growth modes as a function of coverage and lattice mismatch. Six small panels on the top and bottom of this figure illustrate surface morphology in six different growth modes. Small islands indicate the presence of stable islands, while larger islands indicate ripening islands. However, GaN / AlN system has 2.5% lattice mismatch that is too small to reach 3D growth. But MOCVD system possible changes the growth modes using some growth techniques and these techniques will be described in this section.

4.1.4. Current state of the art for GaN nanostructures

The introduction of quantum wells (QWs) in the early 1970s was a turning point in the direction of research on electronic structures [24]. A QW is a very thin layer sandwiched between two layers with wider energy gaps. In the 1980s, research interests of shifted toward lower dimensional structures: 1D confinement (quantum wires) [25] and 0D confinement (quantum dots). Since investigation of InAs QDs grown on GaAs revealed the 2D to 3D transition in the SK mode and strong dependence of growth parameters on InAs QD growth[8, 14], this technique has been applied to other materials [i.e. Ge / Si, , (Ga,In,Al)P, (Zn,Cd,Mg) / (S,Se), (In,Ga)N / (Al,Ga)N].

Self-organized GaN nanostructures were commonly grown with relatively low temperatures around 700 ºC using MBE. Widmann et. al. first activated GaN nanostructures on AlN optically, and reported that the optical properties of GaN nanostructures are caused by a trade-off between confinement (resulting in blue-shift) and piezoelectric (resulting in red-shift) effects [26-28].
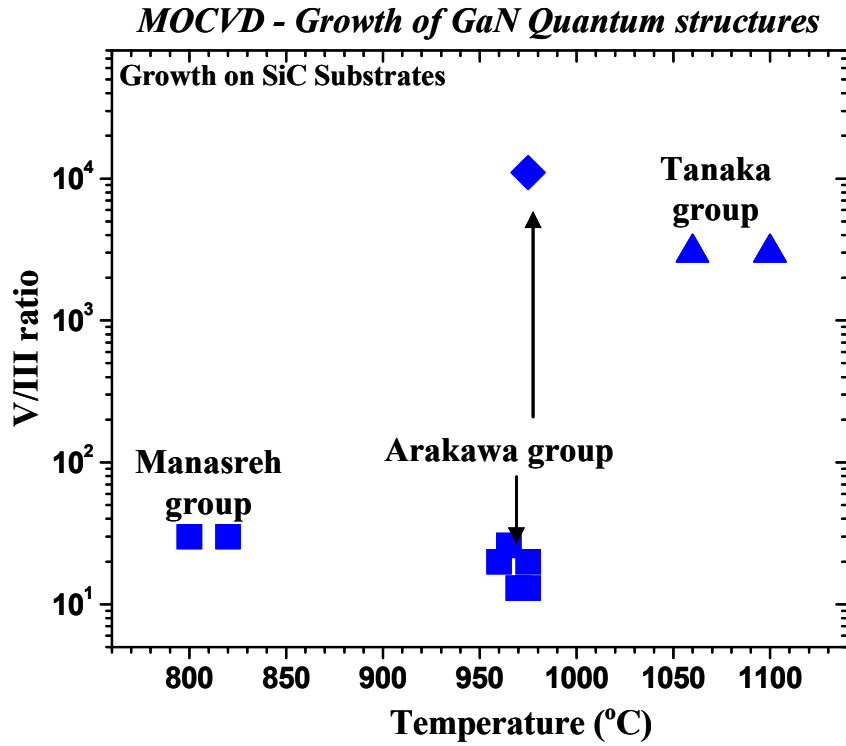
Figure 4.4 A graph of other research in GaN nanostructure using MOCVD.

Figure 4.4 shows that MOCVD-grown GaN nanostructures have also been investigated since the mid-1990's. Dmitrev *et. al.* grew GaN QDs directly on 6H-SiC substrates instead of sapphire [29]. In this case, the lattice mismatch between the GaN and SiC is large enough to lead to island growth. Other approach using sapphire substrate has been studied by Tanaka and Han [30, 31], who succeeded in growth of GaN quantum dots on AlGaN template layer. They employed Si as an anti-surfactant and droplet epitaxy growth technique for their quantum dots, respectively. GaN nanostructure/AlN growth on a sapphire substrate using MOCVD was first performed in this work.

4.2. AlN growth as a GaN nanostructure template

4.2.1 Introduction

Recently, III-nitride compound alloys have been attractive for optoelectronic applications due to their direct band gap energies from UV to infra regions. However, few studies on AlN growth have been reported, although AlN is a promising material in view of wide band gap, high thermal conductivity and negative electron affinity. The major purposes for AlN have been as a buffer layer for III-nitride-based devices, i.e. the use of buffer layer for GaN growth on SiC substrate [32,33], and utilized for electronic packaging applications due to caustic chemicals combined with a reasonable thermal match to Si and GaAs [34]. In addition, piezoelectric property of AlN makes an attractive for surface acoustic wave device application.

AlN has hardness, high thermal conductivity, resistance at high temperatures. AlN is a very hard material with a melting point in excess of 2800 °C and it also has a good thermal conductivity of 2 W/cmK [35], which can be used for a material to emit heat energy from devices. Its structure is wurtzite type with lattice constants, a-spacing = 3.112 Å and c-spacing = 4.982 Å [36]. AlN single crystal is an insulator because of the low intrinsic carrier concentration and deep native defect and impurity energy levels of AlN, so it has been found that it is hard to achieve p-type and even n-type AlN films, which is a big barrier to develop semiconductor devices. In optical property, AlN has a direct band gap energy of 6.2 eV at room temperature.
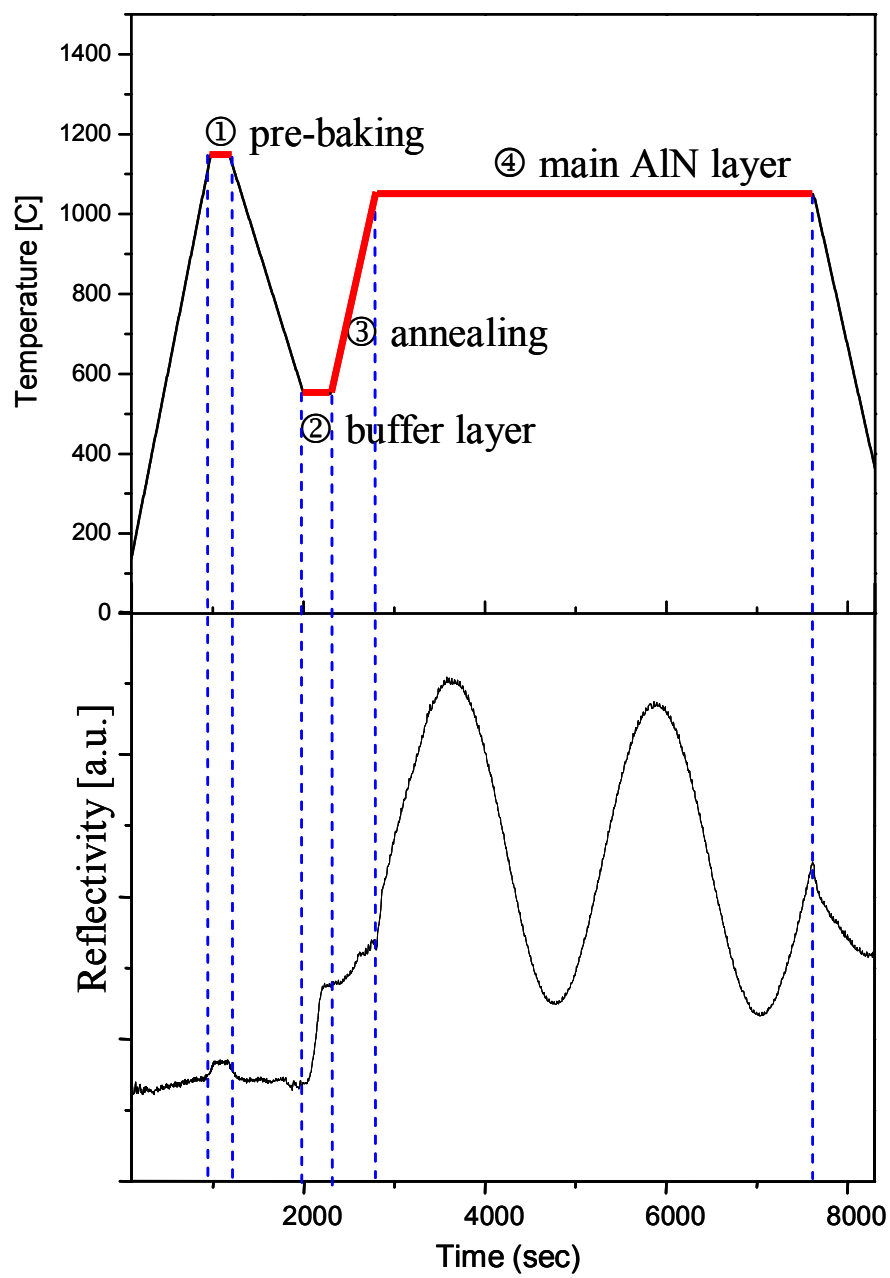
Figure 4.5 (a) a schematic of growth steps with varying growth temperature and (b) in-situ characterization data for 0.3μm-thick AlN growth

4.2.2 General growth techniques

AlN growth is not easy to achieve due to high reactivity of Al. High growth temperature, high purity source materials, and oxygen-free ambient are required for high crystalline quality. We have used a two-step growth technique in which the thin first layer was grown at a low temperature to prevent thermal damage of substrate surface, and then the second layer was grown at a high temperature to obtain high quality AlN.

Figure 4.5 shows growth process and in-situ data during AlN growth. All of AlN growths were performed on sapphire substrates. The first growth process in AlN is pre-baking step at 1100 ºC under H_2 ambient to clean the substrate surface and to recrystallize the substrate. After the pre-baking, growth temperature decreases to 550 ºC, and then TMAl and ammonia sources are introduced into the growth chamber. This relatively low temperature AlN growth as a buffer layer is performed for a couple of minutes. A primary purpose of this step is to relieve the lattice mismatch between a main AlN and the sapphire substrate and to provide seeds where AlN is grown [37]. But a thick crystalline AlN film as the buffer layer would not have this benefit anymore, thus thickness of the low temperature (LT) AlN is a crucial factor to affect the main AlN film. Moreover, GaN and AlGaN layers are also used on some of samples to compare effects of buffer layers.

After LT AlN growth, the growth temperature increases above 1000 ºC for thermal activation of LT AlN film under ammonia background. This process provides recrystallization of LT AlN and nucleation. Figure 4.5 shows that *in-situ* signal would not fall down during the third step since LT AlN had been grown. It is found that adjacent AlN islands do not coalesce each other or grow laterally but the islands get larger with

3D-growth formation because it is hard of AlN adatoms to migrate on the surface and to get smoother. However, the following high temperature AlN film is grown at above 1050 ºC. Growth temperature, pressure, and V/III ratio affect AlN crystal quality and its surface morphology.
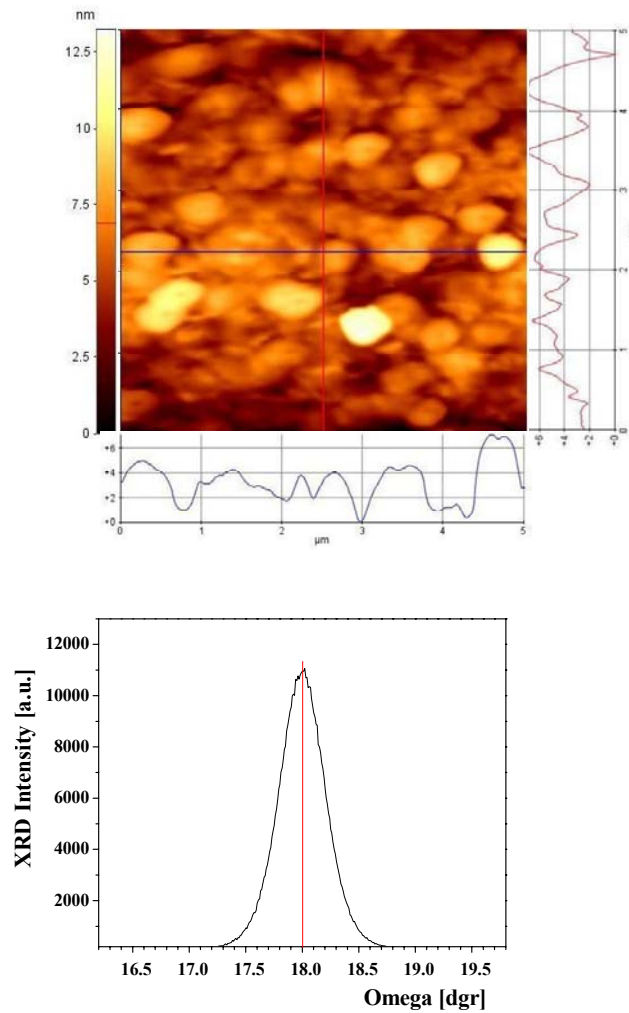
Figure 4.6 (a) AFM image and (b) XRD data on AlN.

4.2.3 *Ex-situ* characterizations

Ex-situ characterizations were performed to optimize growth conditions using not only AFM for surface morphology and surface roughness but also high resolution XRD for crystalline quality. Figure 4.6 (a) shows that the surface morphology of AlN reveals micro-sized island growth (i.e. 3D growth) which causes the surface rough rather than a general step-flow in MOCVD. RSM (Root Square Mean) value of surface roughness is more than 2 nm. However, a rocking curve scan was performed on (0 0 0 2) plane of AlN epitaxial layer using the high resolution XRD as shown in Figure 4.6 (b). We have over 1000 arcseconds of FWHM to determine relative crystal quality, which is pretty larger than GaN's FWHM, generally between 100 and 200 arecseconds. From these two characterizations, it was found that our AlN films have bad quality in comparing with GaN films. Pre-reactions of AlN prior to film deposition and slower adatom migration on the substrate are major barriers to obtain high quality AlN layer. In the next subchapter, optimization of growth conditions and their characterizations will be described.

4.2.4 Optimized growth conditions for smoother surface

In this work, AlN grown on sapphire has been utilized. AlN has a large lattice mismatch with GaN, which encourages nanostructure growth, but the roughness of AlN template may typically discourage the nanostructure growth. It has been shown that columnar structures of the AlN templates are formed and voids may be generated during coalescence of these columnar structures in Figure 4.6 (a). These voids prevent adatoms

from migrating on the surface due to vacancy occupation. Therefore, a smoother AlN template is required.

In order to obtain high quality AlN template layers, a two-step growth process was employed in which a LT AlN buffer layer was grown at 550 °C followed by a HT AlN layer grown at above 1050°C. Growth parameters such as growth temperature, pressure, and V/III ratio were altered to optimize. In addition effects of thickness of LT AlN buffer layer on surface morphology were investigated.

The growth temperature for AlN is usually higher than other III-nitride material growth, because AlN has a higher reactive energy. The temperature is set between 1000 °C and 1200 °C in MOCVD growth. In this work, effects of growth temperature up to 1150 °C (which is the tool limit) on surface morphology were investigated. Figure 4.7 shows AFM images and *in-situ* optical characterization measurements with different growth temperatures. At lower growth temperatures, kinetic and thermodynamic energies are not sufficient to coalesce AlN islands (i.e. grains) and crystallize. On the other hand, at excessively higher temperatures, these energies are so strong to leads vertical growth, rather than island coalescence and lateral growth. However, we have optimized the growth temperature at 1100 °C. In comparing the *in-situ* reflectivity signals of the optimized temperature [Figure 4.7 (b)] with lower or higher temperature [Figure 4.7 (a) or (c)], the oscillation signals are falling down, indicating that AlN layers get rougher. This results was confirmed by AFM characterizations. AFM reveals that RSM surface roughness on AlN layer grown at the optimized temperature is 6 Å which is 2 ~ 10 times lower than other temperatures as seen in Figure 4.7.
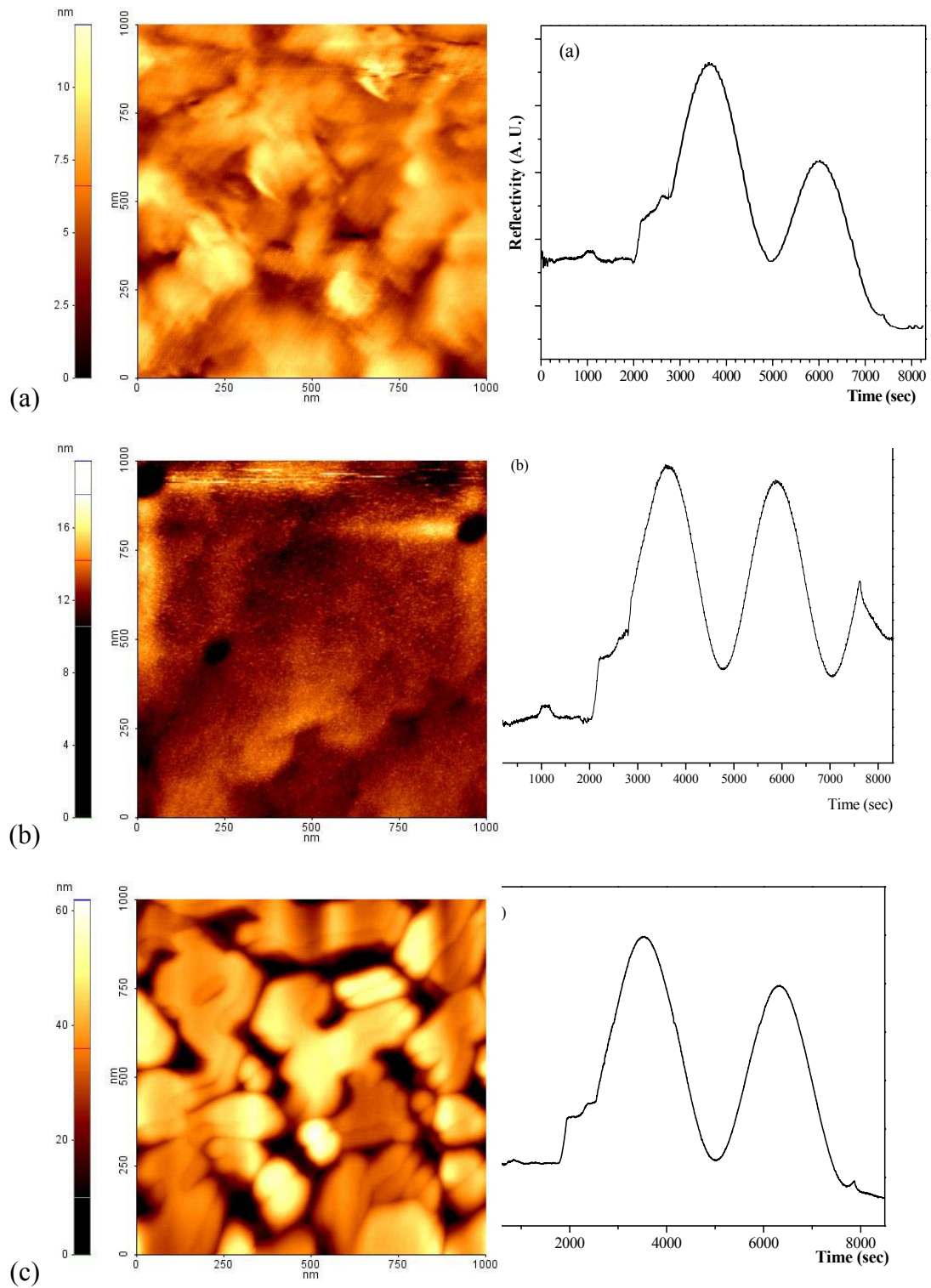
Figure 4.7 Surface morphologies and *in-situ* reflectivity measurements of AlN layers with different temperatures, (a) 1050, (b) 1100 and (c) 1150 °C.

In AlN growth, growth pressure is an important factor to influence growth rate. We had changed the pressure in the ranges from 30 to 200 Torr. In higher pressures above 100 Torr, the growth rate abruptly decreased to less 0.1 μm/hour, but the growth rate increased as the pressure decreased from 100 Torr. The growth rate of AlN is tremendously affected by parasitic reaction [38, 39]. The AlN particles are generated by the reactions

$$2Al\,(CH_3)_2 \cdot NH_2 \quad \rightarrow \quad AlN \text{ particles or } [Al\,(CH_3)_2 \cdot NH_2]_2 \quad (4.1)$$

$$[Al\,(CH_3)_2 \cdot NH_2]_3 \quad \rightarrow \quad AlN \text{ particles} \quad\quad\quad\quad (4.2)$$
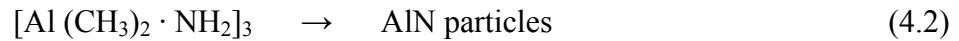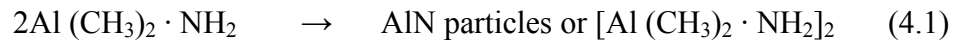
These particles are taken away from the boundary area of the substrate, which does not lead to deposition. The dimers, $[Al\,(CH_3)_2 \cdot NH_2]_2$, have enough energy to be decomposed into methyl radicals for AlN particle generation at high temperatures. Moreover, trimers $[Al\,(CH_3)_2 \cdot NH_2]_2]$ and higher n-mers ($[Al\,(CH_3)_2 \cdot NH_2]_n$ for n>3) are easily reacted to be AlN particles which tends to deposit on the chamber wall or to be exhausted to outlet. Therefore, there is higher possibility to react between organometallic species, (i.e. TMAl) and ammonia and to produce dimmer, trimers, and higher n-mers for AlN particles as the pressure increases, which reduces the growth rate. However, in low pressures, surface kinetics mainly affects AlN deposition, and the gas phase parasitic reaction is weakened.

Effects of the parasitic reactions on surface morphology were also investigated. Weaker parasitic reaction in lower pressures contributes to improve surface morphology, but mass transport is too dominant for source spices to (chemi or physi)-absorb onto the substrate in the pressure below 50 Torr, and the surface roughness is degraded due to non-lateral growth. Thus, we have found that the optimized growth pressure is 50 Torr.
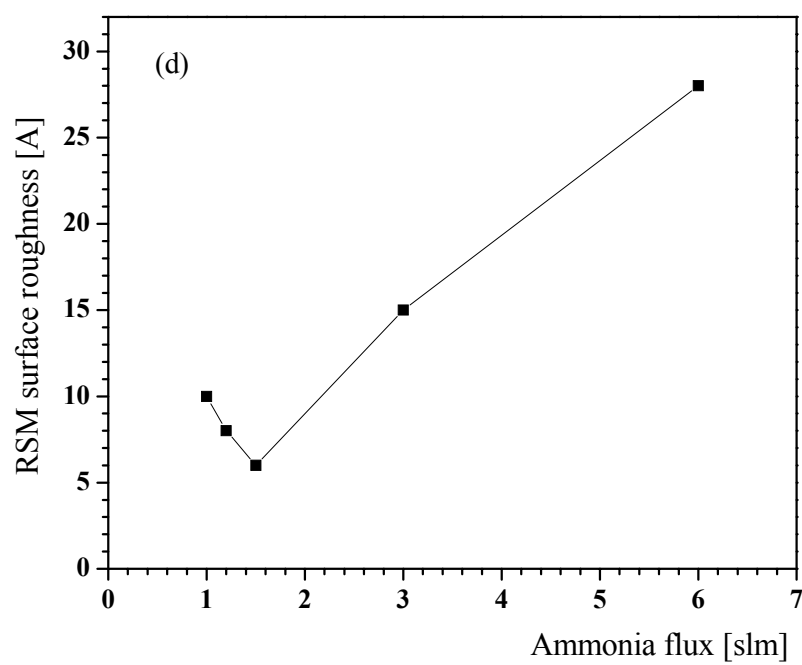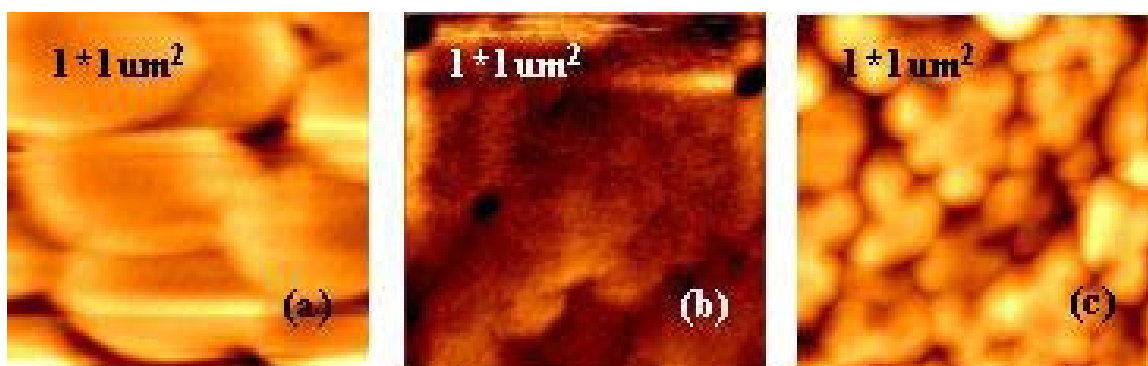
Figure 4.8 AFM images with ammonia flux (a) 3 slm, (b) 1.5 slm, and (c) 1 slm.
(d) A graph of surface roughness as a function of ammonia flux.

We changed V/III ratio with different NH_3 flow rates. We had ammonia fluxes, 6 slm, 3 slm, 1.5 slm, 1.2 slm and 1 slm. Figure 4.8 shows surface morphologies of AFM images and a graph of surface roughness from AFM measurements. With the decrease of the ammonia flow rate, the surface roughness is improved, and below 1.5 slm, the surface morphology gets degraded as seen in Figure 4.8 (d). It is found that ammonia can lower the potential energy barriers to form trimers and higher n-mers, which leads to rougher surface as well as reduction of growth rate [40]

It has been reported that a buffer layer remarkably affects main epitaxial layer [41,42]. In this subchapter, we have studied the surface morphology of HT AlN depending on thickness of LT AlN as a buffer layer. The buffer layer plays a role to relieve lattice mismatch from substrate and provide seeds at which a desired film starts growing. LT AlN layer was optimized by changing its thickness from 10 to 30 nm. *In-situ* reflectivity measurements in Figure 4.8 show reflective curves of LT AlN buffer and HT-AlN layers with time. Oscillations of HT AlN reflectivity signals in Figure 4.9 (a) and (c) get more dramatically falling down as the growth time elapses than in Figure 4.9 (b). It is found that the reflective signal into the detector gets weaker because HT AlN layers in Figure 4.9 (a) and (c) get rougher and incident optical beams get deflective on the surface of these layers. When LT AlN buffer layer is too thin, the buffer layer can not relieve lattice mismatch of the substrate, resulting in non-crystallization of HT AlN layer on the substrate and even generation high dislocation density in HT AlN [43]. In our study, the optimized thickness of LT AlN buffer layer is 20 nm and RMS surface roughness from AFM scans have a good agreement with this trend.
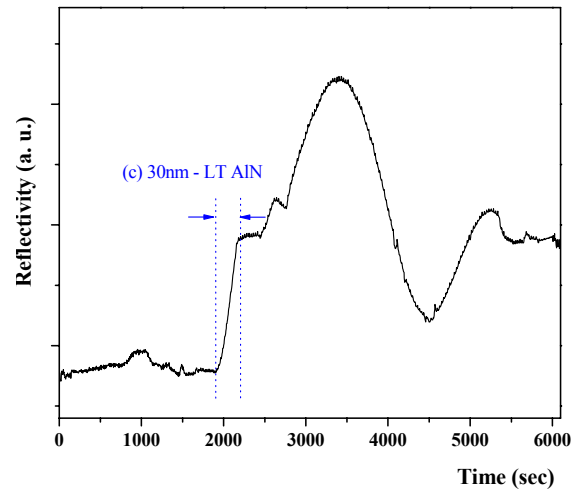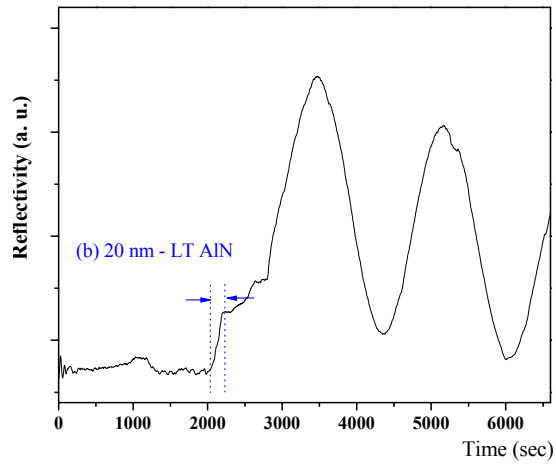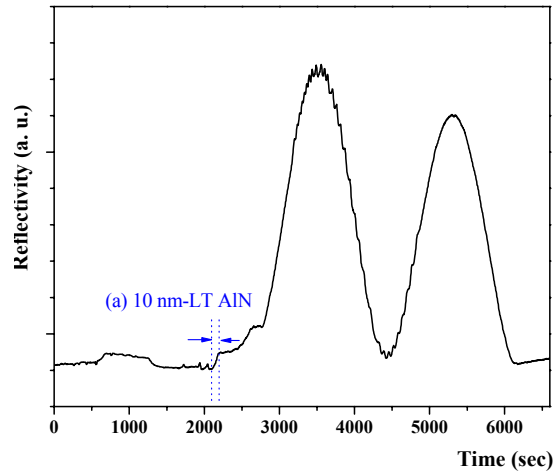
Figure 4.9 *In-situ* reflectivity measurements of AlN layers with different thickness of the buffer layer (a) 10, (b) 20 and (c) 30 nm.

Various growth conditions for AlN template of GaN nanostructures have been optimized, and the surface roughness of the AlN template is less than 10 Å which is good enough to growth GaN nanostructures. The dislocations from AlN template do not significantly affect GaN islands.

4.3 Nucleation and formation of GaN nanostructures

(a) lattice-mismatched system

(b) Mostly governed by pseudomorphic growth

(c) Larger strain energy

(d) Formation of islands to release this strain energy
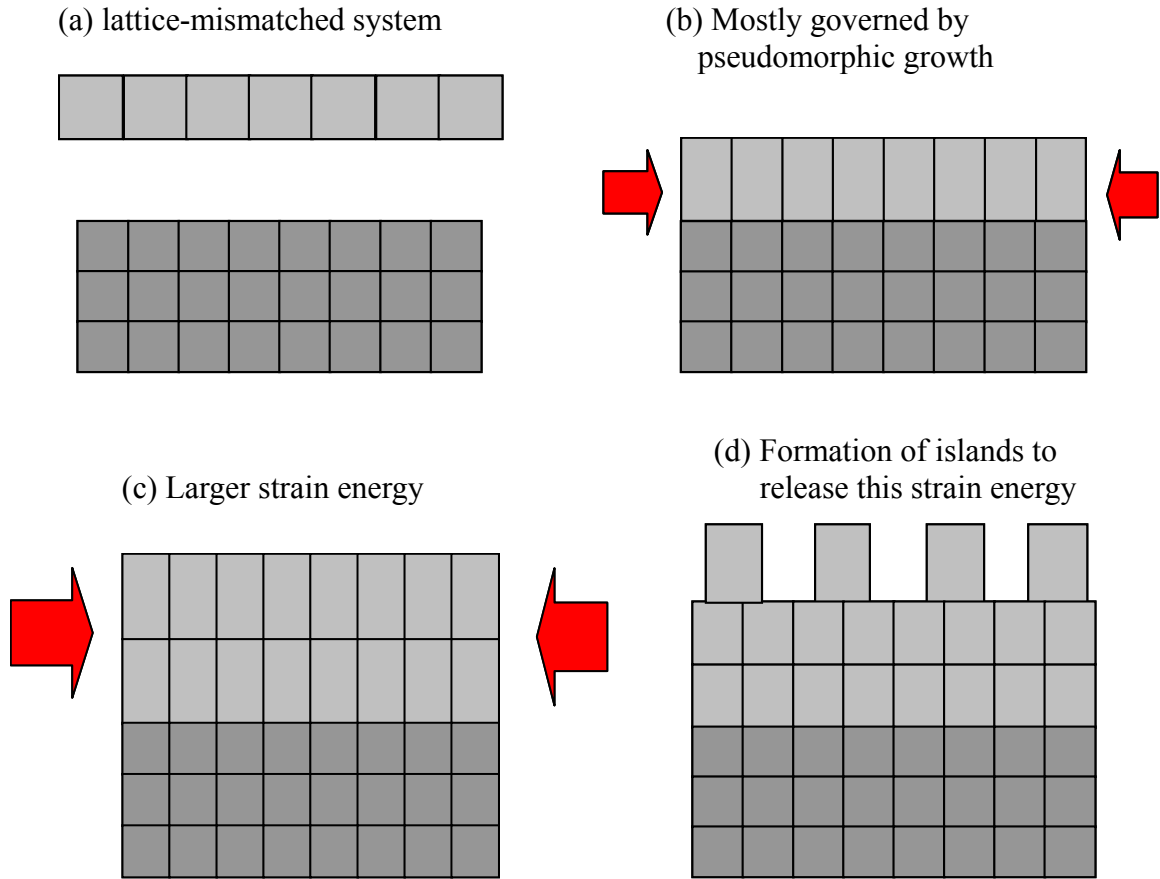
Figure 4.10 Growth mechanism steps of GaN nanostructure on AlN structure.

The achievement of self-organized GaN nanostructures using S-K like mode in MOCVD growth is shown in this section. The MOCVD provided a remarkable control ability to form nanostructures. The growth techniques which are given through general GaN growths were based on the self-organized nanostructures.

Figure 4.10 shows the growth process steps of GaN nanostructure on AlN If a crystalline material is grown on another crystalline material with smaller lattice constant, the growing material have a compressive strain make it squeezed. If the growth continues further, total strain energy in the growing material increases. At certain point, islands start forming to release the strain energy as seen in Figure 4. 10. (d).

Step 1;

Nucleation and formation of nanostructure

GaN   GaN   GaN

AlN layer

Step 2; Nanostructure overgrowth

GaN   GaN   GaN

AlN layer
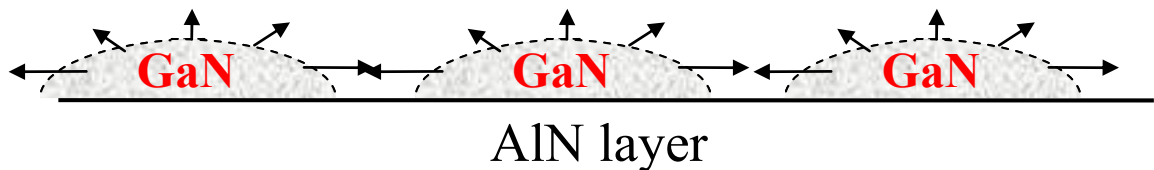
Figure 4.11 Two steps for 3D growth process.

Two steps for the 3D growth mode have divided to control stability and island density as seen in Figure 4. 11. The initial nucleation where islands start forming occurs during the first step. Islands grow and overgrow even laterally, and these islands become finally 2D layer after the second step as known for the ripening effect. Growth to form islands needs to be stop in the middle of the second step. But the transition from the first step to the second step is so fast and is not easy to control. Therefore, control of this transition is very important to form nanostructures. In this section, this transition is under control with low V/III ratios and low growth temperature.
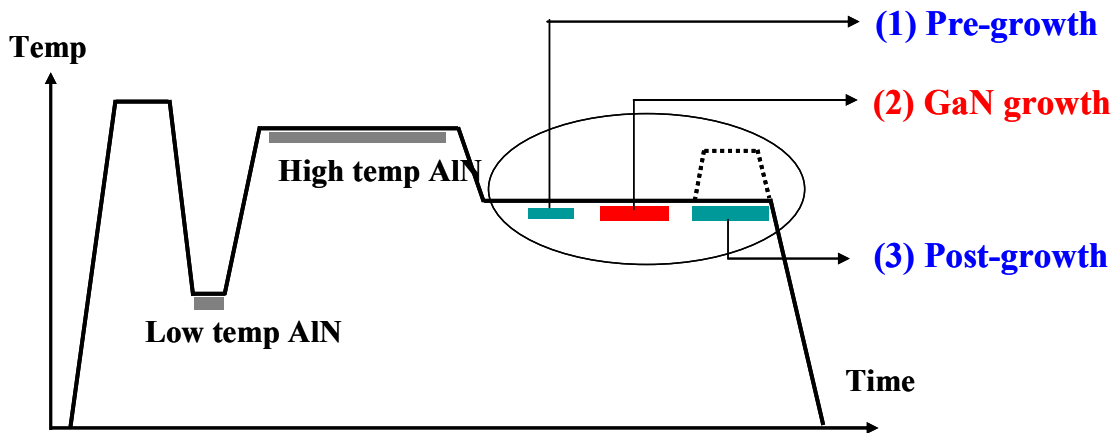
Figure 4.12 Growth process step of GaN nanostructure on AlN as a function of temperature variation with time.

Figure 4.12 shows temperature variation with time. Firstly the temperature was increased to clean the sapphire surface, An AlN buffer layer on the sapphire wafer was grown at relatively low temperature, and the high crystalline quality AlN was grown at high temperature. Then, GaN nanostructure could been grown on this top of AlN.

Three different process areas for GaN nanostructure were studied as seen in the circle. In the first step, pre-growth treatment, antisurfactant which can change surface free energy was considered. In the actual GaN growth step, various growth parameters like growth temperature, V/III source ratio, TMGa flow were investigated. Lastly, thermal treatment was considered with the ripening effect in post-growth step.

Table 4.1 Growth process and its effect.

Process	Effect
Pre-growth	Changing surface free energy : Anti-surfactant
GaN growth	Growth parameters : Growth temperature, V/III source ratio, source flow, etc.
Post-growth	Ripening effect : Thermal treatment

4.4 Pre-growth treatment

Before optimization of growth conditions, silane was introduced as an anti-surfactant to increase available nucleation sites before GaN deposition [44, 45]. As the formation of nanostructures was supported by such a gallium bilayer [44], introduction of Si leads to Si-N bonding and sub-monolayer coverage changes the surface energy, forming the 3D growth of GaN on AlN as seen in Figure 4.13 (a).
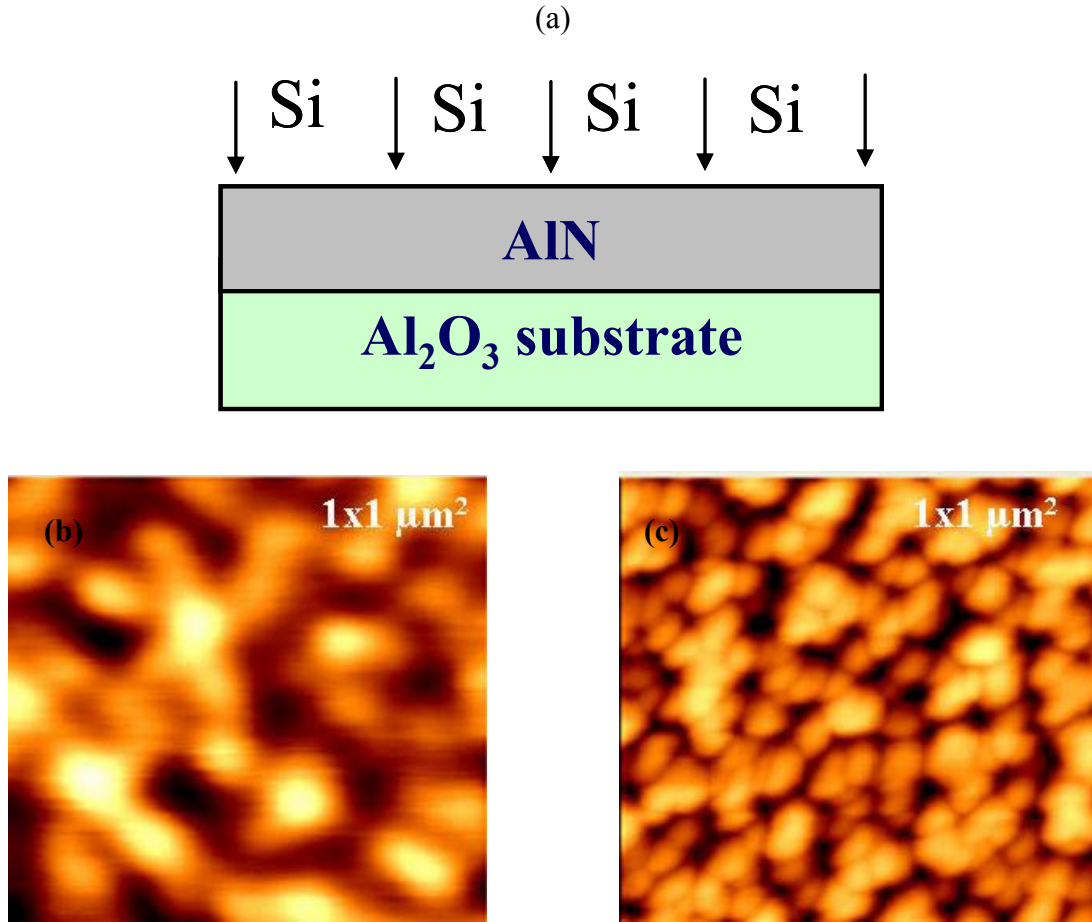
Figure 4.13 (a) A schematic of silicon incorporation in the pre-growth, and AFM images of GaN nanostructures on AlN (b) without Si or (c) with Si as anti-surfactant.

AFM images in Figure 4.13 (b) and (c) show that island densities up to 10^{10} cm^{-2} were achieved using Si, and the use of an anti-surfactant made it possible to form nanostructures with significantly smaller dimensions. The conditions of Si deposition were optimized under 5 μmoles of silane for 5 seconds. However, the sizes of nanostructures were still big, but their size could be shrunken through optimization of growth conditions later.
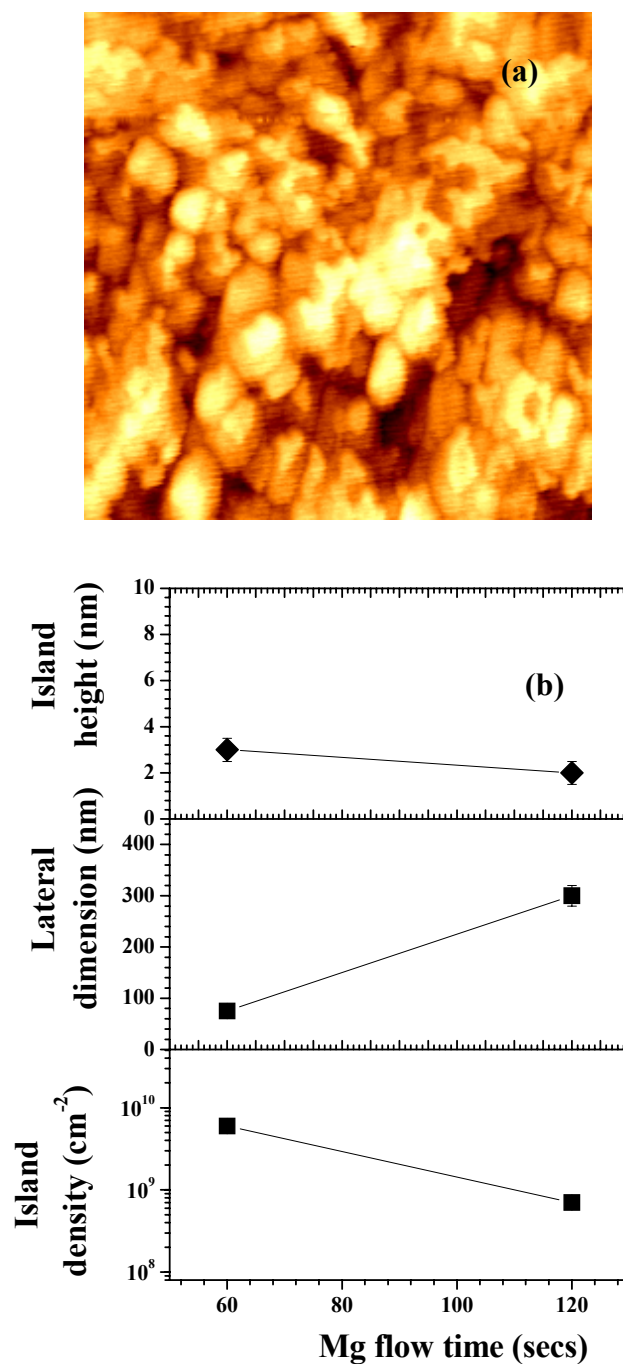
Figure 4.14 (a) AFM image of surface morphology for GaN nanostructures prior to Mg
introduced and (b) geometric GaN nanostructures as a function of the Mg
deposition time.

Magnesium is a p type dopant of the most common materials for III-nitride semiconductors. However, Mg has been known that it degrades surface morphology but changes surface free energy, so we used its characteristic.

The magnesium was introduced before GaN nanostructures were formed. The growth conditions for GaN nanostructures were fixed and we only changed Cp_2Mg flow rate as a MO precursor. Cp_2Mg 500 sccm was flowed for 1 min. Figure 4.14 shows surface morphology of GaN nanostructures after the flow was optimized. Island size is dramatically decreased, and island density increased. The nanostructure rough surface can be utilized on top of a p-type layer for higher EQE.

4.5 GaN growth step

4.5.1 Growth temperature

In order to achieve self-organized GaN nanostructures, we firstly investigated the growth temperature because the growth temperature is an important parameter to govern the growth mechanism as seen Chapter 2.2.4. We investigated the effect of growth mechanism on S-K mode with different growth temperatures. Thus, we changed the temperatures with a wide range.
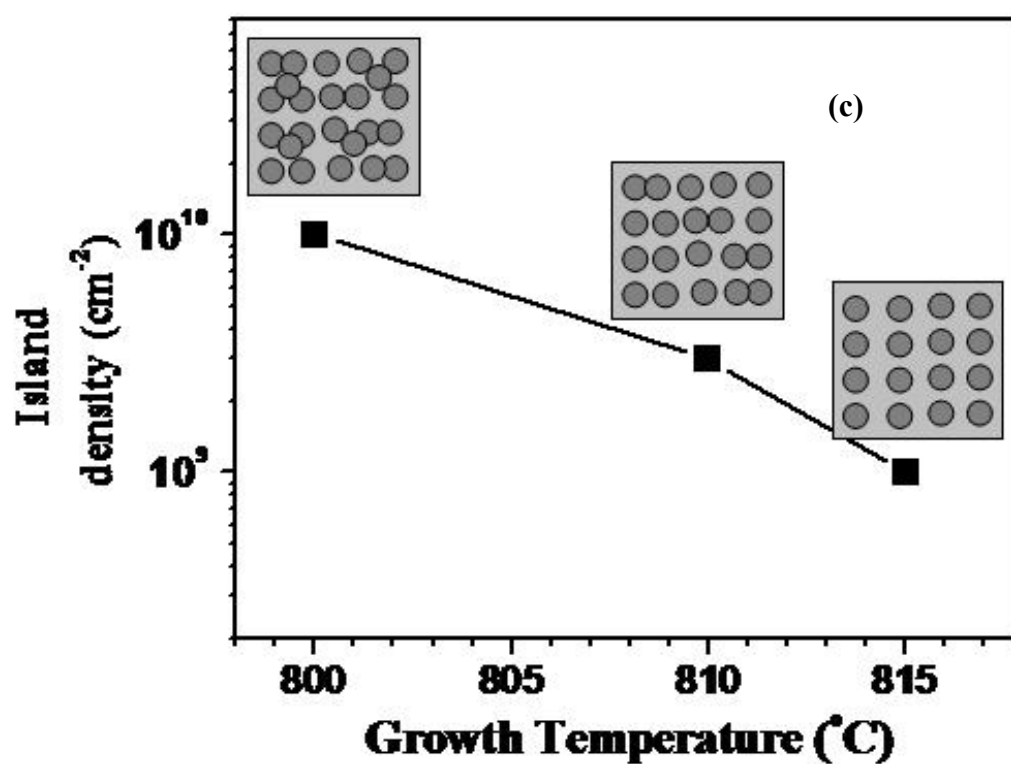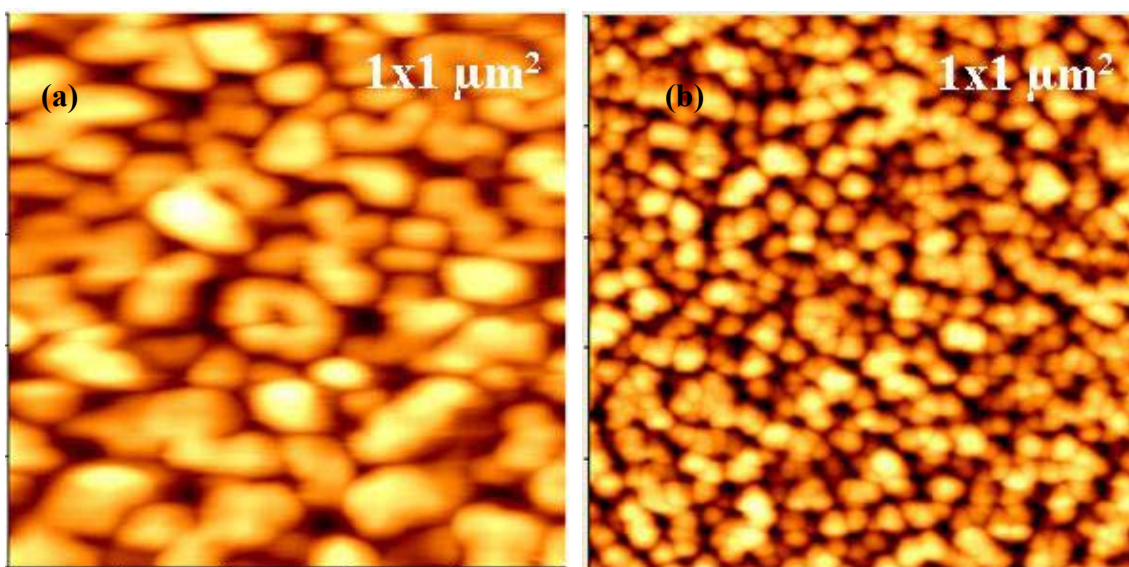
Figure 4.15 AFM images of GaN nanostructures as a function of growth temperatures
(a) at 1050 ℃ or (b) at 815 ℃, and (c) a graph of island as a function of
growth temperature.

However, GaN nanostructures were firstly grown at 1050 °C as the same growth temperature for a typical bulk GaN growth. AFM image [Figure 4.15 (a)] shows the nanostructures are too big and tend to transit 2D growth resulting in low nanostructure density. So the growth temperature was reduced to 815 °C. Figure 4.15 (b) shows that small GaN nanostructures with lateral dimensions below 50 nm and low aspect ratios were obtained using a relatively low temperature of 815 °C.
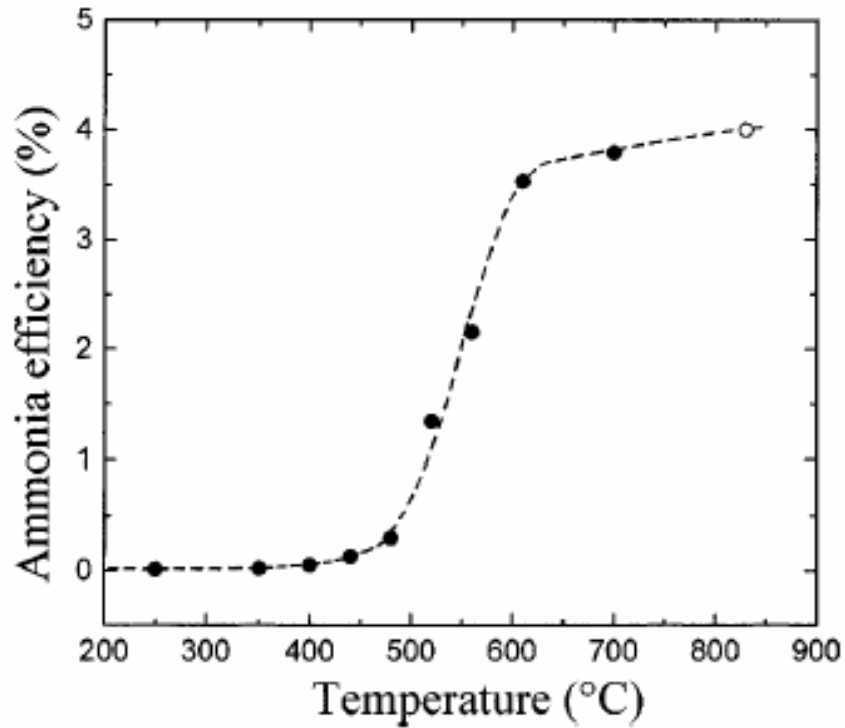
Figure 4.16 Reaction efficiency of ammonia with different temperatures.

In the lower than 750 °C, it was hard to control and even form high quality GaN, because NH_3 has a higher decomposition energy than TMGa precursor as seen Figure 4.16. The cracking efficiency of ammonia decreases as the growth temperature decreases

and even it would be zero at less than 500 ºC, which means that it gets more difficult to achieve high crystalline quality of GaN as the temperature lowers.

The kinetic energy of adatoms is influenced mainly by growth temperature. Ga adatoms are provided by the heat energy (i.e. growth temperature) which we supply. When the temperature increases, these adatoms have more energy which makes them unstable and easy to move around the surface [46]. The high surface migration of adatom leads to 2D growth and even evaporation, rather than 3D island formation. Therefore, lower growth temperatures facilitate the nanostructure growth. However, these nanostructures are still too big to have the characteristic of confinement. We reduced the nanostructure size by optimizing other growth parameters.

4.5.2 V/III ratio

V/III ratio is another important growth condition to form the self-organized GaN nanostructures, because it generally affects film surface energy and mobility of adatom. Geometric nanostructure size was investigated with a wide range of V/III ratio from 150 to some thousands. It was observed that the optimal ratio range is between 150 and 600 at 800 °C. Two AFM images in Figure 4.17 with different V/III ratios show this apparent difference for the density. The nanostructure density significantly increased as the V/III ratio decreased.

Typical V/III ratio for GaN is between 4000 ~ 6000. Some hundreds of V/III ratio are low, which becomes metal Ga-rich condition for this growth. However, typical GaN surface energy is about 2 J/m^2. But The GaN grown under a low V/III ratio has a higher surface energy than that energy, which improve the nanostructure density.
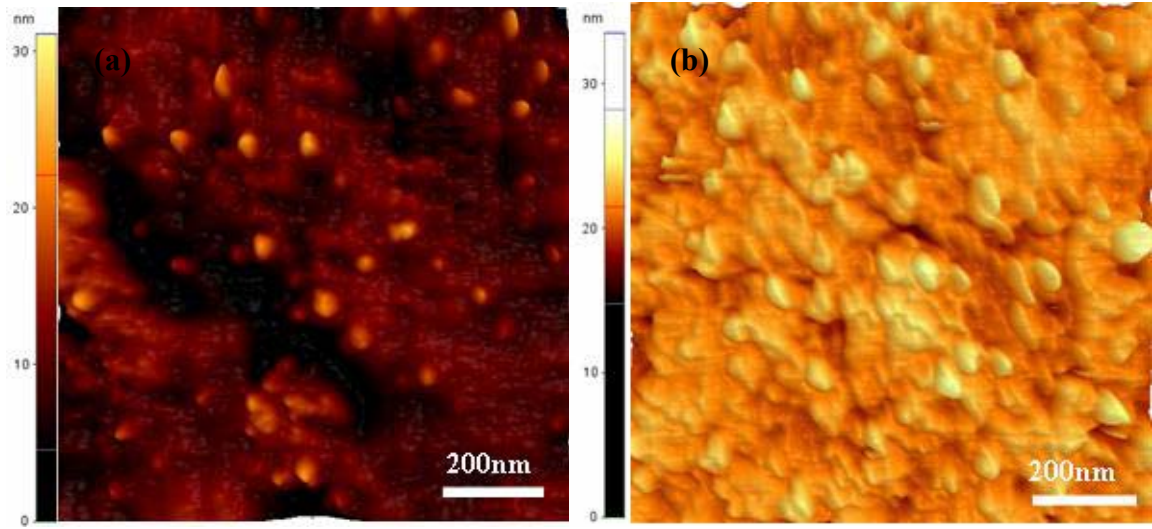
Figure 4.17 AFM images for V/III ratio (a) 200 and (b) 300.

4.5.3 TMGa Flow

Two above parameters mainly allowed the self-organized GaN nanostructures to be formed. But TMGa flow is also influenced on the growth mode, because it is related to growth rate. In this work, the TMGa flow was determined to control the amount of material deposited. This flow should be under control with the small amount of change due to fast transition of growth mode. Figure 4.18 shows that the surface morphology governed by the growth mode dramatically changes with TMGa flow. A low flow does not allow nanostructures to be generated [see Figure 4.18 (a)], while a high flow accelerates the growth rate and transits lateral growth by island coalescence [see Figure 4.18 (c)]. Therefore, the proper amount of TMGa flow is required for the self-organized GaN nanostructures [see Figure 4.18 (b)].
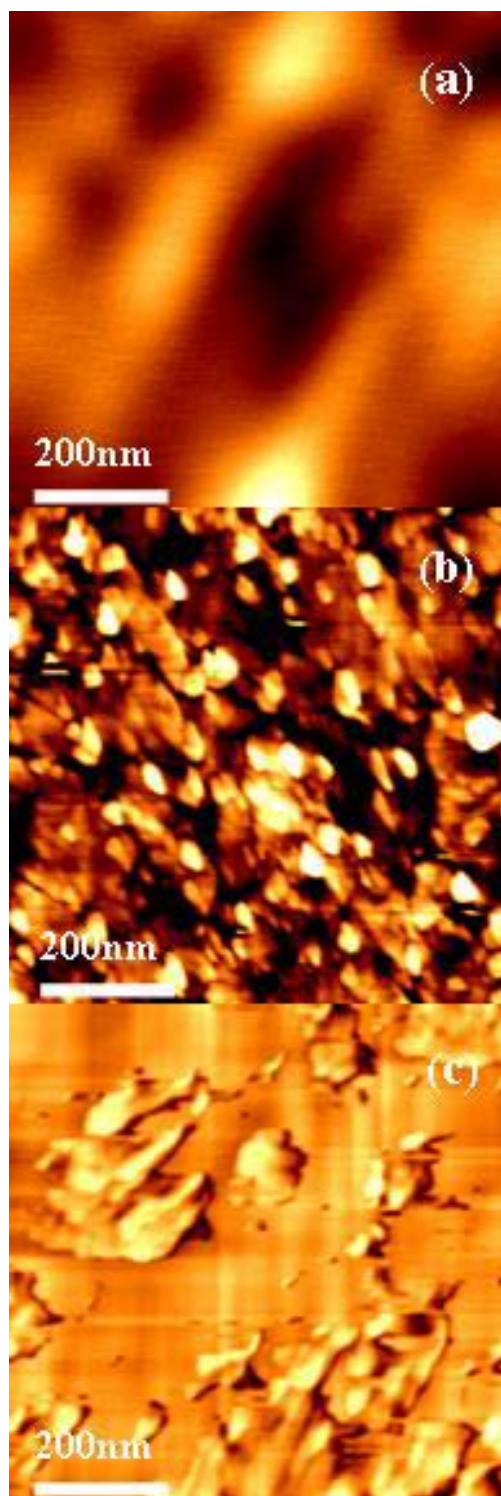
Figure 4.18 AFM images of GaN nanostructures with different amounts of TMGa precursor.
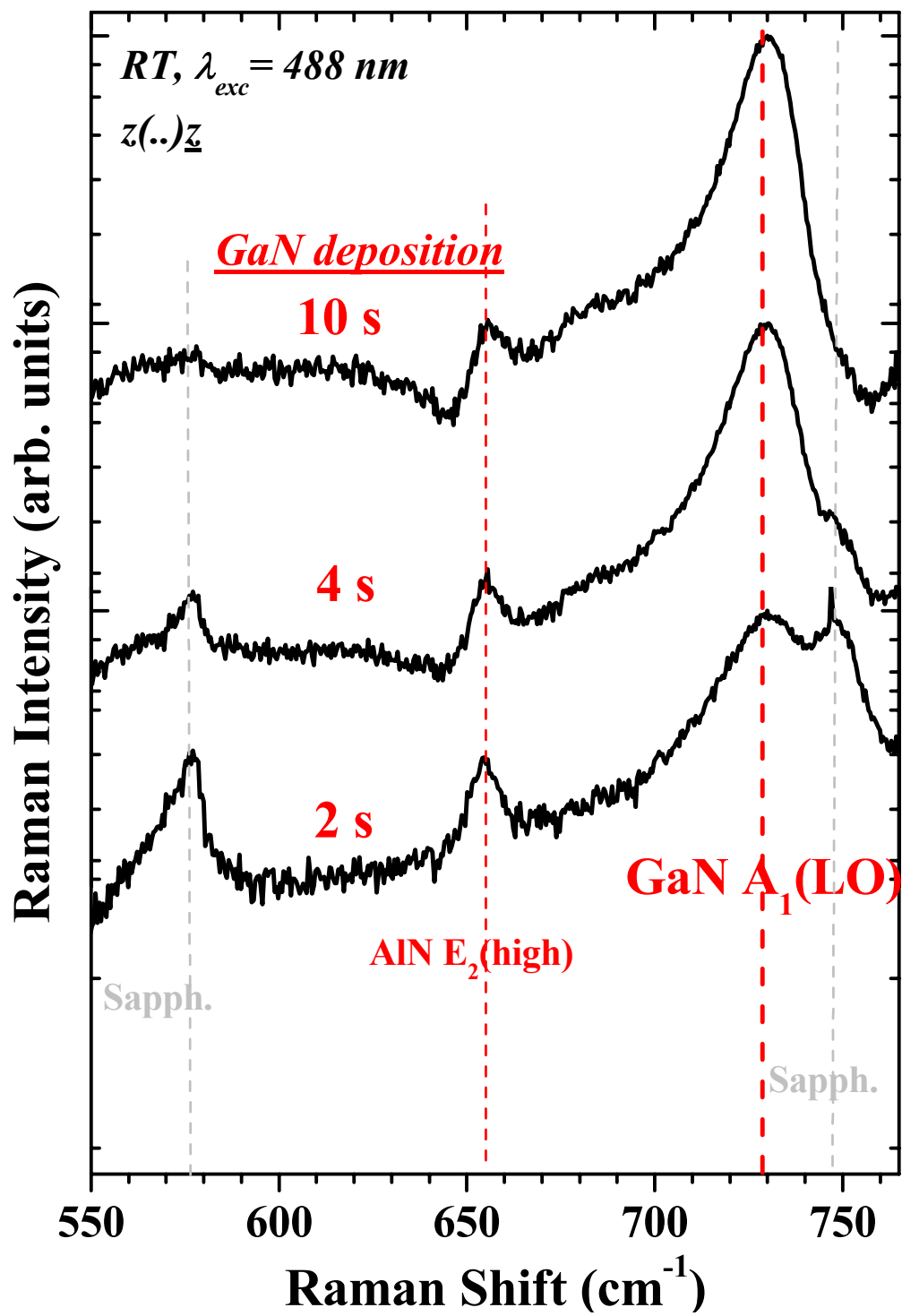
Figure 4.19 Raman measurement on GaN nanostructures on AlN.

Micro-Raman spectroscopy was exploited to study the lattice dynamics of the nanostructures. In Figure 4.19, the intensity of the GaN A_1(LO) mode increased as deposition time increased, while intensities of AlN (656 cm^{-1}) and sapphire (750 cm^{-1}) decreased, respectively. In addition, the existence of the GaN A_1(LO) mode provides evidence of the high crystalline quality of the nanostructures under the extremely metal-rich growth conditions at relatively low deposition temperatures.

4.6 Post-growth treatment

The primary optimization of growth conditions (i.e. growth temperatures of 815°C and V/III ratios between 150 and 600) provided GaN nanostructures. However, preliminary nucleation studies revealed that a thermal activation step after the GaN deposition was necessary to promote the formation of nanostructures having typical lateral dimension of 30 nm and height of 5nm with a density of more than $1x10^{10}$ cm^{-2}. In all of the growth, the activation step was performed with a temperature ramp applied in the reactor under a nitrogen atmosphere immediately after GaN deposition. Figure 4. 20 shows that a clear transition to 3D growth mode was observed through the activation step.

Since this activation step provides the growth transition from 2D to 3D as well as recrystallization, low activation temperature or even no this step restricts 3D growth transition and good optical property. However, for temperature ramps up to 950 ºC and above, the nanostructures had a lateral dimension of more than 100 nm, indicating a ripening of the islands [18]. In this work, the thermal activation was performed between 800 and 850 °C for a couple of minutes.
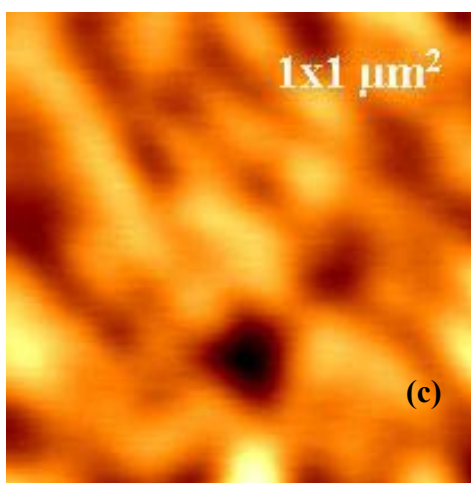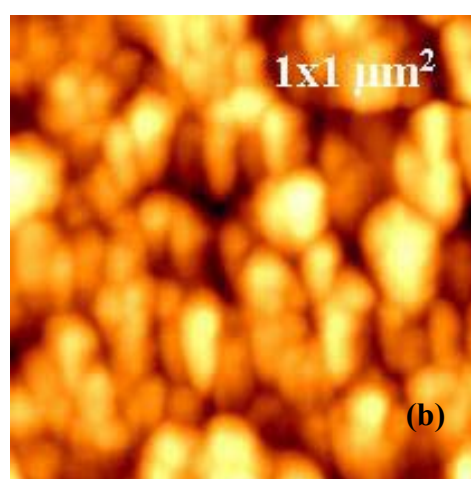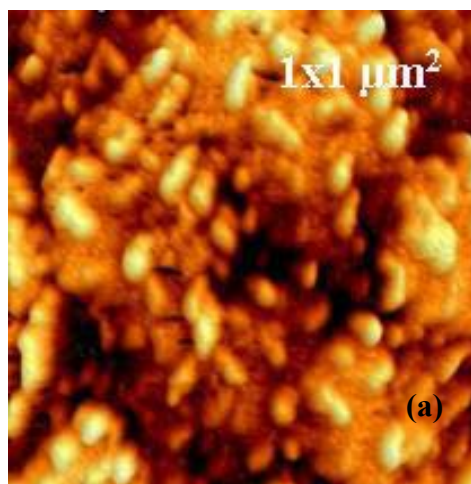
Figure 4.20 AFM images of surface morphologies as a function of thermal treatment temperatures (a) 800 ºC (b) 850 ºC and (c) 950 ºC

4.7 Optimization of growth conditions

Table 4.2. Optimized growth conditions

Growth parameter	Optimized values
Antisurfactant: Silicon	5μmole/min for 10 secs
Growth temperature	800 ºC ~ 815 ºC
V / III ratio	150 ~ 600
Growth pressure	100 Torr
Thermal treatment	820 ºC for 30 secs

Growth conditions have been optimized through all growth processes described in this section. All growths have the pre-growth treatment with 5μmole/min for 10 secs. Major growth conditions are growth temperature and V/III ratio optimized. The temperature and ratio were relatively low. And the thermal treatment was performed at 820 ºC for 30 secs. Table 4.2 shows these optimized growth condition.

However, two measurements were performed on the samples grown under these optimized growth conditions as seen in Figure 4.21. AFM image shows small islands with high density (Height : 5 ~7 nm, Diameter : 30 ~ 50 nm and Density : 1E10 cm^{-2}) and PL measurement shows that these nanostructures were optically activated at wavelength of around 380 nm.
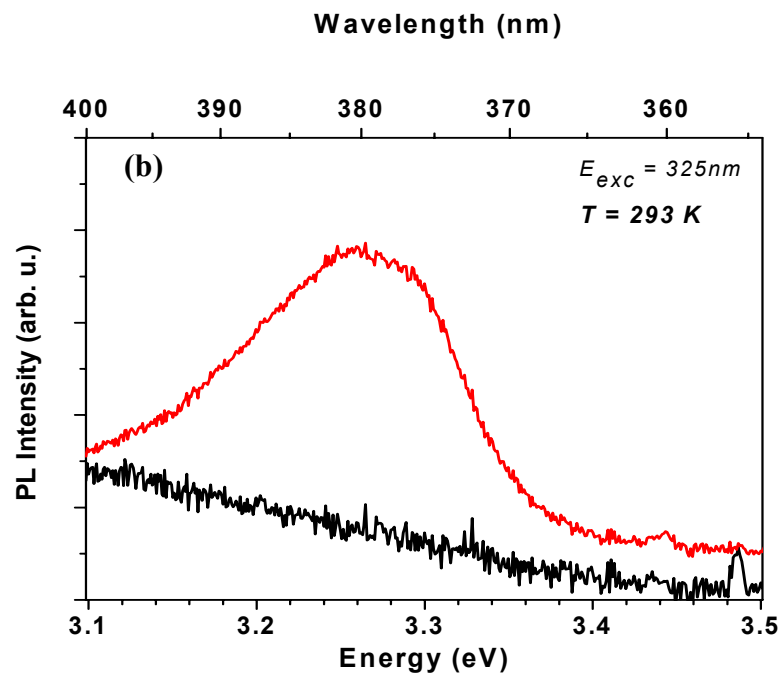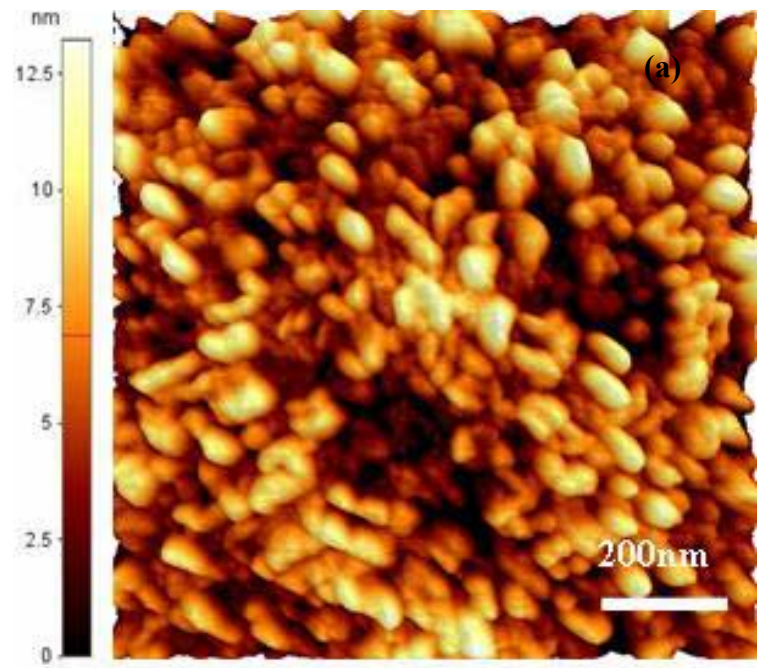
Figure 4.21 (a) AFM image and (b) PL measurement on the sample grown under the optimized growth conditions.

4.8 Controllable nanostructure size and its light emission energy

Table 4.3 Nanostructure size with different V/III ratios under the growth conditions.

Growth conditions	T_{growth} = 800 ~ 815 ºC P_{growth} = 100 Torr $T_{thermal}$ = 820 ºC for 30 sec
V / III ratio	**Size (Height / Diameter)**
150	2 ~ 4 / 20 ~ 30
200	5 ~ 7 / 30 ~ 50
300	8 ~ 10 / 50 ~ 100
600	> 11 / 100

Finally, the dot size can be controllable by changing mainly V/III ratio as seen Table 4.3. The size can vary from 2 nm to above 10 nm with V/III ratio range between 150 and 600. Another important observation is that the light emission wavelength of GaN nanostructure changes with different dot sizes. Figure 4.23 shows that smaller dot has a shorter light emission wavelength.

The optical properties of GaN nanostructure with the wurtzite structure result from a balance between confinement and piezoelectric effects. GaN nanostructure/AlN system has strong localization of carrier resulting in a suppression of non-radiative recombination and (spontaneous and piezoelectric) polarizations resulting in an internal electric field. The red-shift of the QD emission relative to excitonic emission in GaN

results from the piezoelectric effect while the blue-shift is caused by confinement. The blue-shift is evident for small dots and the red-shift occurs with the increasing the height of the dots. So it is showing that the control of dot size is very important to get desired color wavelength.
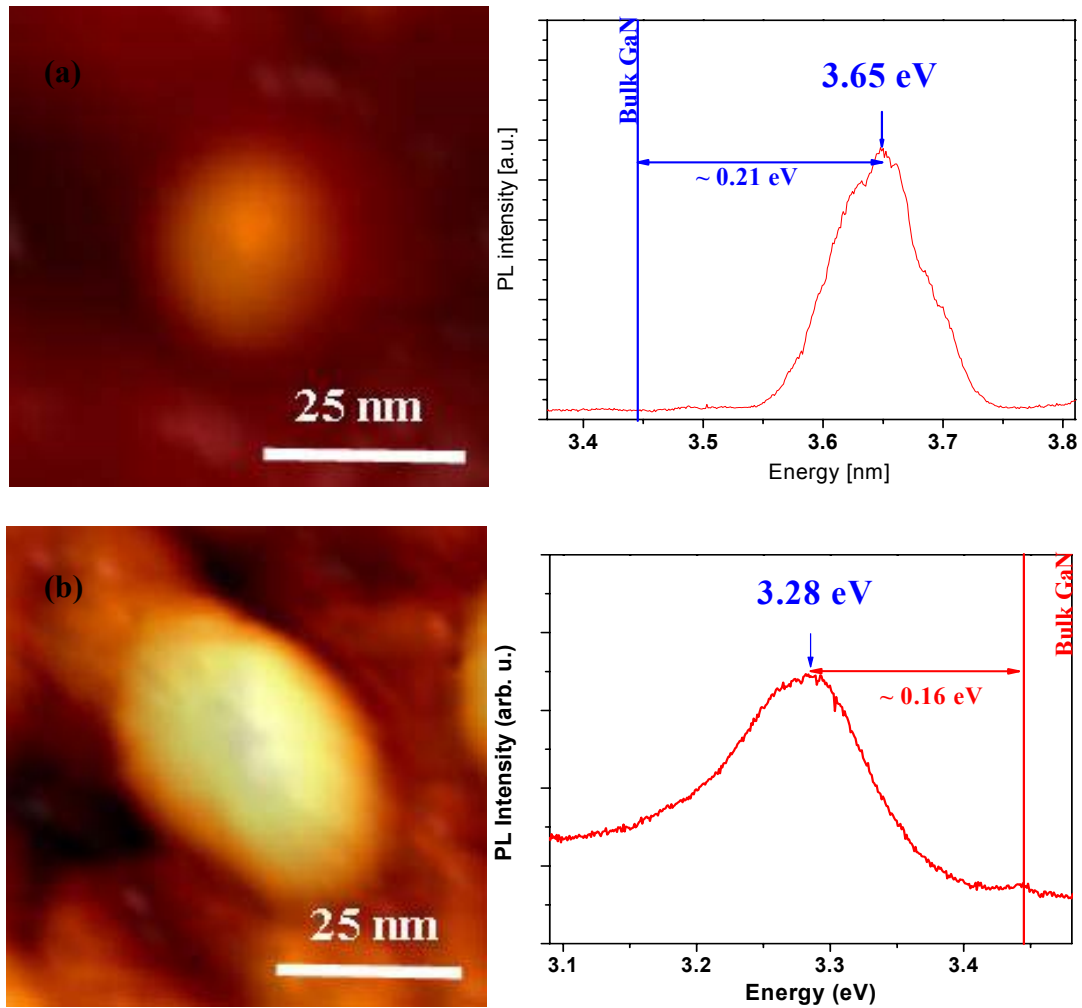
Figure 4.22 AFM images and PL measurements with different dot sizes.

4.9 References

[1] S. Nakamura and G. Fasol, *The Blue Laser Diode*, Berlin, Germany: Springer-Verlag (1997).

[2] Y. Arakaw, H. Sakaki, Appl. Phys. Lett. 40 (1982) 939

[3] H. Morkoc, Nitride Semiconductors and Devices, Berlin, Germany: Springer-Verlag (1999).

[4] D. Bimberg, M Grundmann, and N. Ledentsov, "Quantum Dot Heterostructures", John Wiley & Sons Ltd, (1988).

[5] F. Widamann, B. Daudin, G. Feuillet, Y. Samson, J. Rouviiere, and N. Pelekanos, J. Appl. Phys. **83**, 7618 (1998).

[6] F. Widamann, J. Simon, B. Daudin, G. Feuillet, J. Rouviiere, N. Pelekanos, and G. Fishman, Phys. Rev. B **58**, R15989 (1998).

[7] B. Daudin, F. Widmann, J. Simon, G. Feuillet, J. Rouviere, N. Pelekanos, and G. Fishmann, MRS Internet J. Nitride Semicond. Res. **451**, G9.2 (1999)

[8] M. Copel, M. Reuter, E. Kaxiras, and R. M. Tromp, Phys. Rev. Let. **63** No. 6, 632,

[9] Miton Ohring, "Materials Science of Thin Films, *Deposition and Structure*" Academic Press (2002)

[10] R. Naone, and L. Coldren, J. Appl. Phys. **82** (5), (1997)

[11] J. Neugebauer, Phys. Stat. Sol. (c) **0**. No. 6, 1651 (2003)

[12] D. Eaglesham, F. Unterwald, and D. Jacobson, Phys. Rev. Let. **70** No. 7, 966, (1993).

[13] F. Frank and J. Van der Merwe, Proc. Roy. Soc. Lond. A, 198 (1949) 205

[14] K. Nakajima, T. Ujihara, N. Usami, K. Fujiware, G. Sazaki, and T. Shishido, J. Cryst. Growth **260**, 372 (2004).

[15] M. Volmer and A. Weber, Z. Phys. Chem., 119 (1926) 277.

[16] W. Seifert, N. Carlsson, M. Miller, M. Pistol, L. Samuelson, L. Wallenberg, Prog. Crys. Growth Charact. **33** 423 (1996)

[17] I. Stanski and L. Krastanov, Akad. Wiss. Lit. Mainz Math. –Natur. K1. Iib 146 (1939) 797.

[18] I. Daruka, and A. Barabasi, Phys. Rev. Let. **79** No. 19, 3708, (1997).

[19] E. Iliopoulos, K. Ludwig, T. Moustakas, Ph. Komninou, T. Karakostas, G. Nouet, and S. Chu, Mat. Sci. & Eng. **B87** 227 (2001).

[20] F. Ponce, *Microstructure of Epitaxial III-V Nitride Thin Films*, 1997

[21] M. Miyamura, K. Tachinana, T. Someya, and Y. Arakawa, Phys. Stat. Sol (b) 228 (2001) 191

[22] M. Miyamura, K. Tachinana, T. Someya, and Y. Arakawa, J. Cryst. Growth 237-239 228 (2002) 1316

[23] B. Daudin, F. Widmann, G. Feuillet, Y. Samson, M. Arley, and J. Rouiere, Phys. 56 (1997) R7069

[24] Gerald B. Stringfellow, 'Organometallic Vapor-Phase Epitaxy, Theory and Practice", Academic Press, ISBN 0-12-673842-4 (1999)

[25] A. Gossard, J. English, P. Petroff, J. Cibert, G. Dolan, S. Pearton, *J. Crys. Growth*, **81**,101 (1986)

[26] X. Shen, s. Tanaka, S. Iwai, Y. Aoyagi, J. Crys. Growth, 201/202 (1999) 402.

[27] D. Romanov, V. Mitin, M. Stroscio. Physica B, 316 (2002) 359

[28] A. Matsuse, N. Grandjean, B. Damilano, and J. Massies, J. Crys. Growth, 274 (2005) 387.

[29] V. Dmtriev, K. Irvine, A. Zubrilov, D. Tsvetkov, V. Nicolacv, M. Jakobson, D. Nelson, and A. Sitnikova, *Gallium Nitride and Related Materials*, MRS (1996)

[30] S. Tanaka, S. Iwai, and Y. Aoyagi, Appl. Phys. Lett., 69 (1996) 4096.

[31] M. Gherasimova, G. Cui, S. Jeon, Z. Ren, D. Martos, J. Han, He and A. V. Nurmikko, Appl. Phys. Lett. **85** 2346 (2004)

[32] S. Tanaka, S. Iwai, Y. Aoyagi, J. Crystal Growth 170 (1997) 329.

[33] J. Hwang, S. Seong, S. Tanaka, S. Iwai, Y. Aoyagi, P.J. Chong, Bull. Kor. Chem. Soc. 18 (1997) 1133.

[34] E. S. Dettmaer, B. Romenesko, H. Charles Jr., B. Carkhuff and D. Merrill, IEEE Trans. on Comp., Hybrids and Man. Tech., 12 (1989) 543

[35] G. Slack, J. Phys. Chem. Solids, 34, 321, (1973)

[36] T. Ogino and M. Aoki, Jpn. J. Appl. Phys., 183 1049 (1979)

[37] H. Amano, I. Akasaki, K. Hiramatsu, and N. Sawaki, Thin Solid Films 163 (1988) 415.

[38] D. Zhao, J. Zhu, D. Jiang, H. Yang, J. Liang, X. Li, and H. Gong, J. Crystal Growth 289 (2006) 72.

[39] T. Mihopoulos, V. Gupta, K. Jensen, J. Crystal Growth 195 (1998) 773.

[40] K. Nakamura, O. Makino, A. Tachibana, K. Matsumoto, J. Organometallic Chem., 611 (2000) 514.

[41] H. Amano, N. Sawaki, I Akasaki, and Y. Toyoda, Appl. Phys. Lett.,48 (1986) 353.

[42] J. Kuznia, A. Khan, and D. Olson, J. Appl. Phys. 73 (1993) 4700.

[43] J. Han, T. Ng, R. Biefeld, M. Crawford, and D. Follstadet, Appl. Phys. Lett., 71 (1997) 3114.

[44] N. Gogneau, D. Jalabert, and E. Monroy, T. Shibata and M. Tanaka, B. Daudin, J. Appl. Phys. **94**, 2254 (2003).

[45] J. Brown, F. Wu, P.M. Petroff, J.S. Speck, Applied Physics Letters **84**, 690 (2004).

[46] M. Miyamura, K. Tachibana, and Y. Arakawa, Appl. Phys. Lett. 80 (2002) 3937.

CHAPTER 5

METAL DROPLET METHOD FOR SELF-ASSEMBLED

GaN NANOSTRUCTURE / AlGaN SYSTEM

5.1 Introduction

The GaN nanostructure on AlN is the common hetero-system to encourage formation of nanostructures due to 2.5% lattice mismatch resulting in S-K mode. But this system has a barrier to fabricate device applications, because AlN is an insulator which is hard to get n-type or even p-type doping for pn junction semiconductors. However, AlGaN, especially lower than 20% of Al molar fraction, is relatively easier to achieve the electrical injection of carriers. In this chapter, effects of growth conditions on nanostructure formation were investigated to achieve GaN nanostructure on AlGaN layer using the metal droplet method.

5.1.1 Mechanisms for GaN nanostructure/AlGaN

The previous growth technique which had been used in GaN nanostructure / AlN system was also utilized in this GaN nanostructure / AlGaN system. Pre-growth treatment, was performed. Various growth parameters were optimized. And even thermal treatment was performed in the post-growth treatment. But such small islands which are less 10 nm of height and 100 nm of diameter (as seen in Figure 5.1) could not be achieved, because the lattice mismatch between GaN and $Al_xGa_{1-x}N$ is too small to fabricate self-assembled

nanostructures which are formed in the GaN/AlN system using strain energy via the S-K growth mode. Therefore, other growth techniques are required to overcome the lower strain energy. In this chapter, a growth technique to achieve GaN nanostructures on top of AlGaN layer was investigated and their characterizations were followed.
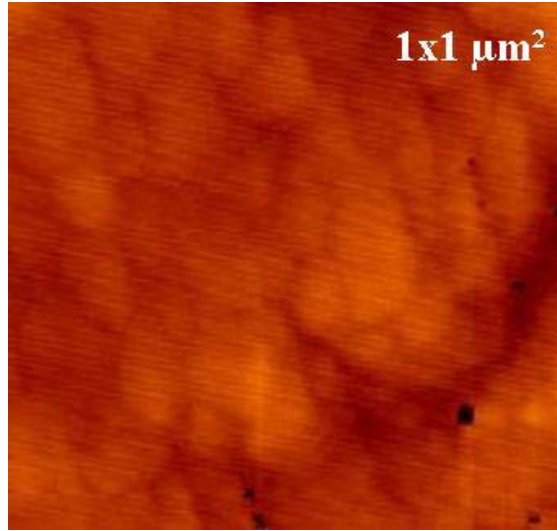
Figure 5.1 Surface morphology of GaN grown AlGaN.

The common technique utilized in lattice-matched systems is metal droplet method, also called to vapor-liquid-solid (VLS). In the method, a liquid droplet condensing from vapor phase transforms crystal solid under chemical vapor deposition conditions at a high temperature. This method was first demonstrated in 1964 by Wanger and Ellis [1] for the growth of silicon whickers with diameters from one hundred nanometers to hundreds of microns, and in 1993 Koguchi, *etc*. proposed the formation of nanometer Ga droplets on a substrate and conversion into GaAs QDs after an exposure to arsenic vapor [2].
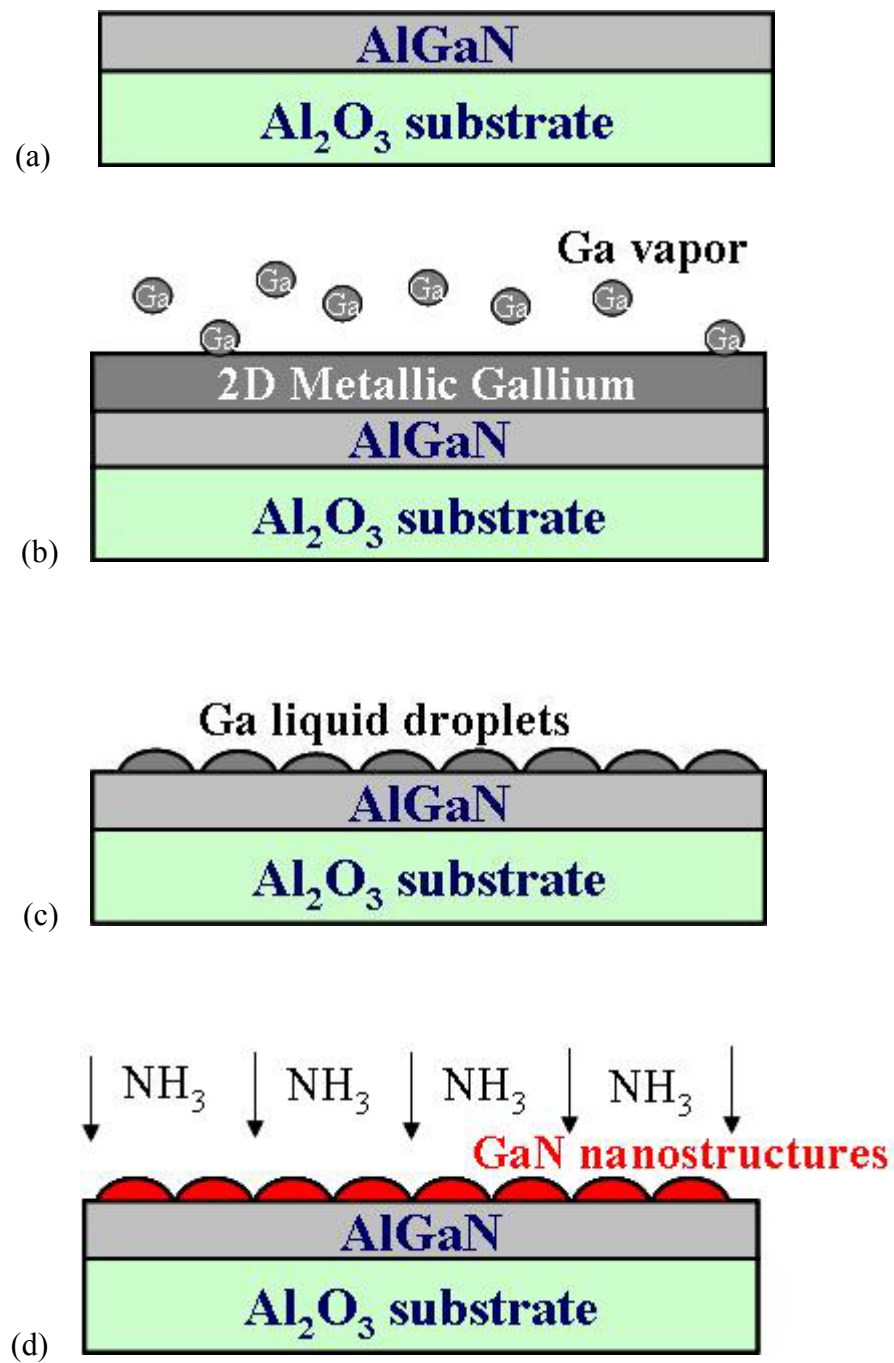
Figure 5.2 Growth mechanism step of GaN nanostructure growth on AlGaN.

In this method, Ga source flows in on the top of AlGaN. Then very thin liquid 2D metallic Ga bi-layer is formed on the surface. This 2D metallic layer is transformed into nanoscale liquid droplets due to a high surface tension of liquid phase. After that, these Ga droplets can be crystallized for GaN nanostructures in the existence of ammonia as a nitrogen source. Therefore, the formation of metal droplets presents an alternative route to nanostructures by converting the droplets into crystalline GaN nanostructures. Figure 4.2 shows this growth mechanism.

The VLS method provides remarkable merits to the GaN nanostructure /AlGaN system. This technique does not need antisurfactants such as Si or surface strain mismatch, because the surface energy of liquid metal is much higher than that of solids [3, 4]. The gallium is a liquid at low temperature of 30 ºC. 2D thin film of metallic Ga deposited on a substrate transforms into nanoscale liquid droplets due to a high surface tension of liquid phase. Then, these droplets can be crystallized in the existence of ammonia as a nitrogen source. The formation of metal droplets presents an alternative route to nanostructures by converting the droplets into crystalline GaN nanostructures

5.2 AlGaN growth

5.2.1 Introduction

AlN film has been utilized for various applications, but the majority of interest in AlN results from its alloy with GaN due to a wide regulable band gap energy from 3.4 to 6.2 eV. Fabrication of AlGaN-based optical devices allows to develop deep UV optoelectronic applications such as solid-state white light source, chemical-biological detection, super high-density storage, fine lithography, and flame detection [5, 6]. It is difficult, however, to make high-quality AlGaN films with high Al content due to the parasitic reaction of TMAl and NH_3 in the vapor phase [7, 8]. Besides, direct reduction of carrier concentration and mobility in n (or p)-type doped AlGaN as a function of higher Al molar fraction is a current barrier to fabricate semiconductor devices. In this chapter, optimization of growth conditions and surface morphology of AlGaN epitaxial layer has been investigated by avoiding the parasitic reaction.

AlGaN is one of common ternary III-nitride material with InGaN. $Al_xGa_{1-x}N$ has properties mixed with AlN and GaN, which is mostly governed by Vegard's law. Structural types of both GaN and AlN are same wurtzite structures. A lattice mismatch between them is 2.5 % along the a-axis and 4 % along the c-axis. Lattice spacing of $Al_xGa_{1-x}N$ is smaller while the optical absorption edge was slightly larger as Al content increases. Moreover, the covalent cation radii are 1.26 Å for gallium and 1.18 Å for aluminum, which means that the low covalent difference results in realizing AlGaN solid solutions. In electrical properties, resistivity increases up to ten orders of magnitude, and the carrier concentration and mobility remarkably decrease with higher Al content.

However, the optical wavelength will be adjusted from 200 nm to 364 nm by changing Al content.

5.2.2 General AlGaN growth techniques

The first achievement of AlGaN growth was performed in 1973 [9] and Baranov et al. realized the first epitaxy on sapphire using CVD in 1978 [10]. In MOCVD technology, Khan and his group firstly succeeded in AlGaN growth using TMAl and NH_3 as sources.

All of AlGaN layers were grown on sapphire substrates and trimethylgallium, trimethylaluminum, and ammonia were used as precursors. After high temperature pre-bake of sapphire substrate under H_2 ambient, growth temperature decreases to 550 ºC to deposit a low temperature buffer layer. In our work, various kinds of buffer layers are performed, but thin LT-AlN layer is mostly utilized as the buffer layer for AlGaN epitaxial layer. AlGaN layer was grown at high temperature of more than 1000 ºC under low pressures (50 ~ 100 Torr) to get good quality AlGaN film [11].

In this work, Al content in AlGaN layer was fixed at 15 % which was determined by x-ray diffraction measurements. The control of Al composition in $Al_xGa_{1-x}N$ can be adjusted by changing the flow ratio of TMGa and TMAl. However, incorporation of a large amount of aluminum into AlGaN layer is not easily achieved by only increasing TMAl flow because parasitic reactions easily occur too. Therefore, optimization of growth conditions, for example reduction of growth pressure, is required for obtaining AlGaN film with high Al composition.
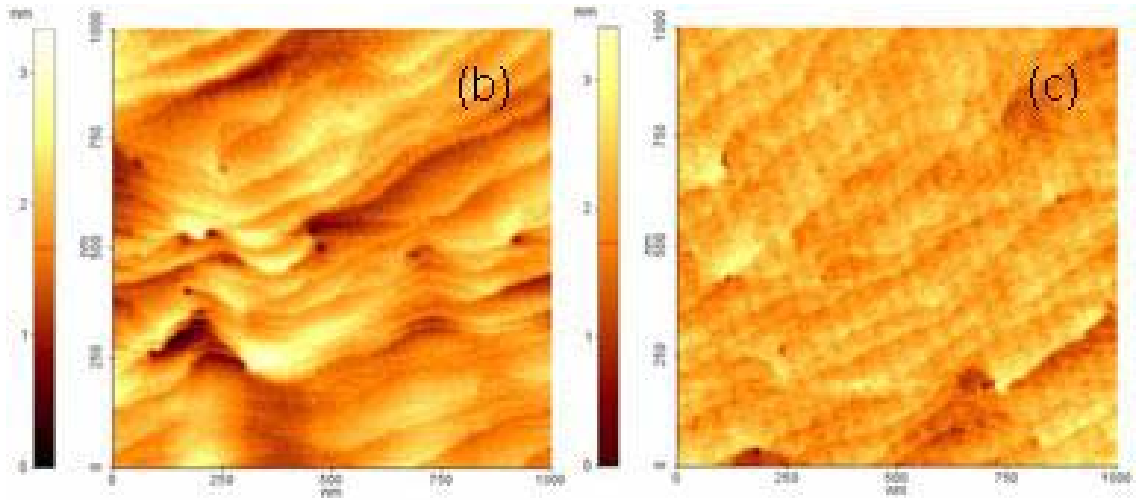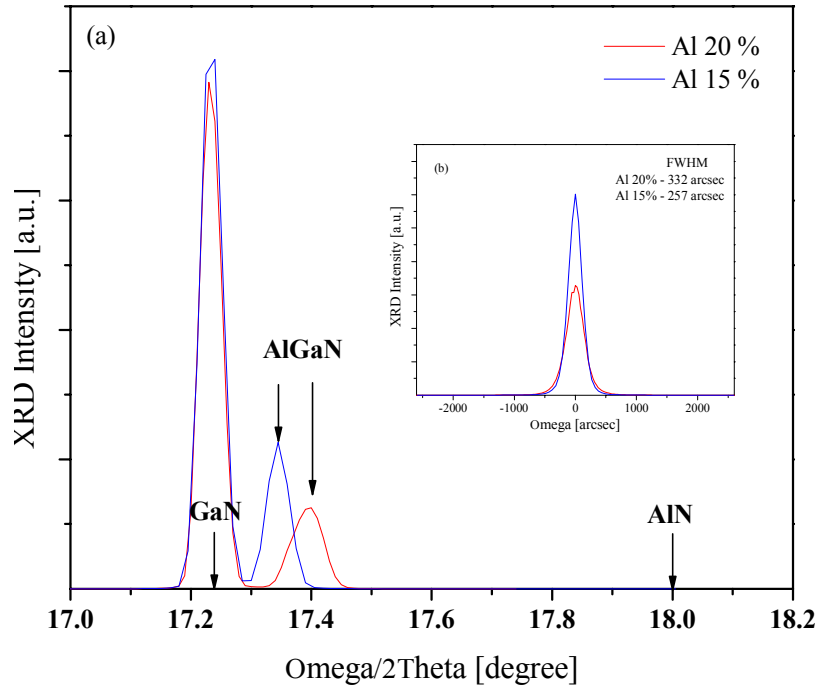
Figure 5.3 XRD spectra with different Al contents (15% and 20%) for (a) Omega/2Theta scans to show Al content and (b) omega scans to determine crystalline quality, AFM images of (c) Al 15% and (d) Al 20% in AlGaN grown on GaN.

5.2.3. Improvement of surface roughness

The most important issue for nanostructure is the growth of a smooth template. AlN or AlGaN layer on substrate is commonly used as templates of 2D GaN to prevent from poor wetting between GaN and the substrate [12]. But it is not easy to obtain smooth surfaces of these layers as nanostructure templates. Crystal quality and surface morphology get deteriorated as Al content in AlGaN layer increases. Figure 5.3 shows XRD and AFM results with different Al contents. XRD data show that AlGaN peak moves to the right side and FWHM of omega scan increases as higher Al composition. And AFM data shows surface morphology get rougher (RMS = 0.7 and 0.3 nm for Figure 5.3 (c) and (d) respectively). We investigated the effects of buffer layers on AlGaN growth, reactor pressure and V/III ratio on the incorporation of Al in AlGaN film, and optimized growth conditions to relieve surface roughness from higher Al incorporation.

A buffer layer is needed to relieve the lattice mismatch between AlGaN film and sapphire substrate. There were two common kinds of buffer layers grown on sapphire substrate: GaN and AlN. As seen in Figure 5.3, the surface morphology of AlGaN/GaN system is relatively smooth, because GaN film has a better characteristic giving more nucleation sites as a buffer layer. However, there are cracks in AlGaN layer grown on GaN as seen in Figure 5.2. Cracks are formed due to the biaxial tensile strain caused by lattice and thermal expansion mismatches at room temperature [13, 14]. Even if AlGaN is grown on GaN without cracking, the optical wavelength from GaN buffer layer can overlap the wavelength from GaN nanostructure and it makes the wavelength wider. Therefore, GaN layer is not proper for a buffer layer of AlGaN.
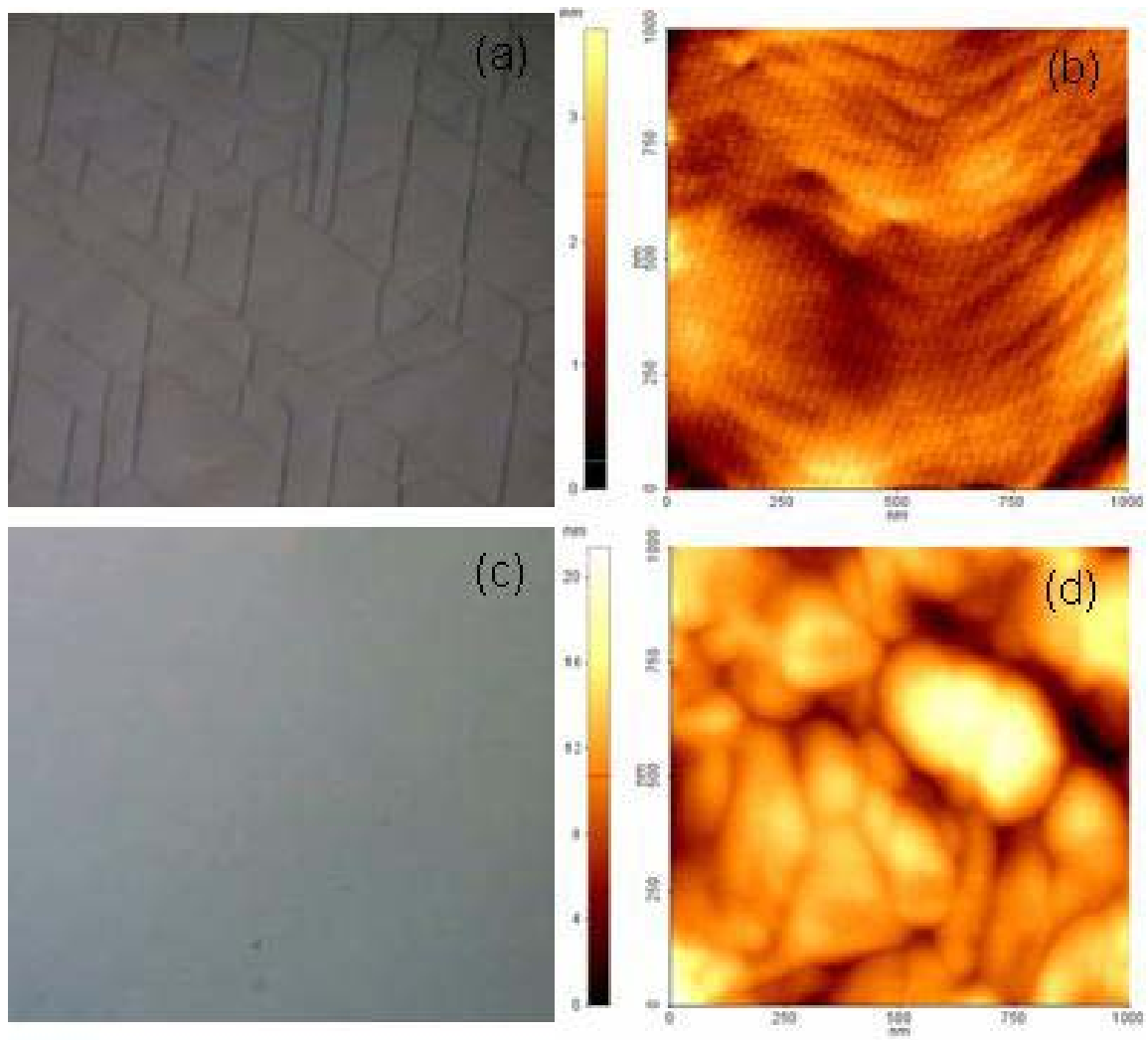
Figure 5.4 (a) A microscope image and (b) An AFM image on AlGaN grown on GaN buffer layer, and (c) a microscope image and (d) an AFM image on AlGaN grown on AlN buffer layer.

On the other hand, Figure 5.4 (c) shows that the AlN buffer layer gives a free-crack AlGaN epilayer. However there is a worse surface morphology of AlGaN epilayer grown on AlN buffer layer in compared with GaN buffer layer [see Figure 5.4 (b) and (d)]. In this work, the improvement of AlGaN surface morphology was performed. Figure 5.5 shows AFM images and *in-situ* monitoring measurements during AlGaN growth to compare a LT AlN buffer layer with a HT AlN buffer layer. We grew two AlGaN samples on an 80nm AlN at 1100 ºC and a 20nm AlN at 550 ºC. The AlGaN layer on LT AlN gets smoother than on HT AlN as seen in Figure 5.5 (b) and (d), surface morphologies of AFM images. A thin AlN grown at the low temperature relieves the lattice and thermal expansion mismatches and improves lateral growth (i.e. 2D like-growth) of AlGaN.
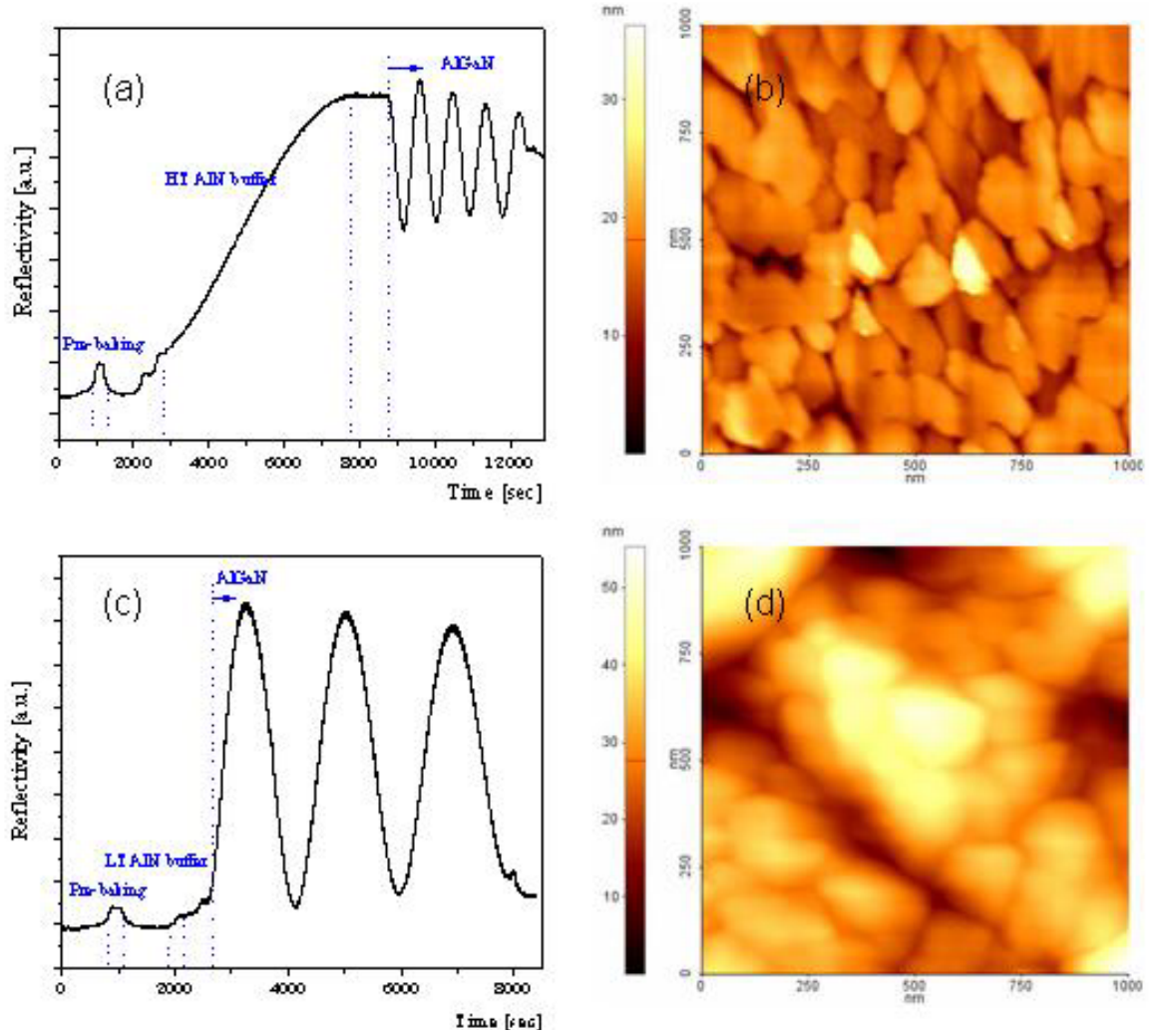
Figure 5.5 (a) An in-situ reflectivity spectrum and (b) An AFM image on AlGaN grown on HT AlN buffer layer, and (c) An in-situ reflectivity spectrum and (d) an AFM image on AlGaN grown on LT AlN buffer layer.

After a proper buffer layer was optimized, growth temperature was investigated from 1000 to 1100 ºC. Higher growth temperature trends to provide a better quality as higher Al content, but also enhances the parasitic reaction between TMAl and NH$_3$, which reduces growth rate. The more TMAl flux is required for the compensation of this reaction. However, the temperature was optimized at 1070 ºC for AlGaN film containing Al of 10 ~ 15 %.
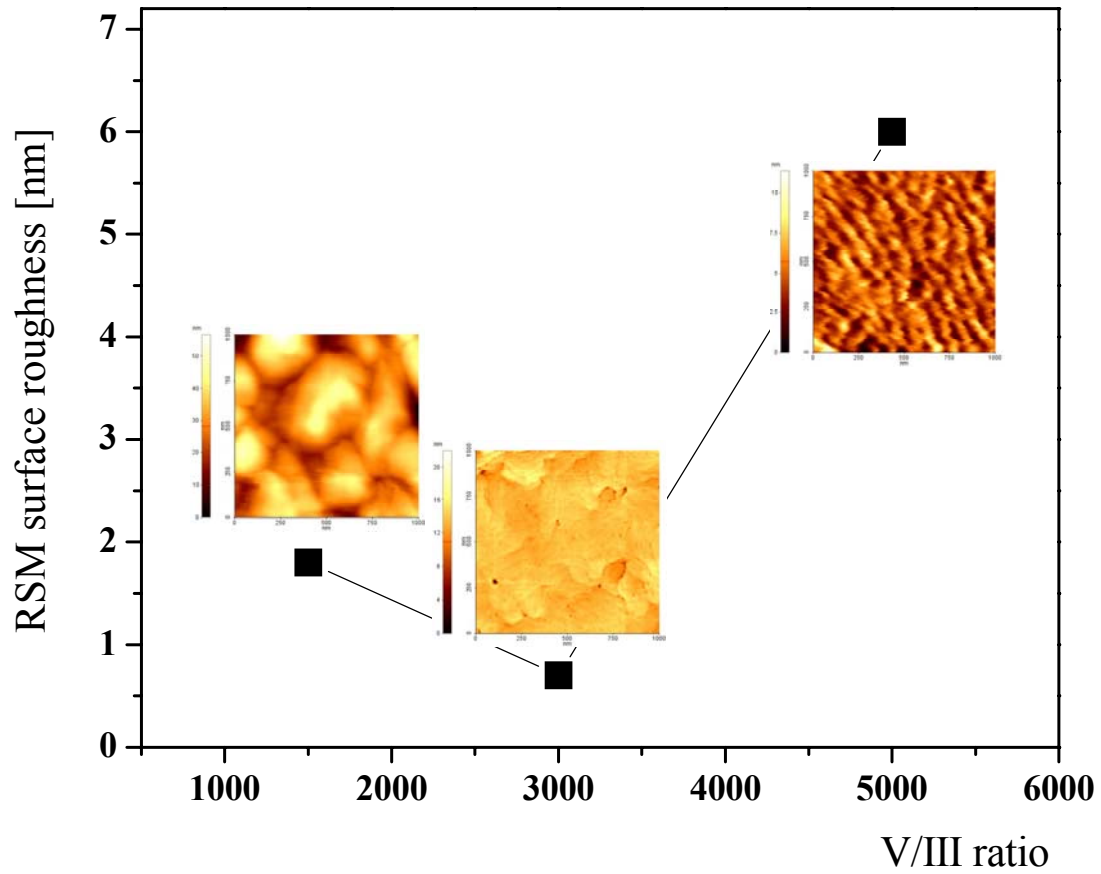
Figure 5.6 A graph of AlGaN surface roughness as a function of V/III ratios and their AFM images.

Growth Pressure was performed by changing from 30 to 200 Torr. The pressure also affects the growth rate because the pressure affects the mass transport mechanism of the precursor molecules even though the mechanism is also influenced by reactor geometry. Higher pressure results in reducing mass transport energy, which means that TMAl strongly reacts with NH_3 to deplete reactants. Therefore reducing pressure gives a better surface morphology when incorporation of Al content increases. However, the pressure was optimized at 50 Torr for AlGaN film containing Al of 10 ~ 15 %.

In the growth of AlGaN containing Al of less than 5 %, a typical V/III ratio is a couple of thousands Torr, similar to high temperature GaN growth. V/III ratio was varied by changing NH_3 from 1500 to 4500sccm. Figure 5.6 shows surface morphology from AFM images with different V/III ratios. The V/III ratio can affect both parasitic reaction and growth mode. A higher V/III ratio accelerates the parasitic reaction, whereas a lower V/III ratio restricts this reaction as well as 2D growth, which makes the surface rough. We have determined the optimized V/III ratio, 3000.

The growth parameters of AlGaN layer have been optimized. AFM measurement gives less than 10 Å and a rocking curve XRD measurement proves its high quality (FWHM < 400 arcsec), which is good enough to grow GaN nanostructures on top of this layer.

5.3 Formation of GaN nanostructures on AlGaN templates
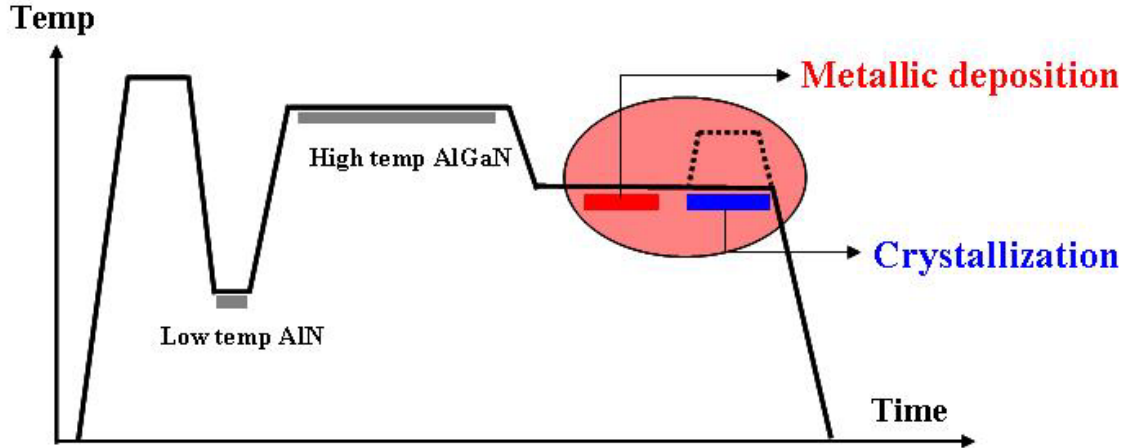
Figure 5.7 A growth process of GaN nanostructure on AlGaN.

Trimethylgallium (TMGa), trimethylaluminum (TMAl), and ammonia (NH_3) were used as the source precursors for Ga, Al, and N, respectively. Figure 5.7 shows a growth process of GaN nanostructure with temperature variation. 0.3 μm-thick $Al_{0.15}Ga_{0.85}N$ templates were grown on sapphire using an LT AlN buffer. After the growth of AlGaN at 1070 °C, ammonia and a carrier gas (H_2 or N_2) only flowed and the temperature was reduced for the deposition of gallium to take place. Ga deposition was achieved by flowing TMGa in the absence of ammonia; the ammonia flow was interrupted for a couple of minutes before TMGa was introduced to prevent from two dimensional GaN growth. The flow of TMGa (10 ~ 500 μmole/min) and the duration of deposition (less than 30 seconds) were performed to study the nucleation dynamics. The

formation of Ga droplets, including the nucleation dynamics and kinetics, is examined at the atomic scale.

5.4 Ga Metallic deposition

Even though island size and density are influenced by various growth parameters, a typical parameter to determine them is the coverage of 2D metallic thin film (i.e. Ga bilayer) over the substrate, because the metallic thin film transforms into liquid Ga droplets and its thickness determines size and density of these droplets. However, the thickness of the Ga bilayer is mainly affected by the amount of TMGa flow. In this work, we determined this thickness by obtaining growth rate from Epimatrics, *in-situ* reflectometry measurement, as seen in Figure 5.8. Comparison of Ga metallic film with bulk GaN in the *in-situ* reflectometry measurements provides growth rate, ~ 1 nm/sec. After studying of effects of TMGa flow rate and duration time, the optimal thickness of the metallic thin film prior to converting into Ga liquid droplets was estimated. In addition, AFM characterization was performed.
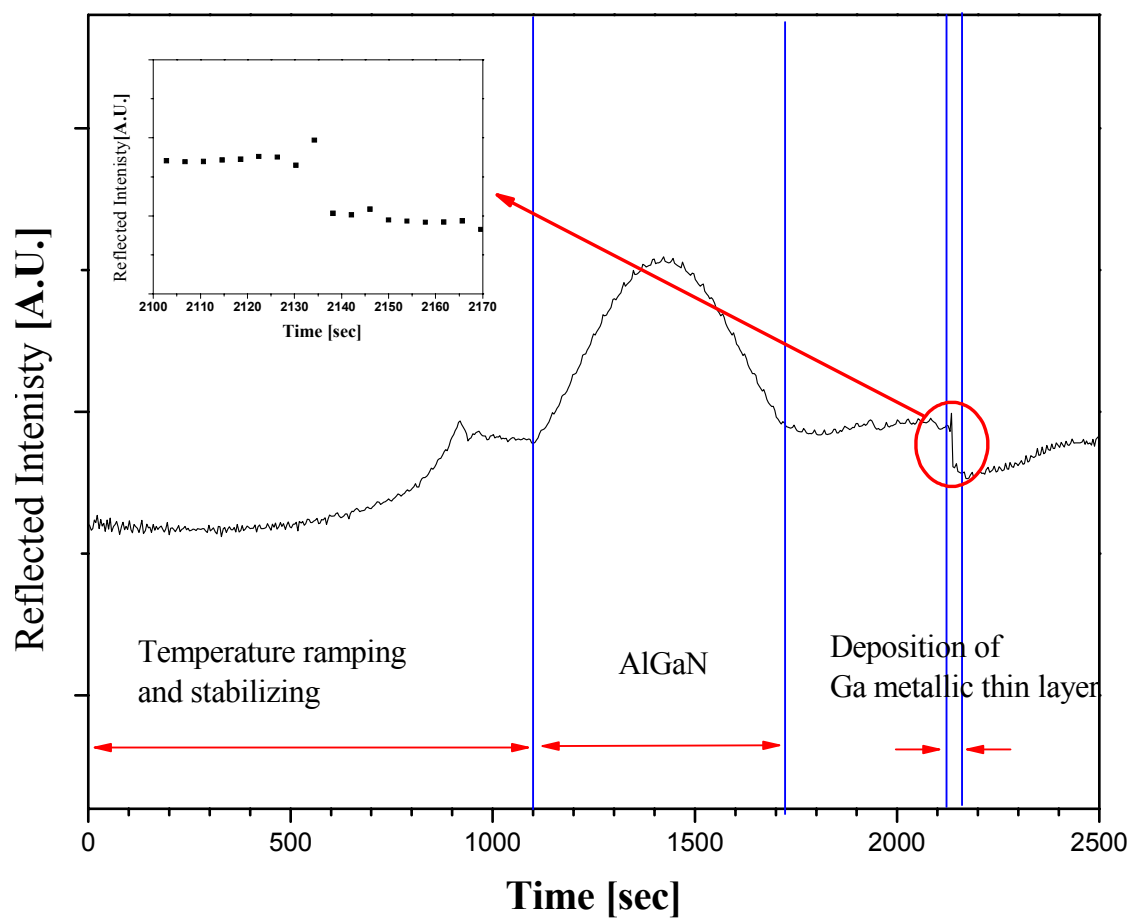
Figure 5.8 *In-situ* reflectometry measurement on GaN nanostructures on AlGaN
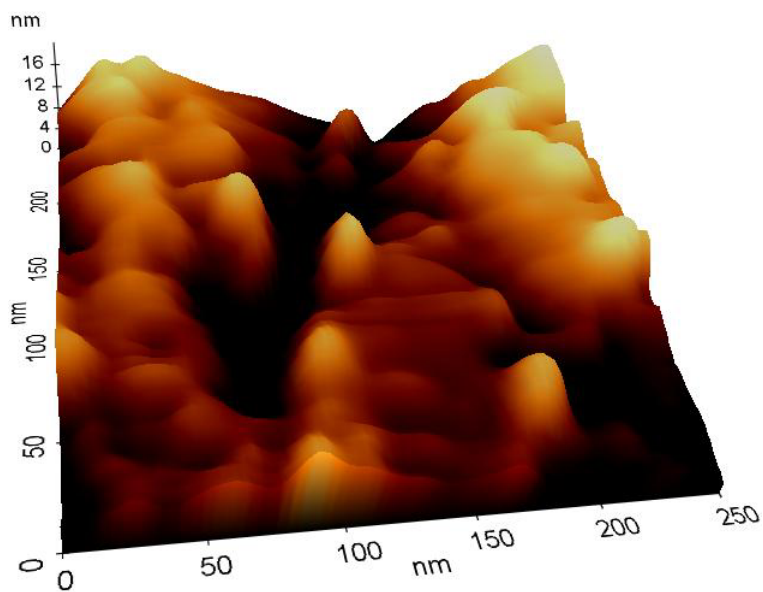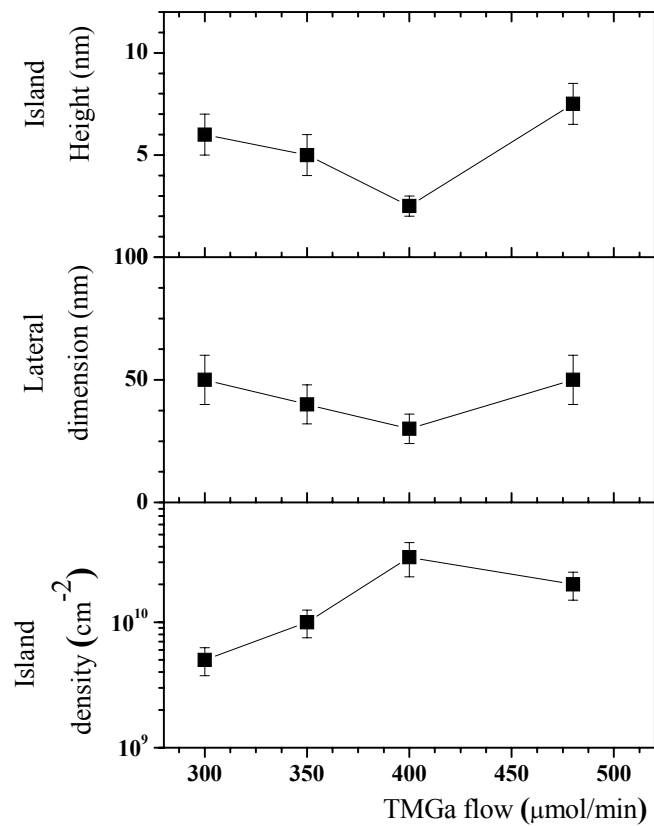
Figure 5.9 (a) Graphs of geometric GaN nanostructure as a function of TMGa source flow rate and (b) an AFM image for TMGa of 400 μmole/min.

Below an optimal TMGa flow, there is not thick enough of Ga bilayer to be formed, and even this was evaporated, rather than was converted into Ga liquid droplets. However, above the critical TMGa flow, it is too thick to transform. There are some of metallic thin layer reminding which could degrade GaN nanostructures for optical characteristics. We have optimized the TMGa flux, and island size was apparently minimized and density was maximized at this TMGa flow rate.

The initial deposition of Ga thin film proceeds through an occurrence of Ga bilayers near the surface steps of AlGaN. Beyond an equivalent (integrated) thickness, an onset of the formation of Ga nanodroplets was observed, putting adjacent to the background Ga bilayers. We flowed TMGa of up to about 500 μmol/min at 800 °C and the duration of TMGa flow was 9 seconds. Increasing TMGa flow reduces island size and improves island density, but above TMGa of 400 μmol/min, there was surplus material easily to happen ripened and coalesced each other, thus islands get larger and density decreases. Figure 5.9 shows the graphs of GaN nanostructure size and density as a function of TMGa flow rate. It results in that TMGa of 400 μmol/min is the optimal flow rate under these other growth conditions. But the optimal value will be change, if these other growth conditions are changed, because thickness of Ga metallic thin layer depends on TMGa flow as well as layer time.
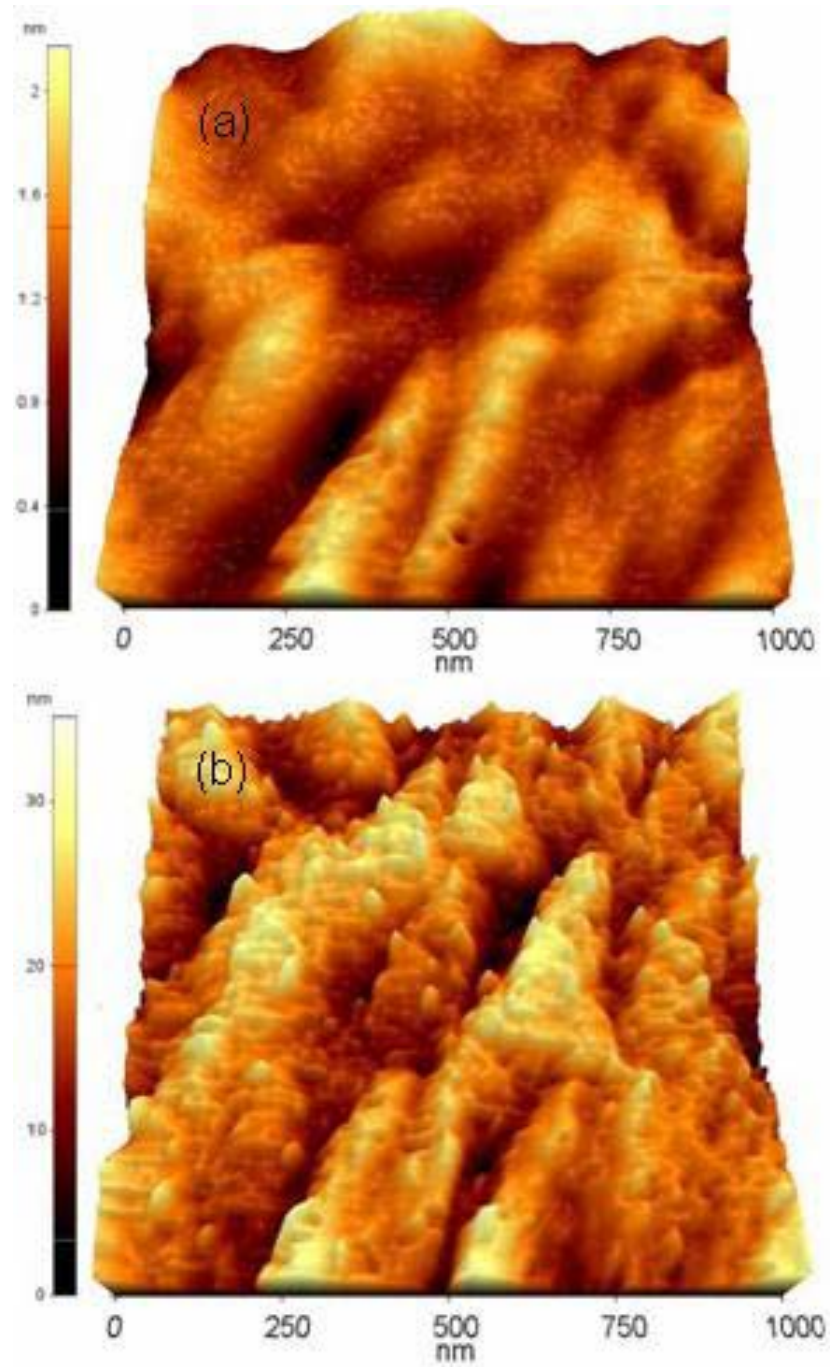
Figure 5.10 AFM images of GaN nanostructures on $Al_{0.15}Ga_{0.85}N$ with TMGa layer duration time of (a) 3 seconds and (b) 9 seconds.

TMGa flow time is important to determine the optimal thickness of 2D Ga metallic thin film. The duration time of 3 seconds was not enough to form the metallic thin layer, but the most material was evaporated as seen in Figure 5.10 (a). Islands began forming after 6 seconds passed, and 9 seconds was the most suitable time for optimization of the duration as shown Figure 5.10 (b). Finally, Figure 5.11 shows the optimal TMGa flow time is 9 seconds. Below that value it is not enough to provide metallic seeds converting to GaN nanostructures, while above that value adjacent islands each other was getting together and larger, thus their density decreased.

The mechanism of the formation of Ga nano-droplets depends on kinetic processes such as nucleation, surface diffusion, and ripening through grain growth. [15, 16] Theoretical modeling [17] has predicted the coexistence of mono-dispersed large droplets, regulated by the ripening process, with poly-dispersed small droplets as a result of continuous nucleation. As the flow of TMGa is increased, the nucleation barrier for droplet formation is reduced as a result of increased super-saturation, thereby leading to higher island densities, while the nominal thickness is preserved. Considerable narrowing of droplet size distribution is also observed with the reduction in the deposition time. A prudent selection of growth parameters such as temperature, super-saturation, and extent of ripening is expected to produce Ga droplets with controlled density and homogeneity.
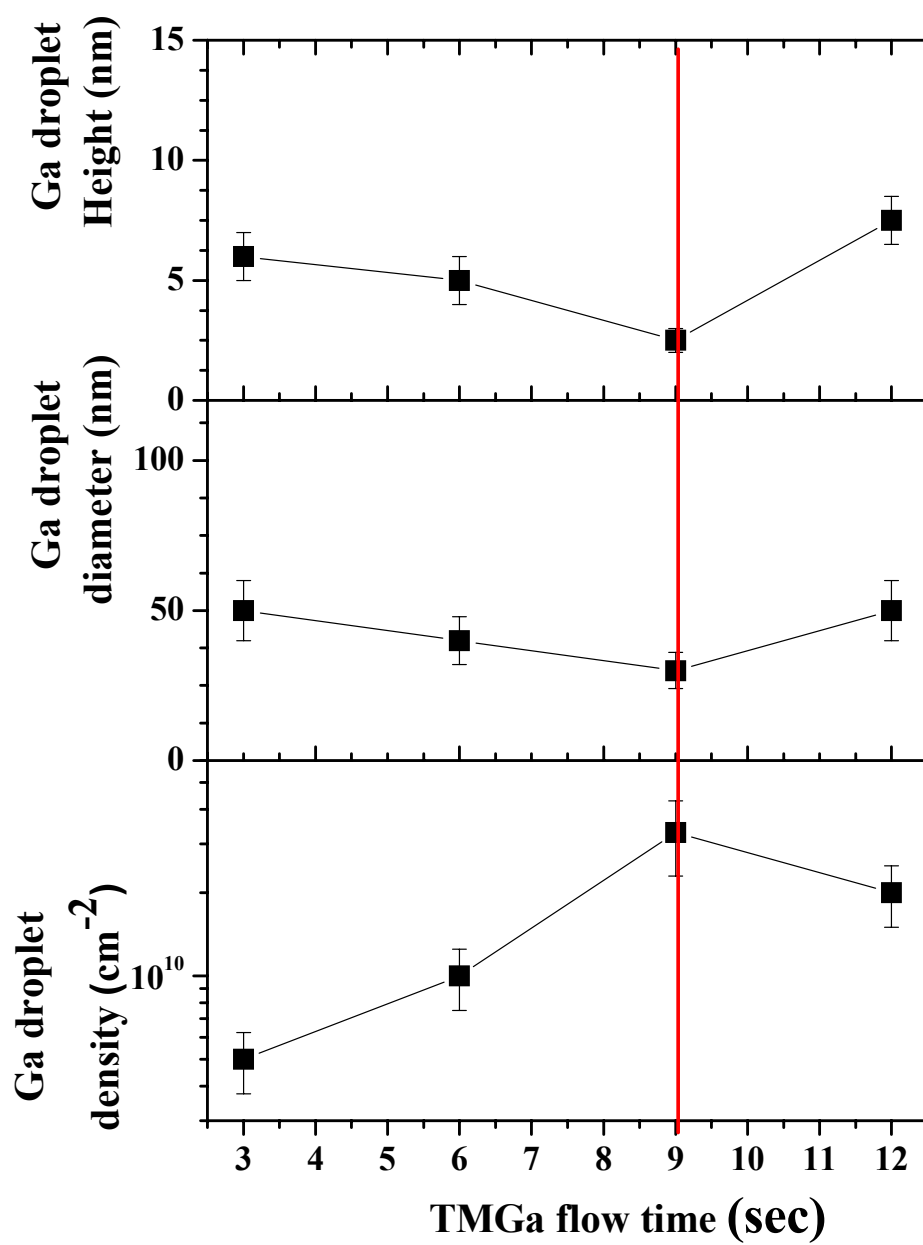
Figure 5.11 Graphs of geometric GaN nanostructure as a function of TMGa flow time.

5.5 Crystallization for GaN nanostructure

After deposition of metallic layer, NH_3 needs to be introduced to transform into GaN nanostructures. The conversion of nanoscale Ga droplets into GaN quantum dots was preformed by exposing the Ga droplets to ammonia flow immediately after the TMGa flow. Figure 5.12 shows the wafer colors with different ammonia flow times. The sample in Figure 5.12 (a) had been exposed for 1 minute, It was demonstrated that the density of Ga islands is preserved under NH_3 flow for some minutes, while the surface looks dark in the ammonia flow for less than a minutes, meaning that the metallic Ga droplets has been not completely transformed into crystalline GaN solid and even optical property of the nanostructure is poor. However, the sample in Figure 5.12 (b) had been exposed for 5 minutes, and it looks as bright as the typical 2μm-thick GaN wafer (see Figure 5.12 (c)), which means that most liquid droplets were crystallized into GaN nanostructures.

Figure 5.12 GaN nanostructure samples grown on AlGaN with ammonia exposure (a) for 1 minute and (b) 5 minutes, and (c) a normal 2um-thick GaN.

The transformation process represents interaction of several mechanisms. The first is the reaction of nitrogen with Ga nanodroplets, resulting in the formation of a supersaturated solution and consequently the crystallization of GaN at the droplet/AlGaN interface. On the other hand, the transition from nanodroplets to crystal can proceed differently when Ga adatoms have a high surface diffusion rate; the diminishing role of the surface tension as Ga droplets solidify in the absence of a high compressive strain makes it possible for the Ga atoms to diffuse out from the droplets and participate in a layer-by-layer growth [18]. Based on the notion that the kinetic barriers associated with surface diffusion can be modified by the local surface stoichiometry [19], the effect of ammonia flow during conversion was investigated in a series of preliminary experiments.

5.6 Optimization of growth conditions

Table 5.1 Optimized growth conditions for GaN nanostructure on AlGaN

Growth parameter	Optimized values
Growth temperature	820 ºC for 9 seconds
Growth pressure	300 Torr
Thermal treatment	850 ºC for 5 minutes

Table 5.1 shows that the growth conditions have been optimized through all growth processes described in this section. The TMGa source was introduced at 820 ºC for 9 seconds. The optimal Ga metallic layer thickness was estimated about 3 nm. And all of the growth were performed at 300 Torr of a optimized growth pressure. Finally, thermal treatment was performed at 850 ºC for 5 minutes for crystallization Ga liquid droplets into GaN nanostructures. Most liquid droplets were successfully transformed into GaN nanostructures and good optical property was obtained.

However, two measurements were performed on the samples grown under these optimized growth conditions as seen in Figure 5.13. AFM image shows small islands with high density (Height : 5 ~7 nm, Diameter : 30 ~ 60 nm and Density : 1.5E10 cm^{-2}) and PL measurement shows that these nanostructures were optically activated at wavelength of around 350 nm.
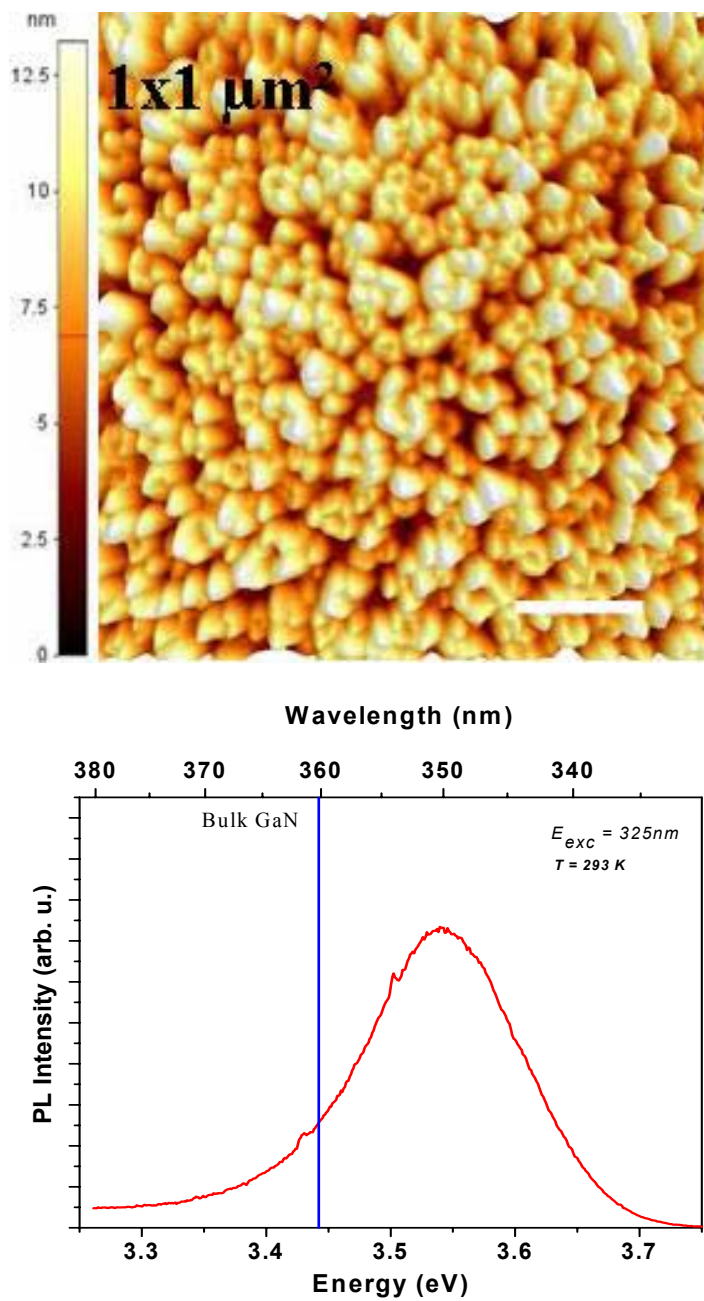
Figure 5.13 (a) AFM image and (b) PL measurement on the sample grown under the optimized growth conditions.

5.7 Comparison with GaN/AlN system

Photon energies from GaN nanostructures have compared between GaN/AlN and GaN/AlGaN systems. Figure 5.14 shows two AFM images for GaN nanostructures grown on (a) AlN and (c) AlGaN, and their photoluminescence spectra [see (b) and (d)], respectively.   The GaN nanostructures grown on AlGaN have higher energy than grown on AlN at the same dot size, because GaN/AlGaN system has less lattice mismatch (i.e. < 0.5 %) than GaN/AlN system, which results in smaller piezoelectric field effect to reduce the photon energy. This phenomenon will be explained in numerical calculation section in detail.
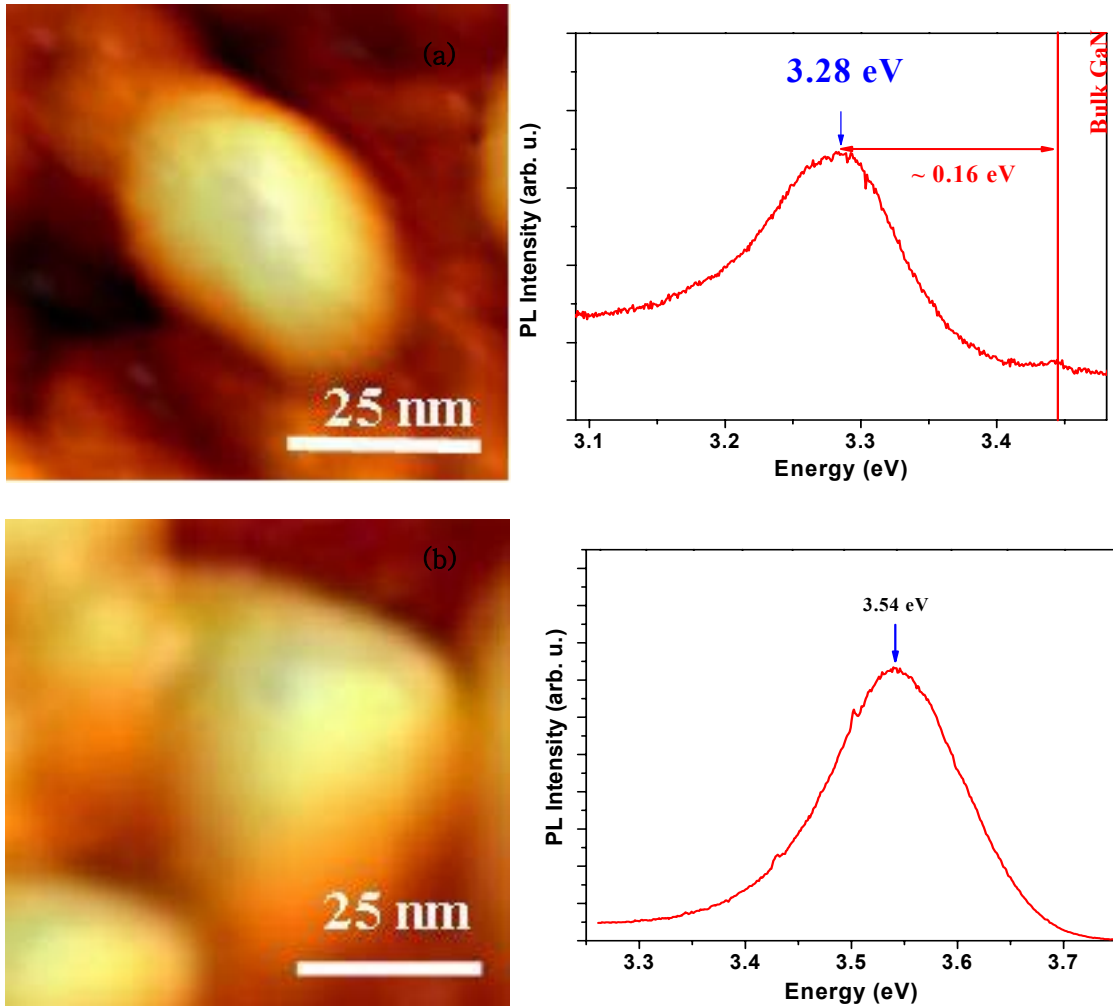
Figure 5.14 AFM images and PL measurements on GaN nanostructure / AlN and GaN nanostructure / AlGaN.

5.8 References

[1] R. Wagner and W. Ellis, Appl. Phys. Lett., 4 (1964) 89.

[2] N. Koguchi, K. Ishige, and S. Takahashi, J. Vac. Sci. Technol. B **11**, 787 (1993).

[3] K. Kawasaki, D. Yamazaki, A. Kinoshita, H. Hirayama, K. Tsutsui, and Y. Aoyagi, Appl. Phys. Lett. **79**, 2243 (2001).

[4] C.-W. Hu, A. Bell, F. A. Ponce, D. J. Smith, and I. S. T. Tsong, Appl. Phys. Lett. **81**, 3236 (2002).

[5] S. Pearton, J. Zolper, R. Shul, and F. Ren, J. Appl. Phys., 86 (1999) 1

[6] O. Ambacher, J. Phys. D, 31 (1998) 31.

[7] C.H. Chen, H. Liu, D. Steigerwald, W. Imler, C.P. Kuo, M.G. Craford, M. Ludowise, S. Lester, J. Amano, J. Electron. Mater. 25 (1996) 1004.

[8] Y. Ohba, H. Yoshida, Rie Sato, Jpn. J. Appl. Phys. 36 (1997) L1565.

[9] M. Lyutaya and T. Barnitskaya, Inorg. Mater., 9 (1973) 1052.

[10] B. Baranov, L. Dawertiz, V, Gutan, G. Jungk, H. Newmann, and H. Raidt, Phys. Statu. Solidii (a), 49 (1978) 629.

[11] C.H. Chen, H. Liu, D. Steigerwald, W. Imler, C.P. Kuo, M.G. Craford, M. Ludowise, S. Lester, J. Amano, J. Electron. Mater. 25 (1996) 1004.

[12] H. Lahreche. M. Leroux, M. Laugt, M. Valle, B. Beaumont, P. Gibart, M. Appl. Phys. 87 (2000) 235

[13] D. Rudloff et al. Appl. Phys. Lett. **82** (2003) 367

[14] C. Chen, J. Zhang, M. Gaevski, H. Wang, W. Sun, R. Q. Fareed, J. Yang, and M. Asif Khana Appl. Phys. Lett. **80** (2002) 2057

[15] M. Zinke-Allmang, L. C. Feldman, and M. H. Grabow, Surf. Sci. Rep. **16**, (1992) 377

[16] M. Harsdorff, Thin Solid Films **90**, (1982) 1.

[17] F. Family and P. Meakin, Phys. Rev. A **40**, (1989) 3836

[18] N. Koguchi, S. Takahashi, and T. Chikyow, J. Cryst. Growth **111**, (1991) 688

[19] M. Gherasimova, G. Cui, Z. Ren, J. Su, X.-L. Wang, J. Han, K. Higashimine, N. Otsuka, J. Appl. Phys. **95**, (2004) 2921

CHAPTER 6

NUMERICAL CALCULATION

6.1 Introduction

The PL wavelength for GaN nanostructures on an AlN structure is dependent both on quantum confinement and piezoelectric effect. It was observed that larger dots obtained at a higher V/III ratio resulted in a red shift. The shift to higher energies with a decrease in nanostructure size is attributed to the decrease in piezoelectric effect rather than quantum confinement. The intensity of the PL is dependent on the density of the nanostructures. A higher PL intensity is obtained with a higher density of nanostructures [1-3].
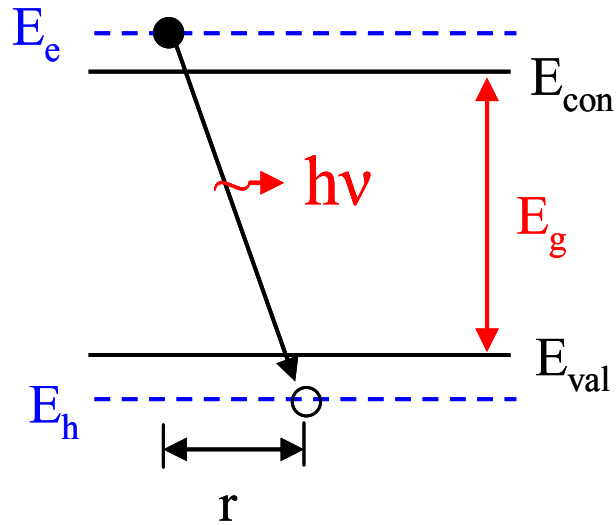
Figure 6.1 A schematic of light emission in GaN nanostructures.

A numerical approach was performed to calculate excitonic and optical properties of a GaN nanostructure system. Figure 6.1 shows a schematic for light emission from GaN nanostructures. In this chapter, ν was extracted by a numerical method to an estimated light wavelength.

$$h\,\nu = E_g + E_e + E_h + E_{col} ,\qquad\qquad (6.1)$$

where h is Planck's constant, ν is light frequency, E_g bandgap energy E_e (E_h) electron (hole) energy, and E_{col} is coulomb interaction energy between electron and hole [4-6].

6.2 Calculation of electron and hole state energies in nanostructures

In order to determine electron and hole states, the proper operator ordering in the multi-band Hamiltonians is used for an accurate description of QD heterostructures. Electron states are eigenstates of the one-band envelope-function equation:

$$\hat{H}_e \Psi_e = E_e \Psi_e,\qquad\qquad (6.2)$$

where $\hat{H}_e$, Ψ_e, and E_e are the electron Hamiltonian, the envelope wave function, and the energy, respectively. Each electron energy level is twofold degenerate with respect to spin[7,8]. The two microscopic electron wave functions corresponding to an eigenenergy E_e are

$$\psi_e = \Psi_e \,|\, S > |\uparrow >,\qquad\qquad (6.3)$$

$$\psi_e = \Psi_e \,|\, S > |\downarrow >,\qquad\qquad (6.4)$$

where $|\, S >$ is the Bloch function of the conduction band and $|\uparrow >$, $|\downarrow >$ are electron spin functions. The electron Hamiltonian $\hat{H}_e$ can be written as

$$\hat{H}_e = \hat{H}_S \, (r_e) + H_e^{(\varepsilon)} \, (r_e) + E_c \, (r_e) + eV_p \, (r_e), \qquad (6.5)$$

Where $\hat{H}_S$ is the kinetic part of the microscopic Hamiltonian unit cell averaged by the Bloch function $|\, S >$, $H_e^{(\varepsilon)}$ is the strain-dependent part of the electron Hamiltonian, E_c is the energy of unstrained conduction-band edge, e is the absolute value of electron charge, and V_p is the piezoelectronic potential.

Hole states are eigenstates of the six-band envelope function equation

$$\hat{H}_h \Psi_h = E_h \Psi_h, \qquad (6.6)$$

where $\hat{H}_h$, Ψ_h, and E_h are the hole Hamiltonian, the envelope wave function, and the energy, respectively[9,10].
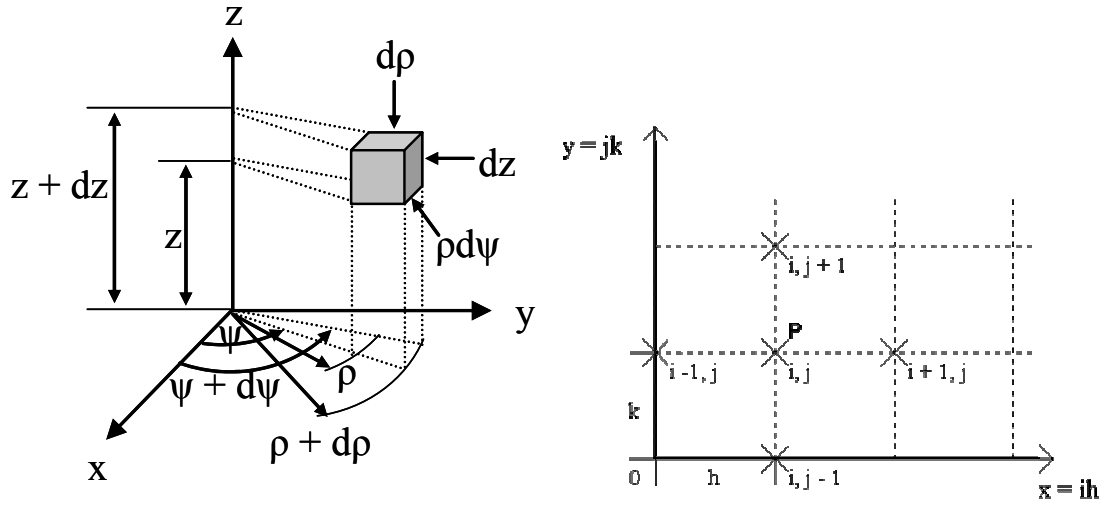
Figure 6.2 schematics of (a) cylindrical coordinated and (b) finite difference method.

However, in this work, it is assume that the shape of nanostructure is cylindrical and its barrier is infinite and the above Schrodinger equations are time-independent, i.e. stationary equation. In order to solve these equations, finite difference method (FDM) was applied as seen in Figure 6.2.

The kinetic electron Hamiltonian part in Equation (6.5) is given by

$$\hat{H}_s(r) = \frac{h^2}{2m_0}(\hat{k}_z \frac{1}{m_e^{ll}(r)}\hat{k}_z + \hat{k}_z^{\perp} \frac{1}{m_e^{\perp}(r)}\hat{k}_z^{\perp}) \tag{6.7}$$

, where m_e^{ll} and $m_e^{\perp}$ are electron effective masses and $\hat{k}_z^{\perp} = \hat{k} - \hat{k}_z$.

$$H_e^{(\varepsilon)}(r) = a_c^{ll}(r)\varepsilon_{zz}(r) + a_c^{\perp}(r)[\varepsilon_{xx}(r) + \varepsilon_{yy}(r)] \tag{6.8}$$

The hole Hamiltonian $\hat{H}_h$ can be given by

$$\hat{H}_h(r) = \begin{pmatrix} \hat{H}_{XYZ}(r_h) + H_h^{(\varepsilon)}(r_h) & 0 \\ 0 & \hat{H}_{XYZ}(r_h) + H_h^{(\varepsilon)}(r_h) \end{pmatrix} \tag{6.9}$$
$$+ E_v(r_h) + eV_p(r_h)$$

,where $\hat{H}_{XYZ}$ is a 3 × 3 matrix of the kinetic part.

The above time-independent Schrodinger equation was solved with the help of finite difference method (FDM). The detailed parts will be explained in the below subchapters [11-14]. Moreover, Table 6.1 shows the material parameters which used in this calculation.

Table 6.1 Material parameters of GaN and AlN for this calculation.

Parameter	GaN	AlN
a, nm	3.189	3.112
c, nm	5.185	4.982
E_g, eV	3.445	6.23
$m_e^{\parallel}$	0.2	0.28
$m_e^{\perp}$	0.2	0.32
C_{11}, GPa	390	396
C_{12}, GPa	145	137
C_{13}, GPa	106	108
C_{33}, GPa	398	373
C_{44}, GPa	105	116
e_{15}, C/m^2	-0.49	-0.6
e_{13}, C/m^2	-0.49	-0.6
e_{33}, C/m^2	0.73	1.46
$\varepsilon_{stat}^{\parallel}$	10.01	8.57
$\varepsilon_{stat}^{\perp}$	9.28	8.67
P_{sp}, C/m^2	-0.029	-0.081

6.3 Confinement energy

The optical properties of GaN nanostructures are affected by quantum confinement resulting in a blue shift of the nanostructure's PL emissions, which means the confinement effect moves the bandgap of GaN (3.44 eV) to higher energy. The confinement energy depends on the size as well as the shape of the nanostructures [15].

The confinement energy of the ground state for an electron (or hole) is given by

$$E_C = -\frac{h^2}{8}\left(\frac{1}{m_x d_x^2} + \frac{1}{m_y d_y^2} + \frac{1}{m_z d_z^2}\right) \tag{6.10}$$

For a disk-like dot, dx and dy are much larger than dz (height of nanostructure) that the above equation is simplified to $-h^2/8m_z d^2$. Figure 6.3 shows confinement energies of electron and hole in GaN nanostructures. For small nanostructures in size, the confinement energy is very sensitive to the dot size, this sensitivity is substantially reduced when the size increased. Quantitatively, when size decreases from 10 to 4 nm, the confinement energy of electron increases to 0.76 eV, even with dependence on the shape of the dots. The absolute value of confinement energy for a hole steeply decreases when the size decrease, because the hole is heavier than the electron [16-18].
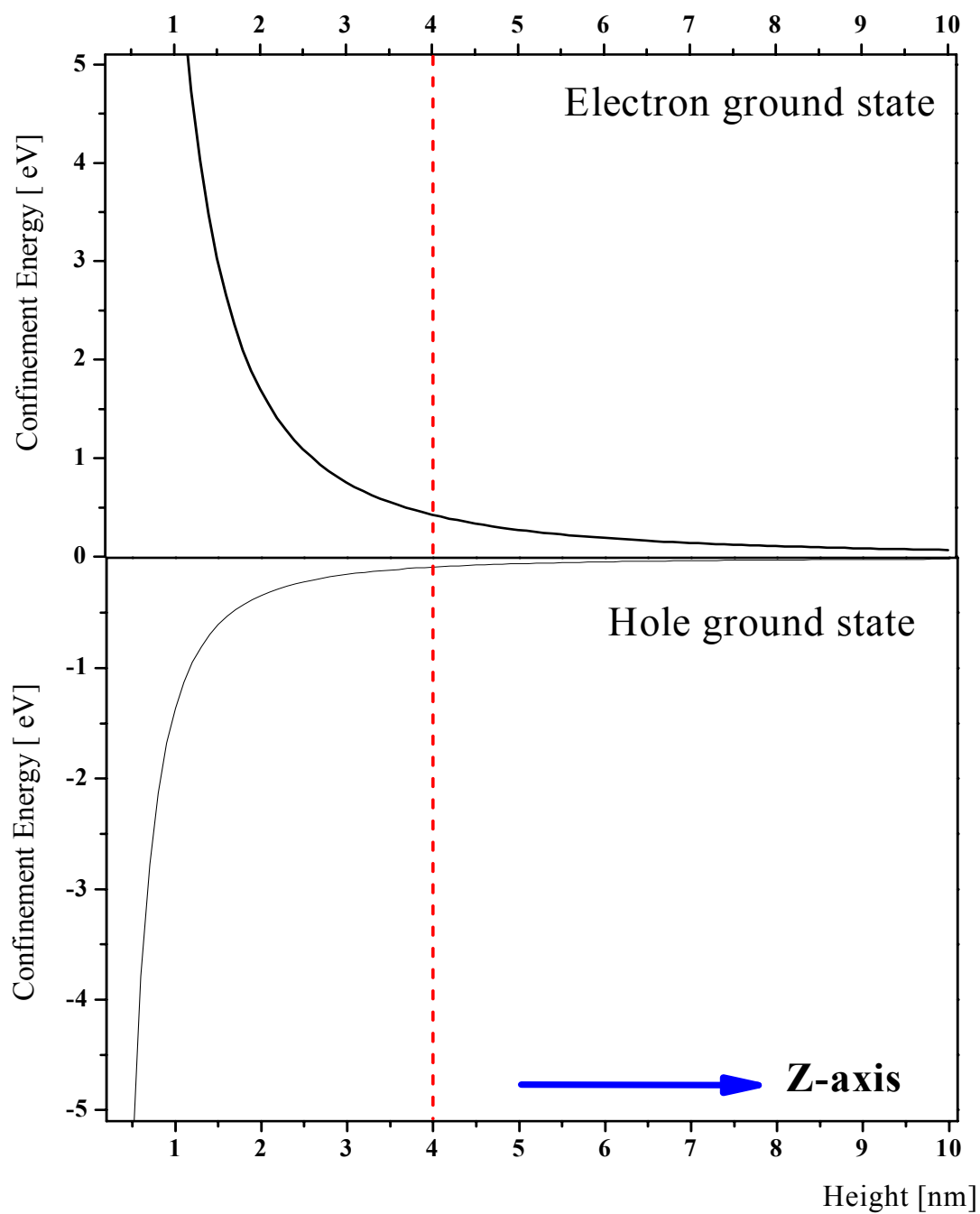
Figure 6.3 Ground state confinement energies of electron and hole.

6.4 Piezoelectric field energy

In III-nitrides, spontaneous and strain-induced polarizations generate an internal electric field (i.e. built-in electric field) making a red shift of the emitted light. The spontaneous polarization is a mechanism for spin polarizing atoms using linearly polarized light. A mechanical stress caused by lattice mismatch produces an electric field which results in the strain-induced polarization (also called piezoelectric polarization). Figure 6.4 shows a schematic of polarization for GaN grown on AlN with Ga-polarity.
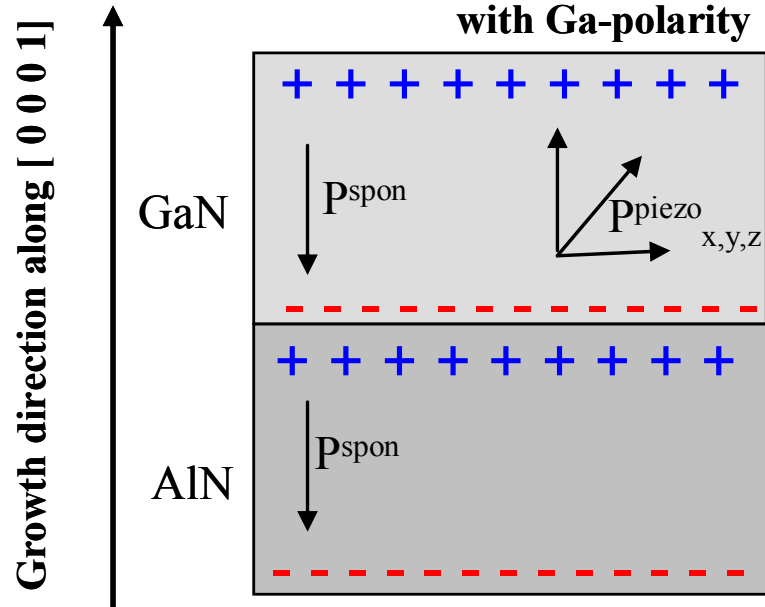
Figure 6.4 A schematic of two kinds polarizations in GaN on AlN system.

In the absence of external fields, the piezoelectric potential is determined by solving Maxwell equation Div D =0 for displacement field, D, which is defined by

$$D = \varepsilon E + P, \tag{6.11}$$

The total polarization, P, is a combination of piezoelectric polarization (P_{piezo}) and spontaneous polarization (P_{spon}), given by

$$P = P_{piezo} + P_{spon} , \qquad (6.12)$$

In the linear equilibrium system, the piezoelectric polarization is related to the strain, ε, by

$$P_i^{piezo} = \sum_{j=1}^{6} e_{ij}\varepsilon_j , \quad \text{where } e \text{ is the piezoelectric coefficient.}$$

(6.13)

In the system of GaN nanostructure / AlN, spontaneous polarization is nonzero for the z direction and its value is a specific constant for each material as seen in Table 6.1. The total polarization along each component is

$$P_x = e_{15}\,\varepsilon_{xz}$$

$$P_y = e_{15}\,\varepsilon_{yz} \qquad (6.14)$$

$$P_z = e_{31}\,(\,\varepsilon_{xx} + \varepsilon_{yy}\,) + e_{33}\,\varepsilon_{zz} + P_{spon}$$

where strain, ε_{ij} (where i or j is x, y, or z), is caused by the lattice mismatch between GaN and AlN[19-20].

The electric field for polarization computed from Div D = 0 is very strong, of the order of MV/cm. The strong electric field leads to a significant reduction of the effective band gap of GaN nanostructures and gives rise to a remarkable electron-hole spatial separation. This effect has a considerable influence on exciton states and optical properties on nanostructures. Moreover, the piezoelectric potential is maximized at the top and bottom of the nanostructures as seen in Figure 6.5. This phenomenon caused by a strong strain between the GaN and AlN interface will show the effect on the excitonic properties of GaN nanostructures [21].
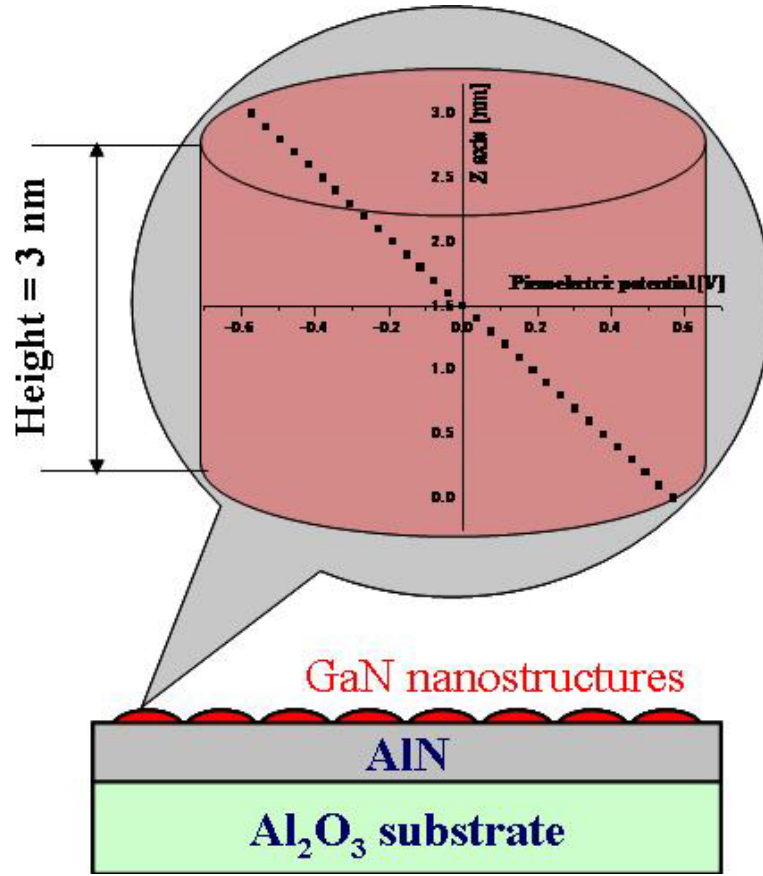
Figure 6.5 Electric polarization potential in GaN nanostructure along the z-axis.

6.5 Coulomb potential energy

The coulomb potential energy (E_{col}) of the electron-hole is given by

$$E_{col}(r) = \frac{e^2}{4\pi\varepsilon_0\varepsilon(r)\left|\vec{r}_e - \vec{r}_h\right|}$$

(6.15)

,where $\vec{r}_e$ and $\vec{r}_h$ are the electron and hole position vectors. This energy was also computed using FDM [22].
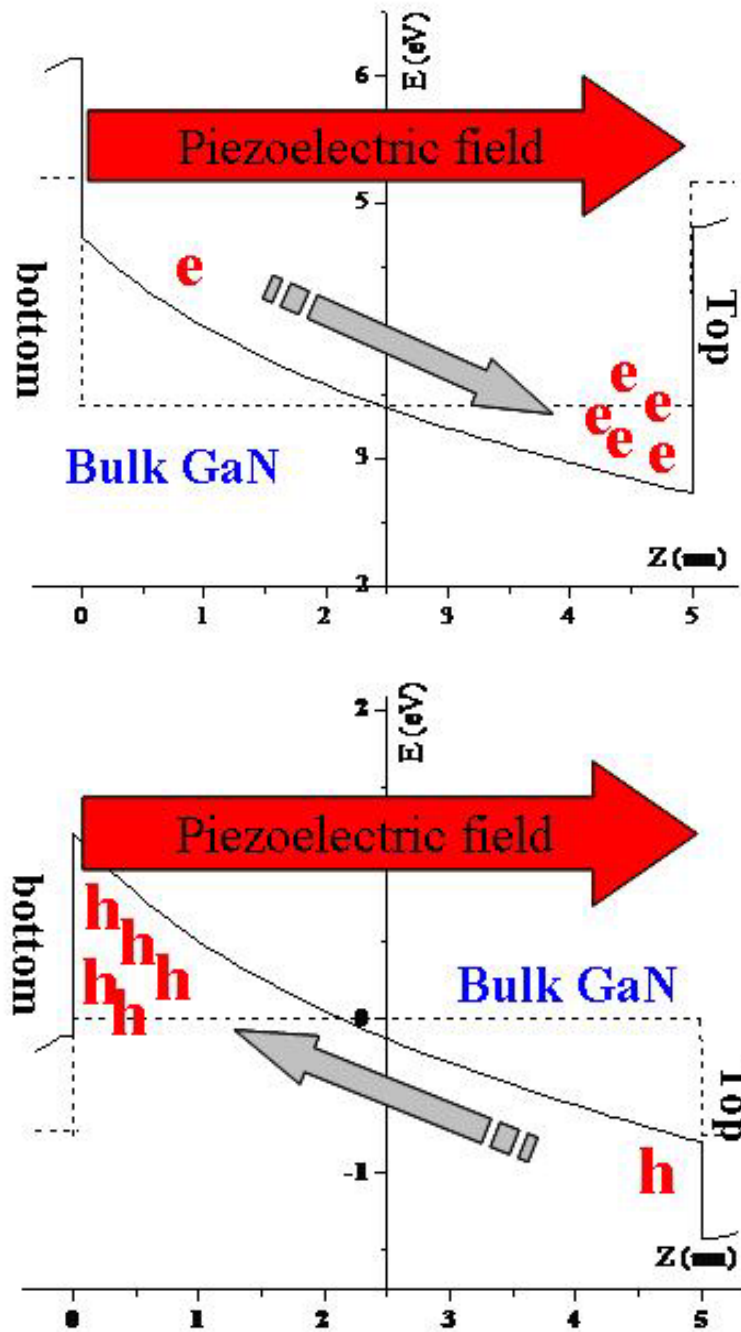
Figure 6.6 Conduction (and valence)-band edge in GaN nanostructure along the z-axis.

6.6 Calculation of exciton states and interband optical transitions

in GaN/AlN and GaN/AlGaN systems

Conduction band edge and valence band edge were calculated before adding coulomb potential. The band shapes are tilted along to the z-axis due to piezoelectric field potential between AlN and GaN as seen in Figure 6.6. This shows that electrons are willing to move to the top of the GaN nanostructure and holes flavor to be located in the bottom of the nanostructure, where the usual spontaneous polarization caused by Ga-polarity in MOCVD growth restricts these electrons and holes moving to each side [23]. However, these carrier motions affect excitonic and optical properties.

Exciton state energy has been determined from Eq. (6.1) after considering the Coulomb potential energy. Figure 6.7 (a) shows the exciton ground state energy as a function of nanostructure height. In this numerical analysis, it is found that GaN nanostructure having a height smaller than 4.1nm has a larger bandgap energy than bulk GaN, while GaN nanostructure with height > 4.1nm has a smaller bandgap energy than the bulk GaN. Thus, confinement factor and piezoelectric field factor are offset each other at around a height of 4.1 nm where it is equal to the bandgap energy of bulk GaN. However, Figure 6.7 (b) also shows exciton state energy as different nanostructure diameters from 10 to 100nm. Although the exciton energy increases as the diameter decreases, the varied amount of the exciton energy can be less important in comparison with the effect of nanostructure height. Therefore, the height in GaN nanostructure growth is a significant factor to determine excitonic properties.
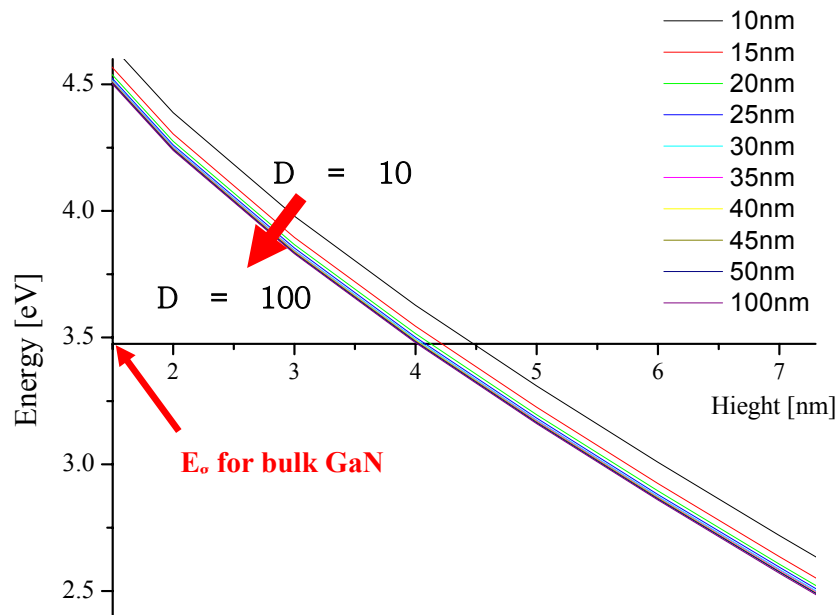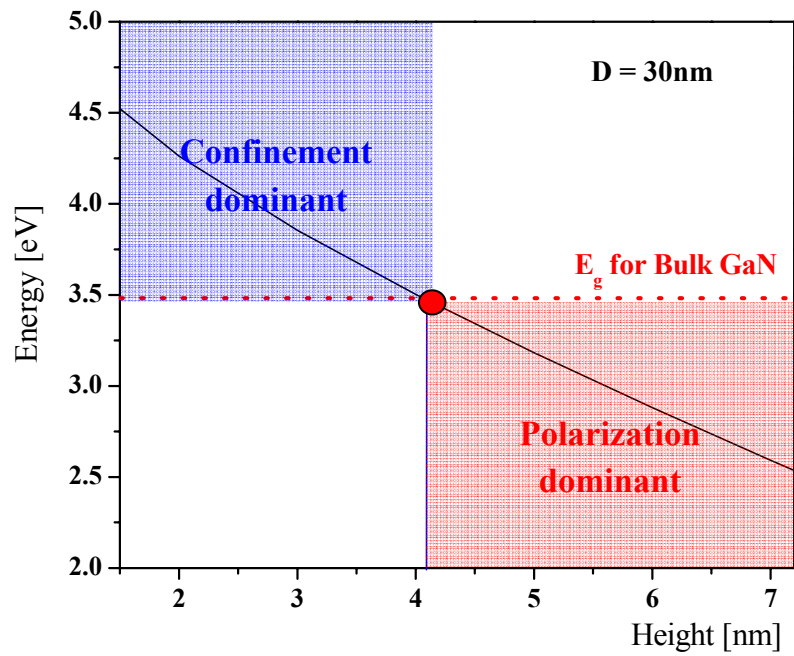
Figure 6.7 Ground state exciton energies in GaN nanostructure as function of (a) the nanostructure height and (b) diameter.
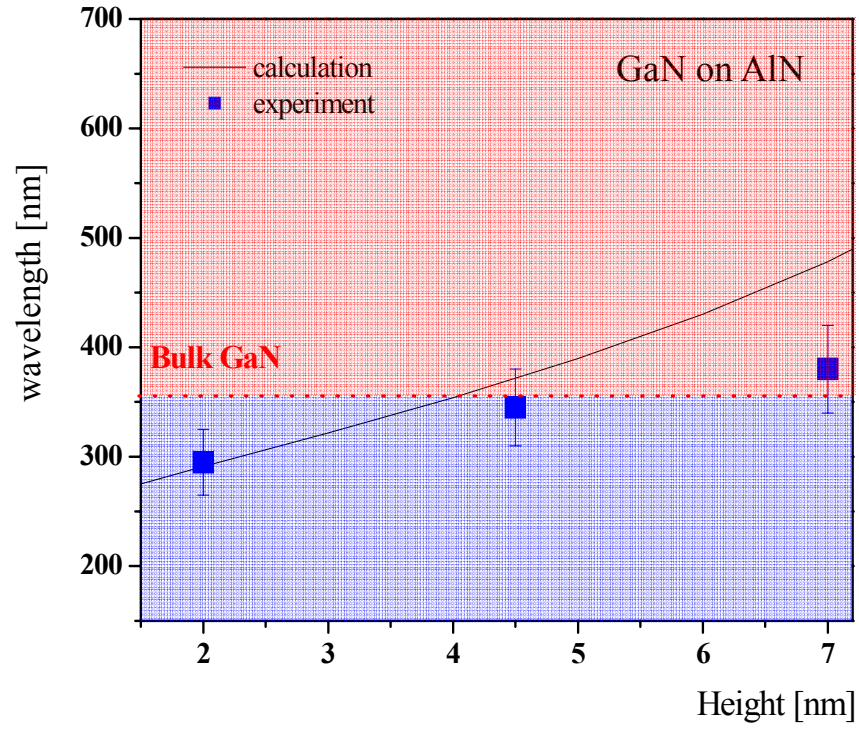
Figure 6.8 A graph to compare optical transition wavelengths between numerical
calculation and experimental data.

In Figure 6.8 (a), the experimental data are compared with the numerical calculation results, which show fairly good agreement between two data. In addition, lattice-matched system (i.e. GaN nanostructure / $Al_{0.15}Ga_{0.85}N$) was calculated. It has been found that the piezoelectric field effect is too small to reduce the exciton energy, thus the confinement energy in this system mainly determines the excitonic properties. Figure 6.8 (b) shows that the emission wavelength is closer to the wavelength of bulk GaN as the nanostructure height increases.

Table 6.2 Comparison between GaN/AlN and GaN/AlGaN systems.

Height : 3 nm Diameter : 30 nm	Lattice mismatch	Piezoelectric field	Confinement energy	Emission wavelength
GaN/AlN	.2.5 %	2.2 MV/cm	0.76 eV	322 nm
GaN/Al$_{0.15}$GaN$_{0.85}$N	< 0, 5 %	0.18 MV/cm	0.76 eV	281 nm

Moreover, numerical calculation was performed in GaN / Al$_{0.15}$Ga$_{0.85}$N system. Figure 6. 9 shows the comparison of emission wavelengths between GaN/AlN system and GaN/AlGaN system with different nanostructure height. The light emission wavelength from GaN nanostructures on AlGaN increases and gets close to the bulk GaN wavelength as the nanostructure height increases However, the wavelength is shorter than one from the GaN/AlN system, because GaN/AlGaN system has smaller lattice mismatch (i.e. < 0.5 %) than GaN/AlN, which cause less piezoelectric effect. This piezoelectric field potential results in red-shift of GaN nanostructure emission relative to excitonic emission in bulk GaN, while blue-shift is caused by confinement. Therefore, quantum confinement effect is more dominant than piezoelectric effect to determine optical transition wavelength in GaN/Al$_{0.15}$Ga$_{0.85}$N system. Table 6.2 confirms this phenomenon. For the same dot size, the emission wavelength of GaN/AlGaN system was 281 nm, but the wavelength of GaN/AlN was 322 nm, which means GaN/AlGaN system has shorter light emission wavelength.
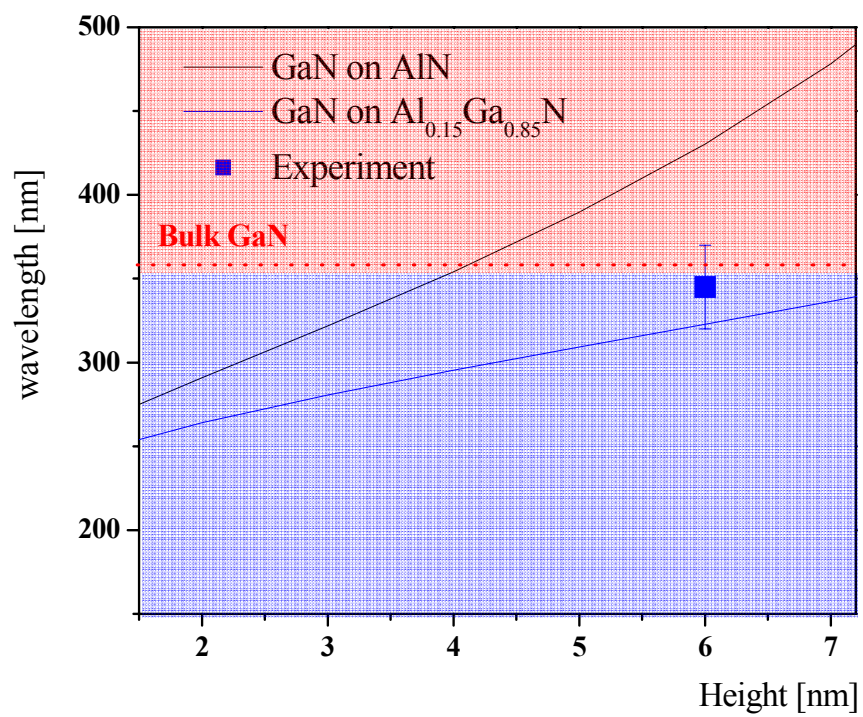
Figure 6.9 A graph to compare optical transition wavelengths between GaN/AlN
and GaN/AlGaN systems

6.7 References

[1] F. Widmann, B. Daudin, G. Feuillet, Y. Samson, J. L. Rouviere, and N. Pelekanos, J. Appl. Phys. **83**, 7618, 1998.

[2] F. Widmann, J. Simon, B. Daudin, G. Feuillet, J. L. Rouviere, N. T. Pelekanos, and G. Fishman, Phys. Rev. B **58**, R15989 1998.

[3] P. Ramval, S. Tanaka, S. Nomura, P. Riblet, and Y. Aoyagi, Appl. Phys. Lett. **73**, 1104 1998.

[4] P. Ramval, P. Riblet, S. Nomura, Y. Aoyagi, and S. Tanaka, J. Appl. Phys. **87**, 3883 , 2000.

[5] V. J. Leppert, C. J. Zhang, H. W. H. Lee, I. M. Kennedy, and S. H. Risbud, Appl. Phys. Lett. **72**, 3035, 1998.

[6] E. Borsella, M. A. Garcia, G. Mattei, C. Maurizio, P. Mazzoldi, E. Cattaruzza, F. Gonella, G. Battagin, A. Quaranta, and F. D'Acapito, J. Appl.Phys. **90**, 4467, 2001.

[7] E. Martinez-Guerrero, C. Adelmann, F. Chabuel, J. Simon, N. T. Pelekanos, G. Mula, B. Daudin, G. Feuillet, and H. Mariette, Appl. Phys. Lett.**77**, 809, 2000.

[8] B. Daudin, G. Feuillet, H. Mariette, G. Mula, N. Pelekanos, E. Molva, J. L. Rouviere, C. Adelmann, E. Martinez-Guerrero, J. Barjon, F. Chabuel, B. Bataillou, and J. Simon, Jpn. J. Appl. Phys., Part 1 **40**, 1892, 2001.

[9] A. D. Andreev and E. P. O'Reilly, Phys. Rev. B **62**, 15851, 2000.

[10] V. A. Fonoberov, E. P. Pokatilov, and A. A. Balandin, J. Nanosci. Nanotechnol. **3**, 253, 2003.

[11] L. D. Landau and E. M. Lifshitz, *Theory of Elasticity*, 3rd ed. ~Pergamon, Oxford, U.K., 1986.

[12] I. P. Ipatova, V. G. Malyshkin, and V. A. Shchukin, J. Appl. Phys. **74**, 7198, 1993.

[13] I. Vurgaftman, J. R. Meyer, and L. R. Ram-Mohan, J. Appl. Phys. **89**, 5815, 2001.

[14] K. Shimada, T. Sota, and K. Suzuki, J. Appl. Phys. **84**, 4951, 1998.

[15]M. E. Levinshtein, S. L. Rumyantsev, and M. S. Shur, *Properties of Advanced Semiconductor Materials: GaN, AlN, InN, BN, SiC, and SiGe* , New York 2001.

[16] E. Ejder, Phys. Status Solidi A **6**, 445, 1971.

[17] F. Bernardini, V. Fiorentini, and D. Vanderbilt, Phys. Rev. B **56**, R10024, 1997.

[18] S. M. Komirenko, K. W. Kim, M. A. Stroscio, and M. Dutta, Phys. Rev. B **59**, 5013, 1999.

[19] E. P. Pokatilov, V. A. Fonoberov, V. M. Fomin, and J. T. Devreese, Phys. Rev. B **64**, 245328, 2001.

[20] F. Mireles and S. E. Ulloa, Phys. Rev. B **62**, 2562, 2000.

[21] C. Pryor, M. E. Pistol, and L. Samuelson, Phys. Rev. B **56**, 10404, 1997.

[22] V. A. Fonoberov, E. P. Pokatilov, and A. Balandin, Phys. Rev. B **66**, 085310, 2002

[23] G. W. Hooft, W. A. Poel, L. W. Molenkamp, and C. T. Foxon, Phys. Rev. B **35**, 8281, 1987.

Chapter 7

FERROMAGNETIC NANOSTRUCTURES

7.1 Introduction of diluted magnetic semiconductors

Since the studies of ferromagnetic properties in diluted magnetic semiconductors (DMSs) such as Mn-doped InAs or GaAs, the spin degree of freedom in DMSs has been attractive for a new functional semiconductor as spintronics devices [1,2]. Either adding the spin degree of freedom to conventional charge-based electronic devices or using the spin alone has the potential advantages which are non-volatility, higher data processing speed, lower electric power consumption, and higher integration densities compared with conventional semiconductor devices. However, the ferromagnetic transition temperature (Curie temperature: T_C) is as high as 110 K in 5% Mn-doped GaAs [3], therefore, there has been strong encouragement to produce a ferromagnetic DMS operating above room temperature. For a successful fabrication of room temperature ferromagnetic DMSs, it is important to identify he origin of the ferromagnetism in DMSs.

Mn is a typical magnetic material for semiconductor-based spin-electronics (i.e. spintronics). The semiconductor with a small amount of Mn incorporated has a ferromagnetic behavior and remarkable magneto-optical property. Ferromagnetic semiconductors based on both the II-VI systems (CdMnTe and ZnMnTe) [4, 5] and the III-V systems (GaMnAs and InMnAs) have been produced. But these systems have lower Curie temperature than room temperature. One group had studied for this problem and

they reported GaN and ZnO which are promising host materials to realize the room temperature ferromagnetic semiconductors [6] as shown in Figure 7.1. In MOCVD system, bis-cyclopentyldienyl manganese (Cp_2Mn) is used as a Mn precursor. The GaMnN epitaxial layer is grown at the normal GaN growth temperature.
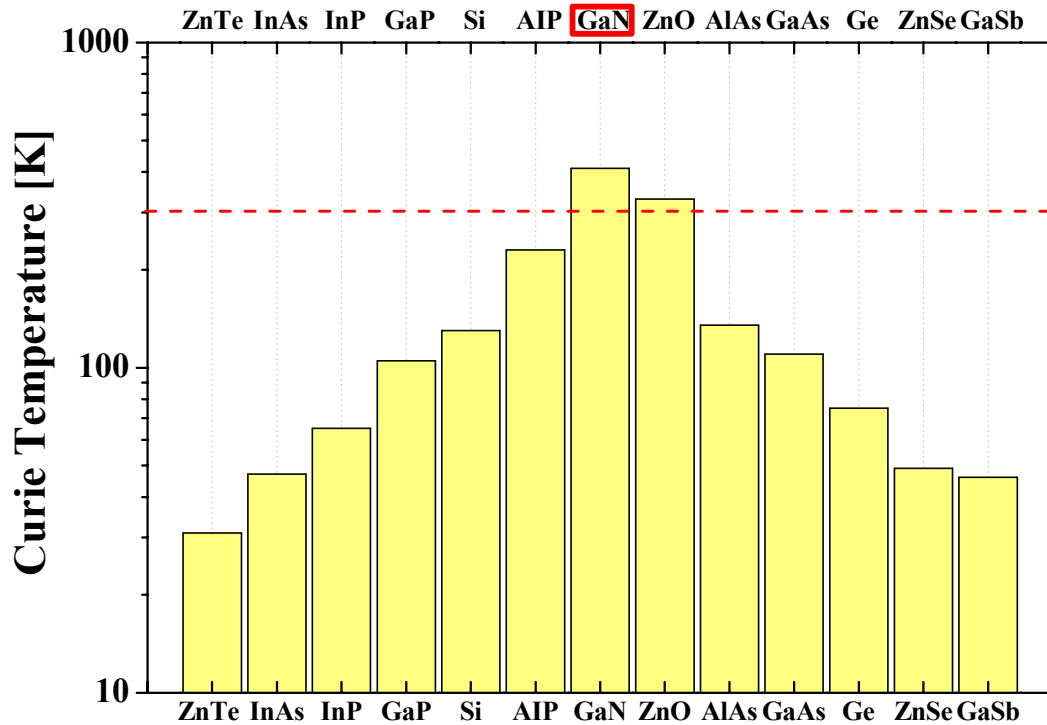
Figure 7.1 Curie Temperature T_c for various p-type semiconductors containing 5% of Mn.

The properties of ferromagnetism are influenced by both effects of quantum mechanics: spin and the Pauli exclusion principle. The spin of an electron, combined with its orbital angular momentum, results in a magnetic dipole moment and creates a magnetic field. In many materials, however, the total dipole moment of all the electrons is

zero (e.g. the spins are in up/down pairs). Only atoms with partially filled shells (e.g. unpaired spins) can experience a net magnetic moment in the absence of an external field. A ferromagnetic material has many such electrons, and if they are aligned they create a field. However, if it is placed in a strong enough external magnetic field, the domains will reorient in parallel with that field, and will remain aligned when the field disappears, thus forming a permanent magnet. This magnetization as a function of the external field is described by a hysteresis curve as shown in Figure 7.2 [7].

Figure 7.2 Hysteresis loop to plot the magnetization (M) as a function of the magnetic field strength (H).

7.1.1 Applications for spintronics

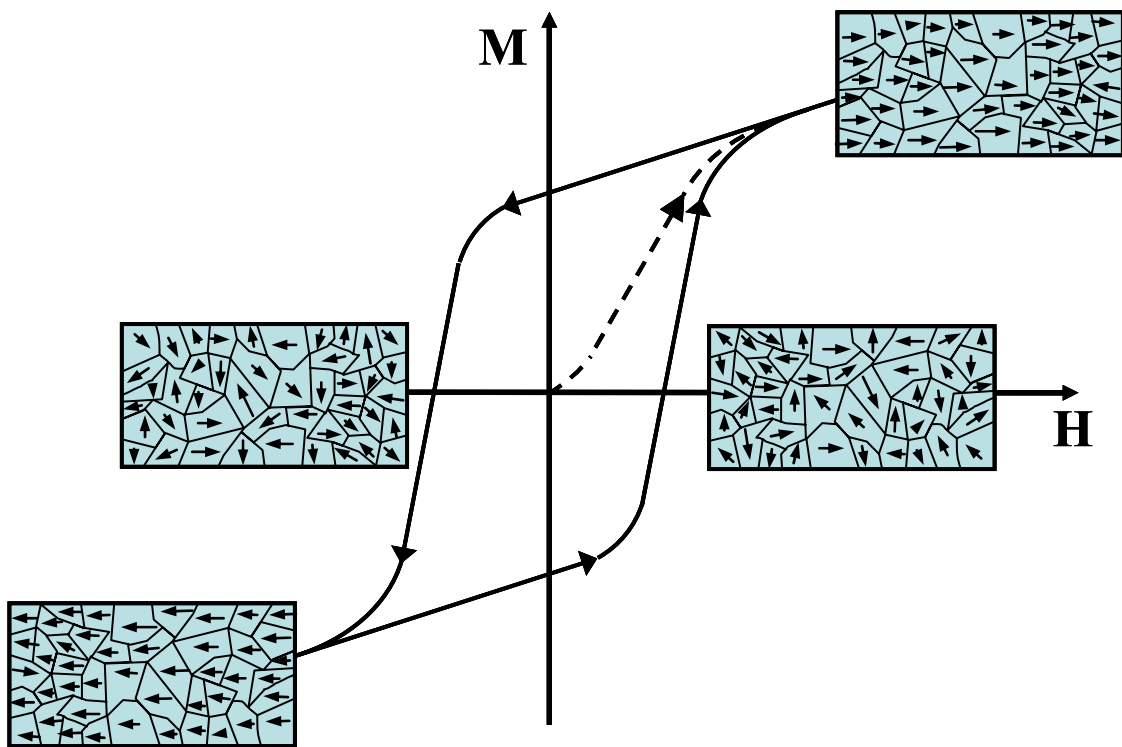The common spintronic devices are spin-junction diodes and solar cells, optical isolators and electrically controlled ferromagnets [8–12]. Moreover, light-emitting diodes with a degree of polarized output have been used to measure spin injection efficiency in heterostructures. In spite of the advantages of non-volatility, higher integration densities, lower power operation and higher switching speeds in spin-based devices, there are many factors still to consider in whether any of these can be realized. One of issues is whether the signal sizes due to spin effects are large enough at room temperature to justify the extra development work needed to make spintronic devices. And another issue is whether the expected functionality will possibly be materialized.

Figure 7.3 shows a projected technology tree for semiconductor spintronics. The basic idea of semiconductor based on spintronics is to add the characteristics of magnetic devices to existing devices such as light-emitting diodes and field effect transistors. There are many different examples for spintronics based on magnetic multi-layers, including hard drives for personal computers and non-volatile magnetic random access memories. This would lead to technologies such as microprocessor integrated on the same chip, magnetic devices integrated sensors with on-chip signal processing and off-chip optical communications. Moreover, there may also be a use for spins in semiconductor quantum dots or wells in realizing a practical quantum computer. In a so-called spin qubit, the electron spin is used as a quantum bit, i.e. a bit that can exist as a superposition of a pure '0' state and a pure '1' state.
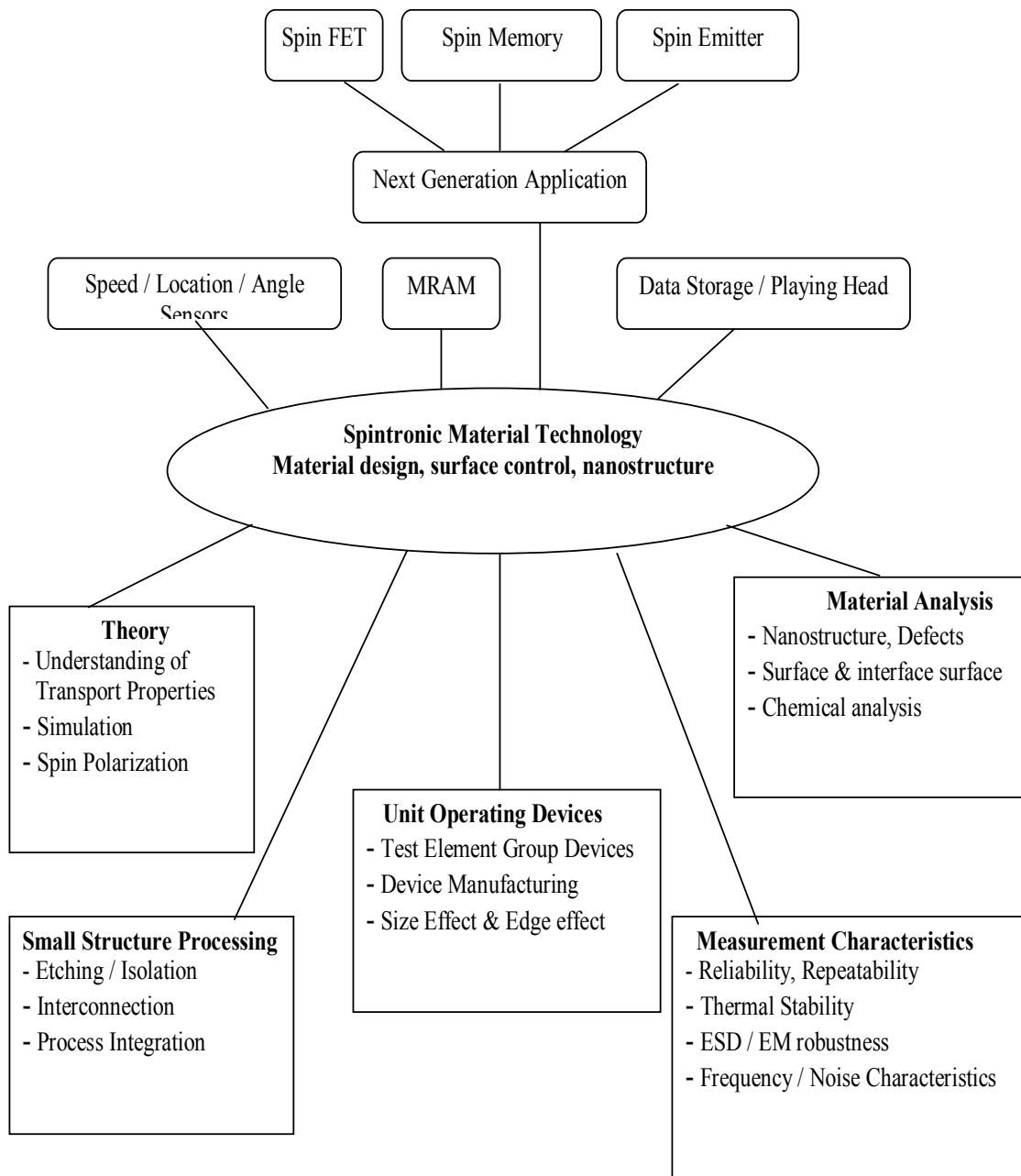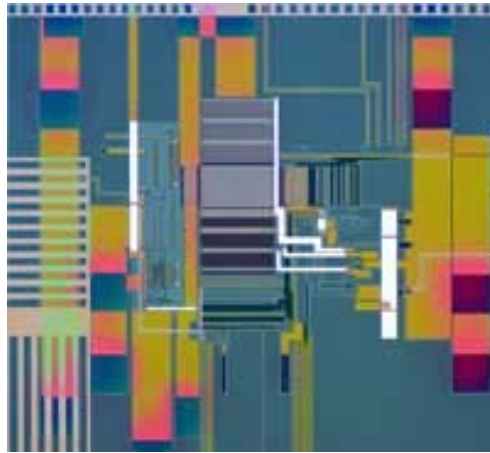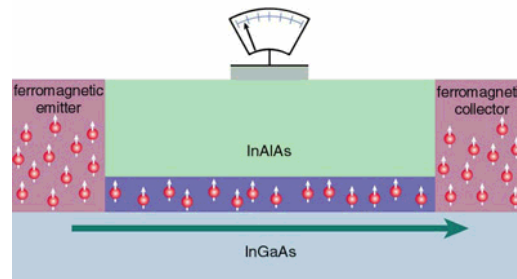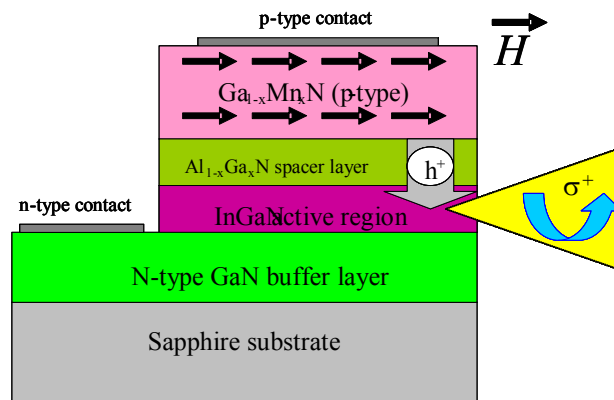
Figure 7.3 Projected technology tree for semiconductor spintronics.

(a)

(b)

(c)

Figure 7.4 Examples of applications for spintronics (a) Nonvolatile memory
(b) Spin-based logic and computation (c) Spin emitters.

The lack of available energy states inhibits both elastic spin flip and inelastic phonon scattering mechanisms, resulting in long spin relaxation times [15-17]. This property is a critical requirement for the operation of various spin-based devices proposed, and makes nanostructures very attractive for the design and development of semiconductor spintronic devices and certain implementations of quantum information technology. Therefore, electrical injection of spin-polarized carriers into nanostructures is an important requirement that would impact a spectrum of future electronic and optical device applications.

One of the suggested prototype spin devices is the so-called spin FET. A possible embodiment is illustrated in Figure 7.4. In this device, carriers are injected from a magnetized source contact (which can be either a ferromagnetic metal or a dilute magnetic semiconductor) through a channel to be collected at a drain contact that is magnetically aligned with the source contact. Without any bias voltage applied to the gate, the polarized carriers are collected at the drain contact. This is the same mechanism of operation as in a conventional charge controlled FET. In a spin FET, application of a relatively low gate voltage causes an interaction between the electric field and the spin precession of the carriers. If this is sufficient to put the spin orientation of the carriers out of alignment with the drain contact, then the current is effectively shut off and this can occur at much lower biases than is needed to shut off the current in a charge-controlled FET. Figure 7.4 show a schematic of a Si-based spin FET, in which carriers are injected into a Si channel FET from ferromagnetic GaMnP. The GaP is almost lattice-matched to Si.

In combination of spintronics with optoelectronic application, the most common way seems to be the concept of a light emitting diode (LED) with one of the contact layers made ferromagnetic by incorporation of transition metal impurities, a so-called spin LED [9]. This spin LED can adjust the polarization of the emitted light with an external magnetic field.

The spin LED can be achieved by implanting Mn into the top contact p-GaN layer of the standard InGaN MQW LED [10]. The electrical and luminescent properties of such devices show that they do produce electroluminescence but, due to the difficulty in annealing out all radiation defects, the series resistance and the turn-on voltage of such spin LEDs are very much higher than for ordinary LEDs and the electroluminescence intensity EL is lower. GaMnN layers produced by MBE have a lower density of defects and may be better suited for spin LEDs [11]. One of the problems with the latter approach is that the MBE-grown GaMnN films with high Curie temperature have n-type conductivity. Therefore, to incorporate such layers into the GaN-based LEDs one has to reverse the usual order of layers and grow a LED structure with the contact n-layer up. It was shown that problems, such as higher series resistance due to lower lateral conductivity of p-GaN compared to n-GaN, are inherent to these inverted diodes. Also it was shown that it is more difficult to attain a high quality of the GaN/InGaN multi-quantum-well active region when growing it on top of a very heavily Mg-doped p-GaN layer. Incorporation of Mn into the top contact layer also produced a relatively high resistivity of the GaMnN and a poorer quality of the ohmic contact. In addition, the ferromagnetism in GaMnN is found to be unstable against the type of high temperature $(900 \ ^{\circ}C)$ anneals used to minimize contact resistance.

However, the mean-field models consider the ferromagnetism to be mediated by delocalized or weakly localized holes in the p-type materials. The magnetic Mn ion provides a localized spin and acts as an acceptor in most III–V semiconductors so that it can also provide holes. In these models, the T_C is proportional to the density of Mn ions and the hole density. Many aspects of the experimental data can be explained by the basic mean-field model. However, ferromagnetism has been observed in samples that have very low hole concentrations, in insulating material and, more recently, in n-type material. More work is also needed to establish the energy levels of the Mn, whether there are more effective magnetic dopant atoms and how the magnetic properties are influenced by carrier density and type [13]. Even basic measurements, such as how the magnetism changes with carrier density or type and how the bandgap changes with Mn concentration in GaN, have not been performed. There is a strong need for a practical device demonstration showing spin functionality in a nitride-based structure, such as spin LED or tunneling magnetoresistance device. The control of spin injection and manipulation of spin transport by external means, such as voltage from a gate contact or magnetic fields from adjacent current lines or ferromagnetic contacts, is at the heart of whether spintronics can be exploited in device structures and these areas are still in their infancy.

7.2 GaMnN nanostructures

Mn as a ferromagnetic material introduces magnetic moments as well as holes due to its acceptor nature. Therefore introduced holes mediate ferromagnetic interaction and make the resulting ferromagnetic alloys [14-17].

7.2.1 Manganese Incorporation

The nucleation studies were performed using a highly modified GaN MOCVD tool with a vertical injection system into a short jar confine inlet design. Trimethylgallium and trimethylaluminum were used as group III sources. Ammonia was used as a group V source, and bis-cyclopentyldienyl manganese (Cp_2Mn) was used as the manganese source.

In order to achieve multifunctional nanostructures combining the advantages of QDs and diluted magnetic semiconductors, initial nucleation studies on Ferromagnetic nanostructures grown on AlN epilayers were performed. Controlling incorporation of transition metal ions in these nanostructures will enable control of their magnetic and magneto-optical properties. Ferromagnetic nanostructures were grown by introducing Mn (or Fe) during GaN flows under optimal conditions formation of nanostructures as seen in Figure 7.5 The optimal growth conditions were 800 ºC of growth temperature, 150 of V/III ratio and 100 Torr of growth pressure. In this ferromagnetic nanostructure growth, pre-growth and post-growth treatments were not performed.
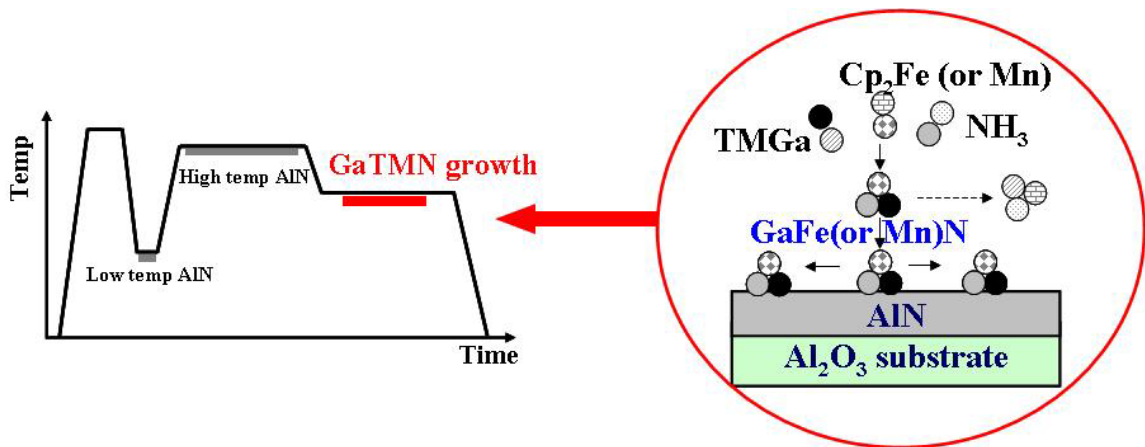

Figure 7.5 Growth processes of ferromagnetic nanostructure with temperature variation.

7.2.2 Surface morphology

The surface morphology was strongly affected by the existence of Mn atoms, as shown in Figure 7.6. The AFM characterization revealed a decrease in the lateral dimension to 30 nm and a height of 2 nm with Mn incorporation, and island density increased to 3.00×10^{10} cm^{-2}. Mn incorporation makes larger lattice mismatch between GaMnN and AlN and change film surface free energy, which results in 3D growth even without Antisurfactant.
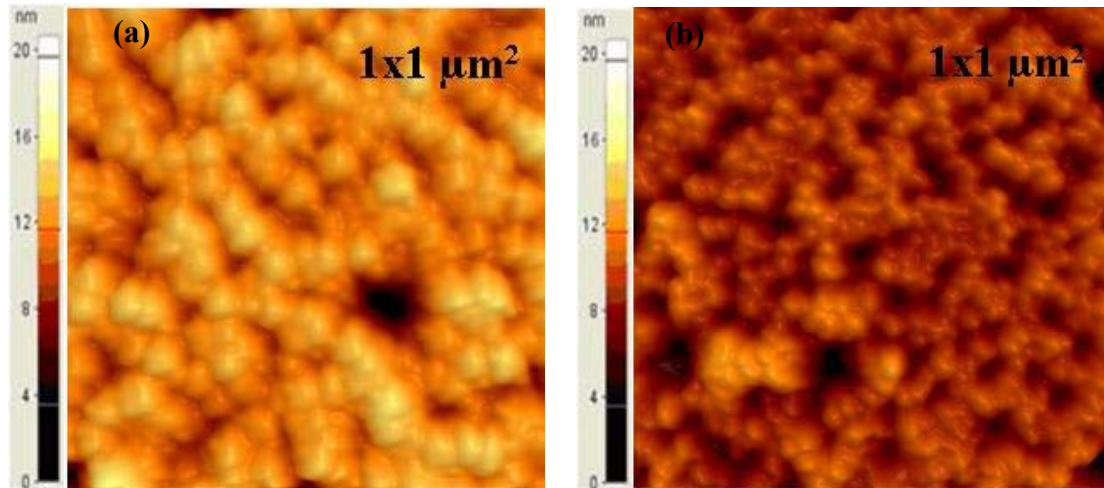

Figure 7.6 AFM images of GaN nanostructures on AlN with different Mn concentrations (a) 1 % and (b) 2 %.

Unlike GaN nanostructures, no annealing step was necessary to provide small nanostructures of high density. In addition, the activation temperatures for the formation of nanostructures are significantly reduced, and above 880°C ripening processes lead to

islands of infinite size reflected by increased island dimensions and smaller island densities (see Figure 7.7). At this point, it can be speculated that the increase in the metal concentration (decrease in the V/III ratio) and/or the role of Mn in enhancing nucleation are responsible for the observed nucleation behavior of GaMnN nanostructures.
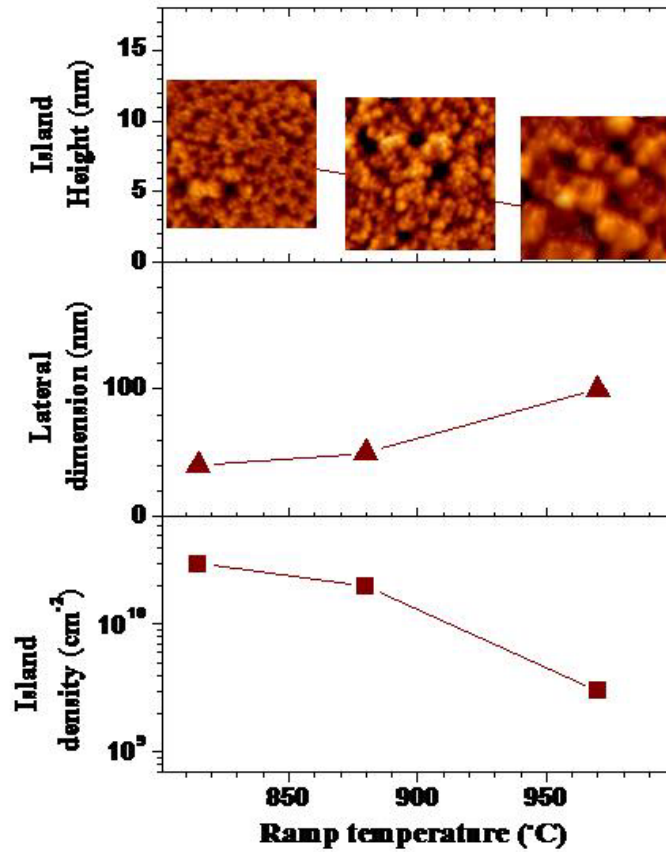

Figure 7.7 Graphs of geometric nanostructure size and density as a function of thermal treatment temperatures.

7.2.3 Ferromagnetism in nanostructures

Magnetization measurement was performed on the GaMnN nanostructures (Mn = 2 %) grown under the optimal growth conditions. Figure 7.8 shows the magnetization

measurement. A magnetic hysteresis loop was observed in this measurement, which gives an evidence for ferromagnetism of GaMnN nanostructures. But this ferromagnetism was obtained at low temperatures, rather than room temperature. During the GaMnN deposition, Mn may degrade the crystalline quality and local spin carrier exchanges. However, room temperature ferromagnetism was still desired, and so Fe was utilized as an alternative spintronic material.
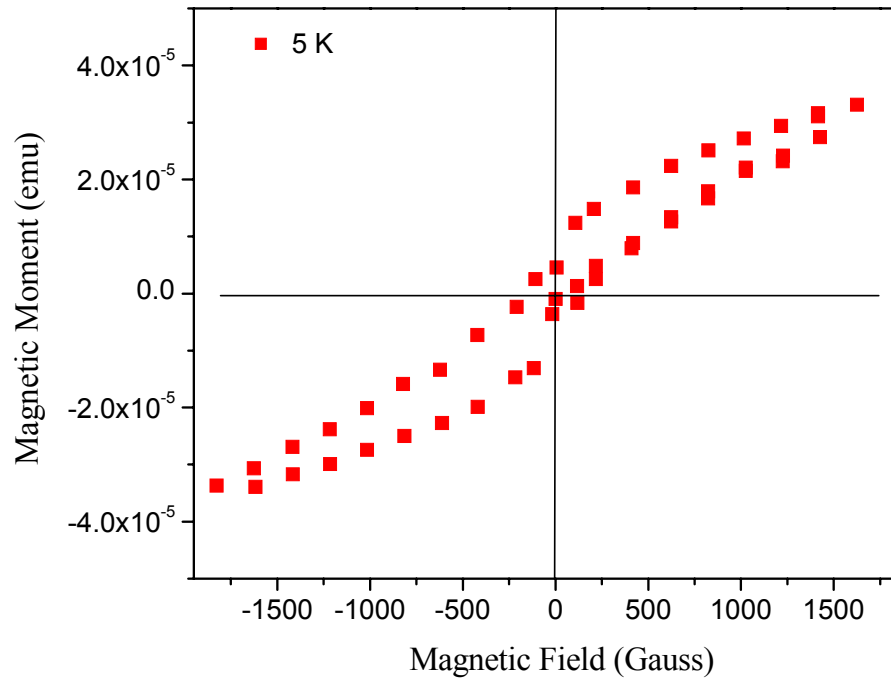

Figure 7.8 Magnetization measurement on GaMnN at low temperature.

7.3 GaFeN nanostructures

7.3.1. Optimization of growth conditions and surface morphology

This work based on GaN/AlN hetero-system with 2.5% lattice mismatch has

been performed using a highly modified MOCVD tool with a vertical injection system into a short jar confine inlet design. Trimethyl gallium (TMGa), trimethyl aluminum (TMAl), and ammonia (NH_3) were used as the source precursors for Ga, Al, and N, respectively. (Cp_2Fe) was used as the iron-doping source. After deposition of an AlN layer on a sapphire (0001) substrate, undoped or Fe doped GaN nanostructures were grown.

A 0.7 μm-thick-AlN layer was grown at 1100 °C on top of a low-temperature (LT) AlN nucleation layer at 550 °C. During growth of the AlN layer, the V/III ratio was around 1000 with H_2 and N_2 carrier gases. AFM measurement on the surface of the AlN layer provided surface roughness of less than 1 nm, which means that its surface was smooth enough to grow GaN nanostructure in the following. In addition, rocking curve (Ω) scans of XRD confirmed that the AlN layer also had good crystalline quality. The nucleation studies of undoped GaN nanostructures were first performed. During growth of typical undoped GaN nanostructures, growth temperature was around 800 °C under a 150 of V/III ratio. Growth pressure was optimized at 100 Torr. Optimization of these growth conditions was obtained using AFM measurements. The average lateral dimension and density of these nanostructures were less than 50 nm and up to 10^{10} cm^{-2} respectively.
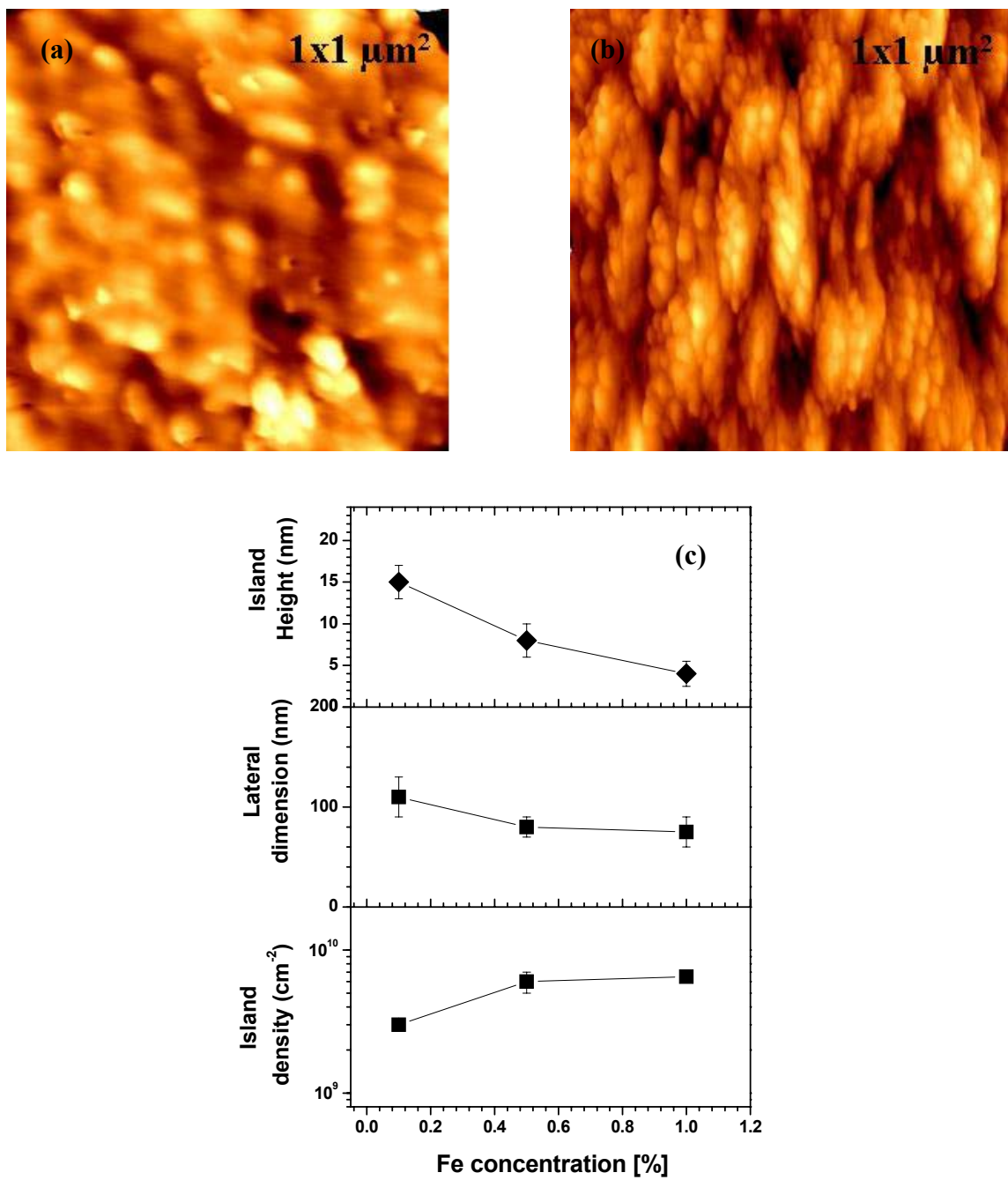
Figure 7.9 AFM images of GaN nanostructures with (a) Cp₂Fe flux of 4 μmol/min and (b) Cp₂Fe flux of 12 μmol/min (c) graphs of nanostructure size and density as a function of Cp₂Fe flux.

As in results of Mn incorporated into GaN nanostructure[18], Fe also enhances nucleation of GaN islands like an anti-surfactant. The surface morphology was strongly affected by the existence of Fe atoms, as shown in Figure 7.9. The AFM characterization revealed a decrease in the lateral dimension to 30 nm and a height of 5 nm with 3% Fe incorporation, and island density increased to about 1×10^{10} cm^{-2}. The 2.5% lattice mismatch of GaN/AlN system is not considerably large to utilize Stanski-Krastanow growth mode[19,20] for self-organized quantum dots, but transition metals can employ the surface kinetics of benefit to form islands on even lattice matched system   The presence of Fe leads to suppress adatoms migration due to altering surface free energy [21,22] and enhances island formation. Therefore, it can be speculated that the increase in concentration of this transition metal is responsible for the observed nucleation behavior of GaFeN nanostructures.

7.3.2 Room temperature ferromagnetism in nanostructures

The Mn dopant in GaN has been investigated thoroughly, as it was expected to act as an acceptor providing besides the S = 5/2 spin also the high hole concentration necessary to mediate the exchange coupling among the Mn ions. More recently it has been shown, however, that unlike Mn in GaAs the 3+/2+ acceptor level of Mn in GaN is deep (1.7 eV above the valence band edge) and the hole is localized on Mn [23, 24]. Hence, Zener magnetism is not expected for the GaN:Mn system. In this respect, the GaN:Fe system seems to be more promising, especially with p-type codoping.
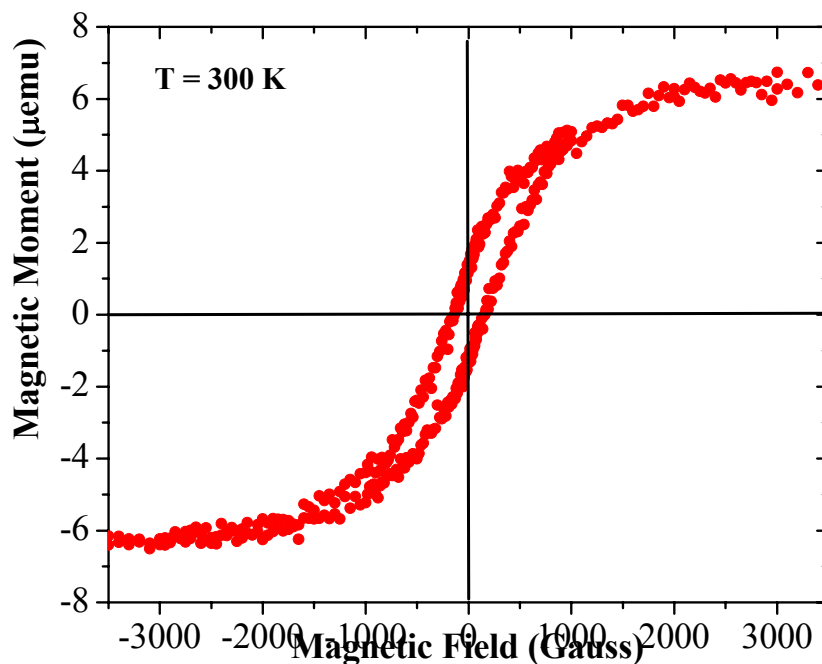
Figure 7.10 Magnetization loops at the room temperature for GaN:Fe nanostructures with different Cp$_2$Fe fluxes

For GaN:Fe nanostructure growth, up to 12 μmol/min Cp$_2$Fe was introduced into GaN nanostructures under the same growth conditions accomplished from undoped GaN nanostructure growths. All samples for magnetization measurements had a 30-nm-thick AlN cap layer. Magnetization of GaN:Fe nanostructures has been revealed by VSM measurements at room temperature. As seen in Figure 7.10, the magnetization measurements show hysteresis loops of GaN:Fe nanostructures with different Fe doping levels at 293 K. The saturation magnetization increased from 5.3 μemu/cm^3 to 6.7 μemu/cm^3 and the coercivity increased from 7.7 Oe to 146.21 Oe as Cp$_2$Fe flux increased from 8 to 12 μmol/min.

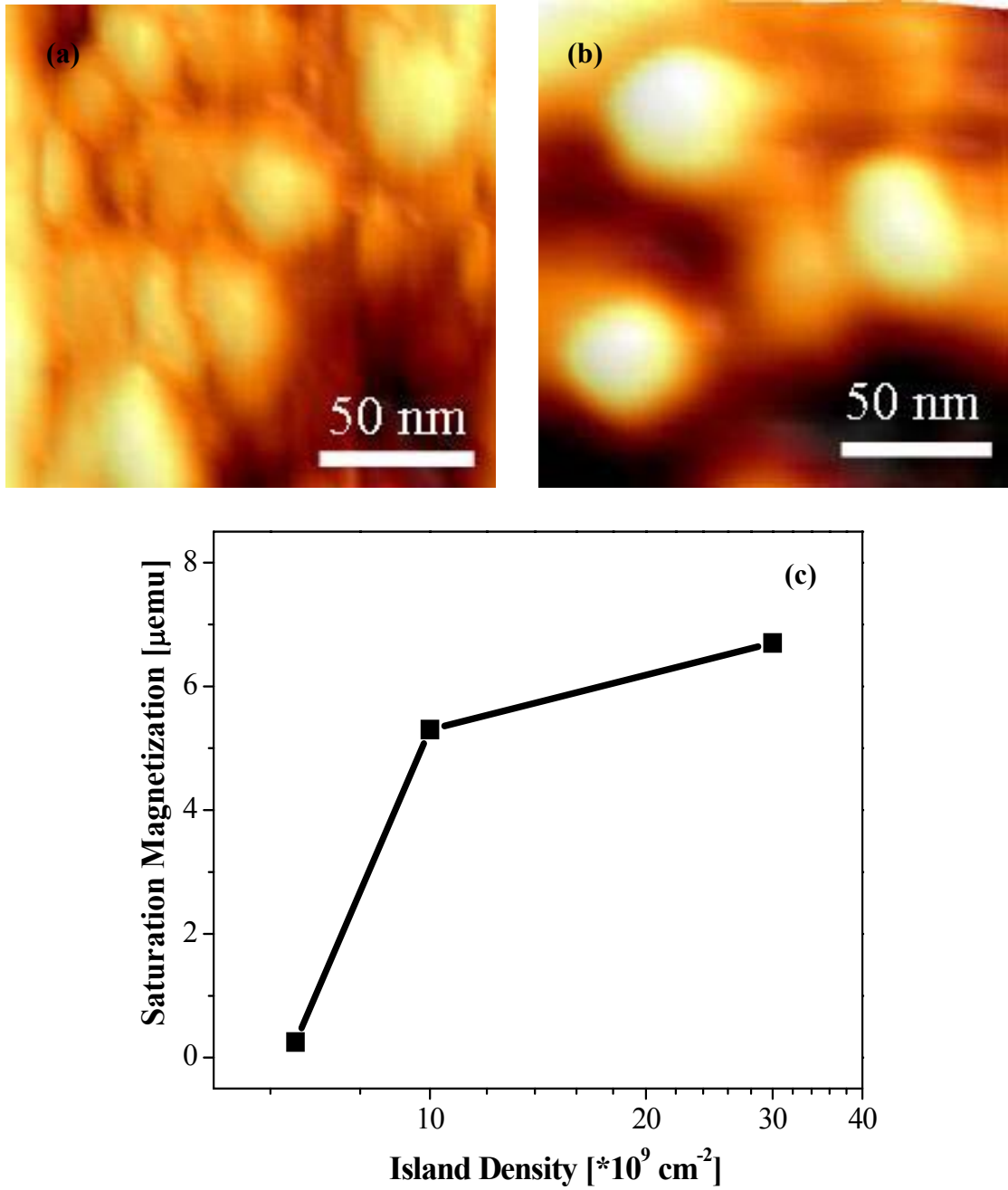Figure 7.11 AFM images (a) and (b) with different dot densities and (c) a graph of magnetization as a function of dot densities.

Figure 7.11 shows an effect of nanostructure density on magnetization. AFM image [see Figure 7.11 (a)] has about 3E10 cm^{-2} of dot density and Figure 7.11 (b) has about 0.8E10 cm^{-2} of dot density. Magnetization is stronger as island density increase. The magnetization depends on spin concentration which is influenced by nanostructure density. Therefore magnetization is directly affected by dot density.
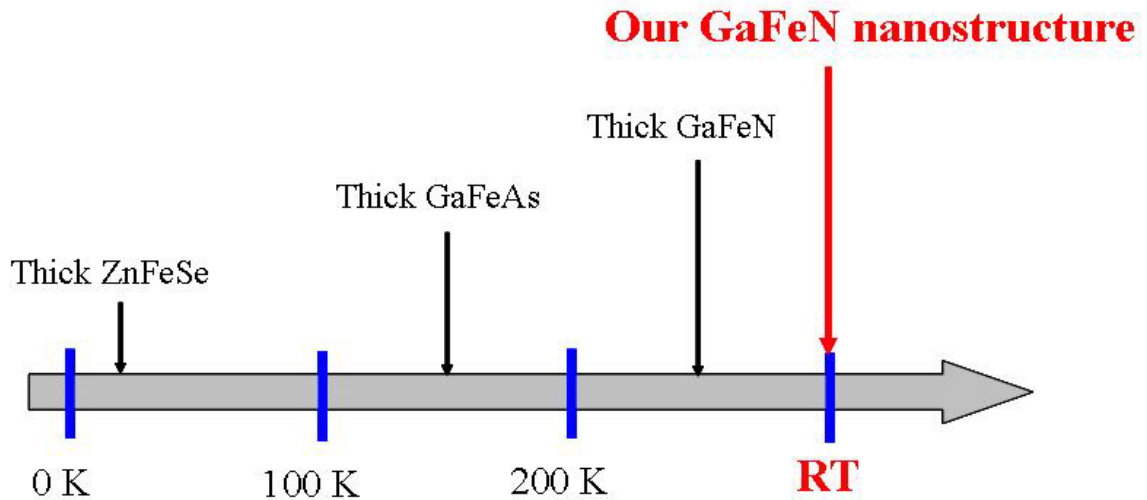
Figure 7.12 Temperatures where ferromagnetism was observed for different systems.

This section shows achievement of RT ferromagnetism in GaFeN nanostructure. Figure 7.12 shows temperatures where ferromagnetism was observed for different systems using Iron as a spintronic material. 2D ZnFeSe was observed at 20K, GaFeAs was at 160K, and even thick GaFeN film was at 250K, but RT ferromagnetism was observed in GaFeN nanostructure grown under this growth condition. Therefore, it can be an evidence that nanostructure can improve Curie temperature.

Curie temperature depends on density of states and spin concentration. The state density is larger as system dimension is reduced. Therefore, nanostructure can improve Curie temperature.

7.4. Mechanism of ferromagnetism in nanostructures

Magnetization of GaN:Fe nanostructures has been revealed by VSM measurement at room temperature. As seen in Figure 7.10, the magnetization measurements show that Fe doped GaN nanostructures contribute ferromagnetism of this system. However, there are few studies to show GaN:Fe has the Curie temperature above room temperature [25, 26], but our GaFeN nanostructures evince the ferromagnetism in the room temperature. The ferromagnetism in DMSs is caused by holes from shallow acceptors in the confined spins of the magnetic semiconductor, which occupy the cation lattice sites and act as acceptors [27,28]. However, the ferromagnetism of GaN;Fe nanostructures can be explained using the carriers-mediated mechanism, or more specifically, by the Ruderman-Kittel-Kasuya-Yosida type which describes exchange between local spin-poloarized carries and the conduction carriers. GaN has conduction carriers of nitrogen vacancy and interstitial gallium which can be native defects. But GaN:Fe nanostructure system is usually grown under metal-rich growth condition, which can easily generated the metallic interstitials and enhance higher Curie temperature by applying to shallow level donor [29].

Transition metals (TMs) are utilized for impurities in compound semiconductor materials, so they generate deep donor and/or acceptor states in these semiconductor materials, which degrades electrical and optical properties of these semiconductor materials. However Mn acting as an acceptor forms a deep-level states in 1.7eV above the valance band in GaN, otherwise Fe has 2.5eV above the valance band. Therefore they can be attractive materials for deep-level dopants with p-type co-doping.

7.5. References

[1] Ohno H *Science* **281 (**1998) 951

[2] Sato. K *Semicon. Sci. & Tech.* **17** (2002) 367

[3] Matsukura F, Ohno H, Shen A and Sugawara Y 1998 *Phys. Rev.* B **57** R2037–R2040

[4] J. Furdyna, J. Appl. Phys. **64** R29 (1988)

[5] K. Onodera, T. Matsumoto, M. Kimura, Eletron. Lett. **30** 1954 (1994)

[6] M. Reed, M. Ritums, H. Stadelmaier, M. Reed, C. Parker, S. Bedair, N. El-Masry, Mat. Lett. 51 (2001) 500

[7] S. Pearton J. Phys.:Condens. Matter **16** (2004) 209

[8] Ohno Y, Young D K, Beschoten B, Matsukura F, Ohno H and Awschalom D D 1999 *Nature* **402** 790

[9] Jonker B T, Park Y D, Bennet B R, Cheong H D, Kioseoglou G and Petrou A 2000 *Phys. Rev.* B **62** 8180

[10] Park Y D, Jonker B T, Bennet B R, Itzkos G, Furis M, Kioseoglou G and Petrou A 2000 *Appl. Phys. Lett.* **77** 3989

[11] Jonker B T, Hanbicki A T, Park Y D, Itskos G, Furis M, Kioseoglou G and Petrou A 2001 *Appl. Phys. Lett.* **79** 3098

[12] Pearton S J *et al* 2002 *J. Appl. Phys.* **92** 2047

[13] Graf T, Goennenwein S T B and Brandt M S 2003 *Phys. Status Solidi* b **239** 277

[14] Ohno. H, J. Magnetism and megnetic materials **242-245** (2202) 105

[15] M. Paillard, X. Marie, P. Renucci, T. Amand, A. Jbeli, and J. M. Gerard, *Phys. Rev. Lett.* 86, 1634 (2001).

[16] D. Gammon, E. S. Snow, B. V. Shanabrook, D. S. Katzer, and D. Park, *Science* 273, 87(1996).

[17] A. V. Khaetskii and Yu. V. Nazarov, *Physica E* **6**, 470 (2000).

[18] S. Gupta, H. Kang, M. Strassburg, A. Asghar, M. Kane, W.E. Fenwick, N. Dietz, and I.T. Ferguson, J.   Crys. Growth, **287** (2006) 596

[19] I. Daruka, and A. Barabasi, Phys. Rev. Let. **79** No. 19, 3708, (1997).

[20] E. Iliopoulos, K. Ludwig, T. Moustakas, Ph. Komninou, T. Karakostas, G. Nouet, and S. Chu, Mat. Sci. & Eng. **B87** 227 (2001).

[21] A. Rosa APL 80 2008 (2002)

[22] M. Copel, M. Reuter, E. Kaxiras, and R. M. Tromp, Phys. Rev. Let. **63** No. 6, (1989) 632

[23] A. Wolos, Phys. Rev. B 69 (2004) 115210.

[24] H. Przybylinska, Mat. Sci. & Eng. B 126 (2006) 222

[25] D. Chiba, K. Takamura, F. Matsukura, H. Ohno, Appl. Phys. Lett. **82** 3020 (2003)

[26] T. Slupinski, A. Oiwa, S. Yanagi, H. Munekata, J. Crys. Growth **237-239** 1326 (2002)

[27] http://www.free-definition.com/Spin-glass.html

[28] Frazier R M, Thaler G, Abernathy C R and Pearton S J 2003 *Appl. Phys. Lett.* **83** 1758

[29] Sharma P, Gupta A, Rao K V, Owens F J, Sharma R, Ahuja R, Osorio Guillen J M, Johansson B and Gehring G A 2003 *Nature* **2** 673

CHAPTER 8

CONCLUSION AND FUTURE WORKS

8.1 Conclusion

In this thesis, the self-assembled formation of GaN nanostructure of various templates had been successfully performed for optoelectronic and spintronic device applications.

GaN-based compound materials have high dislocation density resulting from growth on foreign substrates likes sapphire, SiC, and Si. This dislocation density in these materials determined by XRD measurements was over 10^{10} cm^{-2} that is a barrier for development of high efficiency devices. Williamson-Hall plot and reciprocal space mapping methods are employed for simple determination of the threading dislocations density. Through these methods, AlGaN also has the same order dislocation density as high as GaN has. But a small amount of indium incorporation into AlGaN layer reduces the dislocation density in AlGaN layer. This result was confirmed by etch-pit density method by AFM measurement. So we proposed a new dislocation-free structure and developed growth techniques to achieve self-assembled GaN nanostructures using MOCVD.

In this study, self-organized nanostructures have been accomplished with both lattice matched and mismatched systems. Lattice mismatched system, GaN nanostructure/ AlN, was utilized with S-K mode mechanism, whereas, Vapor -Liquid-Solid method was employed in the lattice matched system, GaN nanostructure / AlGaN.

172

In the growth in the GaN nanostructure / AlN system, the smooth AlN layer was first performed. In order to be smoother, various growth optimizations were performed. To reduce parasitic reaction, we controlled growth temperature and pressure, so then we have a smooth surface with less than 10 nm surface roughness. These nanostructures were formed under 800 C. the growth temperature is very important because it determine crystalline quality. Higher growth temperature enhances the crystalline quality, but the transition of the growth mechanism is too fast to be controlled. The temperature, 800 C was optimized.

Numerical calculation reveals the confinement and piezoelectric phenomenon in nanostructure with different nanostructure size. The quantum confinement exponentially increases as its height decrease, so the nanostructure with lower than 2nm has 1 eV higher than a bulk structure. Hence, the piezoelectric field is influenced by the strain between Al(Ga)N and GaN nanostructure, and this field was mostly strong of the order of MV/cm. However, we have a good agreement with the experimental data.

The magnetic and structural properties GaN:Mn (or Fe) self-assembled nanostructures have been studied. Incorporation of transition metal (Mn or Fe) into nanostructure enhances nucleation of islands, resulting in improving their size and density. It can be explained by the change of surface free energy. The magnetization measurements revealed magnetic properties of GaN:Fe nanostructure at room temperature (Curie temperature (T_c) > 293 K). Smaller islands have higher chance to exchange between spin-career and non-spin career due to strong confinement, which turns out to be stronger magnetization, hence higher density improved too.

8.2 Future work

It has remained the development of devices for next step. For this, there are some barriers to be overcome. First of all, n (and p)-type doping of Al(Ga)N needs to be succeeded to make p-n junction. Al(Ga)N is known as an insulator where it is very difficult to achieve doping. Till now, some of researches reported to achieve the doping in AlGaN with less 20% Al content. Thus there is a need to develop more. It has also known for AlGaN which is a difficult material to fabricate electrical contact on it. It also needs to be solved.

VITA

Hun Kang was born in Seoul, Korea, on June 18, 1974. He received his BS in Electrical Engineering from Inha University, Korea in 1998. He received his MS in 2003 and received his Ph. D. degree in 2006 under Dr. Ferguson's advice in Electrical and Computer Engineering from Georgia Institute of Technology, USA. His thesis work was entitled "A Study of the Nucleation and Formation of Multi-functional Nanostructures using GaN-Based Materials for Device Applications". In addition, he is interested in the development of thin film growth for optoelectronic applications.